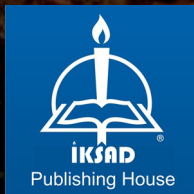


NATURAL SCIENCES: METHODS AND APPLICATIONS

EDITED BY
Dr. Seda CETINDERE

AUTHORS
Prof. Dr. Rahmiye AYDIN
Assoc. Prof. Dr. Hilal ACAY
Assoc. Prof. Dr. Hüseyin OVALIOĞLU
Assist. Prof. Dr. Ayfer YILDIRIM
Assist. Prof. Dr. Duygu İNCİ
Dr. Ayşe UĞUR
Dr. Seda CETINDERE
Dr. Semiha YILDIRIM SARIKAYA



NATURAL SCIENCES: METHODS AND APPLICATIONS

EDITED BY

Dr. Seda CETINDERE

AUTHORS

Prof. Dr. Rahmiye AYDIN

Assoc. Prof. Dr. Hilal ACAY

Assoc. Prof. Dr. Hüseyin OVALIOĞLU

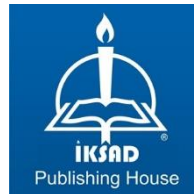
Assist. Prof. Dr. Ayfer YILDIRIM

Assist. Prof. Dr. Duygu İNCİ

Dr. Ayşe UĞUR

Dr. Seda CETINDERE

Dr. Semiha YILDIRIM SARIKAYA



Copyright © 2021 by iksad publishing house
All rights reserved. No part of this publication may be reproduced,
distributed or transmitted in any form or by
any means, including photocopying, recording or other electronic or
mechanical methods, without the prior written permission of the publisher,
except in the case of
brief quotations embodied in critical reviews and certain other
noncommercial uses permitted by copyright law. Institution of Economic
Development and Social
Researches Publications®
(The Licence Number of Publicator: 2014/31220)
TURKEY TR: +90 342 606 06 75
USA: +1 631 685 0 853
E mail: iksadyayinevi@gmail.com
www.iksadyayinevi.com

It is responsibility of the author to abide by the publishing ethics rules.
Iksad Publications – 2021©

ISBN: 978-605-74646-1-3
Cover Design: İbrahim KAYA
February / 2021
Ankara / Turkey
Size = 16x24 cm

CONTENTS

EDITED BY

PREFACE

Dr. Seda CETINDERE.....1

CHAPTER 1

MUSHROOM / MUSHROOM-BASED BIOSORBENTS FOR WASTEWATER POLLUTANTS

Assist. Prof. Dr. Ayfer YILDIRIM

Assoc. Prof. Dr. Hilal ACAY.....3

CHAPTER 2

CHEMISTRY, PRODUCTION AND APPLICATION RELATIONSHIP OF GALIUM-68 USED IN NUCLEAR MEDICAL IMAGING

Dr. Ayşe UĞUR.....39

CHAPTER 3

BODIPY-BASED FLUORESCENT CHEMOSENSORS

Dr. Seda CETINDERE

Dr. Semiha YILDIRIM SARIKAYA.....57

CHAPTER 4

A REVIEW OF DNA BINDING ACTIVITIES OF METAL(II) COMPLEXES CONTAINING AROMATIC AMINO ACIDS AND INTERCALATING LIGANDS

Assist. Prof. Dr. Duygu İNCİ

Prof. Dr. Rahmiye AYDIN.....89

CHAPTER 5

THE EFFECT OF SAMPLE AGE OF META-DIFLUOROBENZENE IN MC-800 ASPHALTENE SUSPENSION ON DYNAMIC NUCLEAR POLARIZATION PARAMETERS

Assoc. Prof. Dr. Hüseyin OVALIOĞLU115

CHAPTER 6

THE EFFECT OF SAMPLE AGE OF N-METHYL-BIS-TRIFLUOROACETAMIDE IN GALVINOXYL RADICAL ON DYNAMIC NUCLEAR POLARIZATION PARAMETERS

Assoc. Prof. Dr. Hüseyin OVALIOĞLU133

PREFACE

It is an honor for us to present the book named **Natural Sciences: Methods and Applications**. We are happy to contribute to the topics mentioned in this book scientifically at international level.

This book was published for the first time and prepared in chapters. The book consists of six chapters that describe new and current issues, after a brief introduction at first. It is a professional book in the field of Natural Sciences with important applications and methods. It includes very effective views and the latest determinations of scientists in the fields of Natural Sciences especially in chemistry, biology and physics.

This book has been prepared with the idea of partly refill the gaps in the aforementioned fields in our country and in the world and to make use of undergraduate / graduate students and our colleagues working in the fields of natural sciences.

We would like to thank İksad Publishing's managers and employees for their rigorous and patient work in conducting the typesetting, editing and printing of the book named **Natural Sciences: Methods and Applications**. Yours respectfully...

Editor of **Natural Sciences: Methods and Applications**

Dr. Seda CETINDERE

CHAPTER 1

MUSHROOM / MUSHROOM-BASED BIOSORBENTS for WASTEWATER POLLUTANTS

Dr.Öğr.Üyesi Ayfer YILDIRIM¹, Doç.Dr. Hilal ACAY²

¹ Mardin Artuklu University, Vocational School of Health Services, Mardin/Turkey
ayferyildirim@artuklu.edu.tr ORCID ID: <https://orcid.org/0000-0002-2079-4587>

² Department of Nutrition and Dietetics, Faculty of Health Science, Mardin/Turkey
hilalacay@gmail.com, ORCID ID: <https://orcid.org/0000-0002-7732-106X>

INTRODUCTION

Every year, a large number of hazardous pollutants such as dyes, metals, and organic compounds (phenolics, pharmaceuticals, pesticides, herbicides, etc.) are produced by various industries. These pollutants are a serious concern for human and animal life and therefore need to be cleaned first to avoid damage to the environment (Khatri, Peerzada, Mohsin & White, 2015). Also, they are usually in traced quantities and are not easily degraded in nature, greatly threatening environmental stability and human health. For instance, toxic metals such as Hg, Cr, Pb, Zn Cu, Cd, Co, and Ni occasioned critical problems for the environment and created serious risks for the health of humans even at low concentrations (Lemaire, Franzluebbbers, de Faccio Carvalho & Dedieu, 2014). Besides, Hg and Co are two typical metal ions in environmental samples also detected in specimens of food and plants. For example, Co metal has been reported as exposing effects on toxicological effects like cardiomyopathy and vasodilation. Hg is also a heavy metal known to be the most neurotoxic to harm most human systems (Özdemir, Okumuş & Dündar, 2013). It uses different dyes in various processing steps in many industries such as textiles, chemical refineries, leather, plastic, and paper (Ismail, Hussain, & Akram, 2013). Industrial sectors are held responsible for the passage of contaminants with toxic, carcinogenic, and mutagenic effects to humans and microorganisms, as they mix approximately 10-15 percent of these dyes that cause organic and inorganic pollution into wastewater (Balakrishnan et al.,

2016; Chequer et al., 2015). It is also stated that it can cause serious damage to systems and organs such as the reproductive system, liver, kidney, brain, central nervous system (Yagub, Sen, Afroze & Ang, 2014). As for antibiotics, even at very low levels can cause toxic effects, chronic allergic reactions, and latent growth of antibiotic-resistant bacteria in the long term (Bao, Qiang, Chang, Ben & Qu, 2014; Kuppusamy et al., 2018). And the high toxicity of pesticides can damage the respiratory, cardiovascular, and nervous system, just like organ failure and fatal consequences (Wang, Wang, Lu, Teng & Du, 2017). Therefore, successfully extracting antibiotics, pesticides, and toxic metals from agricultural water is still a very important and challenging project to maintain ecological stability and human safety. For this reason, advanced methods become an inevitable approach. In recent years, some methods such as adsorption, membrane processes, oxidation, membrane bioreactors, and their hybrid processes have been the subject of researchers' studies (Bui, Vo, Ngo, Guo & Nguyen, 2016). Among these methods, the adsorption technique, which is a simple and effective tool, is the most attractive alternative method for agricultural wastewater treatment due to its wide adaptability, environmental friendliness, and low cost (Ghasemi, Heydari & Sillanpää, et al., 2017). Many researchers have used fungi (Yildirim et al., 2020), used fungal substrate (Zhou, Zhang, Li, Su & Zhang, 2016), inanimate biomass (Schneider & Rubio, 1999), and biosorbent (Gupta, Nayak & Agarwal, 2015; Nahar, Chowdhury, Chowdhury, Rahman & Mohiuddin, 2018) as effective adsorbents to separate antibiotics, pesticides and toxic metals from agricultural

wastewater. Recently, due to its feature of being a renewable resource and biopolymer, the mushroom can be used in many fields from medicine to food, agriculture to cosmetics, from pharmacy to wastewater treatment, and the textile sector. Mushrooms that have many excellent advantages like high porosity, large specific surface area, easy modification, good flexibility, and easy separation for regeneration, can be considered as superior biosorbents for many pollutants from wastewater.

This chapter covers the current state of mushrooms / mushroom-based biosorbents (M/MBB) used in studies to efficiently remove pollutants such as heavy metals, dyes, and organic compounds (phenolic compounds, pesticides, pharmaceuticals, etc.) found in nature. Studies for the removal of pollutants in contaminated water made with M/MBB were examined with kinetic, isotherm models using the literature of the last 10 years. Summaries of the studies conducted for each pollutant are also presented in the form of tables. Future perspectives and biosorption capacities of M/MBB and methods used in biosorption are discussed. This chapter also draws attention to the prospective research requirements regarding the biosorption of wastewater pollutants by M/MBB and determines deficiencies, and also generates ideas about future studies that may be required for the literature.

1. M/MBB BIOSORBENT

Biosorption is defined as an environmentally friendly and cost-effective technique for the treatment of low concentration and high volume wastewater containing pollutants such as heavy metals, dyes, and organic compound wastes, using biomaterials such as agricultural waste, crab shells, fungi, bacteria, or composites (Nadaroğlu, Çelebi Kalkan & Tozsin, 2013). In the case of biosorption studies, researchers are mainly concerned with biosorption materials, conditions, and the mechanism of biosorption. Particularly mushrooms are considered to be the best alternatives for water purification among the biological biosorbents. Due to the adaption and growing of mushrooms under extreme conditions (pH, temperature, nutrient availability), they can be considered a versatile group. Also, the cell wall of mushrooms includes a relatively complex structure consisting of polysaccharides, lipids and, proteins providing a large number of active binding sites for pollutants with functional groups as amides, hydroxyl, and carbonyl (Yang et al., 2020).

Significant advances have been made in many pollution removals using the mushrooms themselves. However, to overcome the shortcomings of a single substance (particle size, mechanical properties, change properties and chemical stability, etc.) and to further improve adsorption performance and stability, modified mushrooms and mushroom-based composite materials by physical or chemical methods were also prepared and investigated in adsorption studies. Recently, various mushrooms and mushroom-derived

biosorbents have been investigated for biosorption of pollutants, such as *Pleurotus ostreatus* (Yang et al., 2020; Chen, Deng, Chen, Yang & Xu, 2014), *Armillaria tabescens* (Yildirim & Acay, 2020), *Morchella conica* (Yildirim & Acay, 2020), *Agaricus bisporus* (Toptas, Demierege, Ayan & Yanik, 2014; Long, Li, Ni, Xua & Xu, 2015), *Shiitake* (Yang et al., 2020; Wu et al., 2019), *Aspergillus niger* (Chatterjee, Mahanty, Das, Chaudhuri & Das, 2020), *Trametes versicolor* (Subbaiah, Yuvaraja, Vijaya & Krishnaiah, 2011), pretreated Fungus Biomass (Ahmed & Ebrahim, 2020), inactive biomass of the fungus (Grassi et al., 2019), plant gum-mushroom biocomposite (Das, Vimala & Das, 2015), renewable biopolymer composite (Kumari & Sobha, 2016), Fe₃O₄ nanoparticle-coated mushroom (Wang et al., 2019a), etc. These biosorbents have been used in the removal of many pollutants from wastewater such as dyes (Malachite green, Safranin T, Congo red, Basic Red 18, Direct red 5B, etc.), heavy metals (Cu(II), Pb(II), Cr(IV), Fe(III), Mn(II), Hg(II), Ur(VI), etc), organic compounds (phenolic compounds, pesticides, pharmaceuticals, etc.) (**Figure 1**). On the other hand, spent mushroom waste is residual compost waste produced by the mushroom production industry, and considering that 1 kg of mushrooms creates 5 kg of waste, it turns out to cause serious pollution in the environment. Besides, thanks to the richness of the spent mushroom waste in terms of natural polymers and thus their functional groups, they will be able to provide high binding sites for pollutants in wastewater treatment process.

2. KINETICS of BIOSORPTION

Kinetic of biosorption studies is an important parameter for wastewater treatments because it provides significant parameters to determine the mechanism of the biosorption process. Generally, pseudo-first-order and pseudo-second-order models were preferred to determine the kinetic parameters of the biosorbents. The pseudo-first-order kinetic model is given by the following equation (Mishra et al., 2020) (1):

$$\ln (q_e - q_t) = \ln q_e - k_1 t \quad (1)$$

where q_e and q_t are the amounts of adsorbed adsorbate (mg/g) at equilibrium and t time (min), respectively. Also, k_1 is the rate constant of biosorption (1/min) and can be calculated from the plot of $\ln (q_e - q_t)$ vs t . The pseudo-first-order kinetic model implies that the adsorption processes of pollutants by biosorbents is controlled by physical processes.

The pseudo-second-order kinetic model which indicating the chemical-adsorption-mechanism can be expressed as (Osman, Hendi & Saleh, 2020)(2):

$$1/q_t = 1/k_2 q_e^2 + t/q_e \quad (2)$$

Where k_2 is the pseudo-second-order kinetic model (min g/mg). From the plot of the t/q_t vs t , k_2 and q_e values can be calculated from slope and intersection, respectively. The pseudo-second-order kinetic model supposes that chemical-adsorption is the rate-limiting step, and the removal of pollutants is directly proportional to the active groups on the biosorbent surface. Pseudo-first-order kinetic model is applicable only during the initial stage of the biosorption process whereas pseudo-second-order kinetic model applies over a long period time.

3. ISOTHERMS of BIOSORPTION

Isotherms of biosorption which are of great importance in optimizing the use of adsorbents, are widely used models to explain how the interaction between biosorbents and adsorbate occurs. The adsorption isotherm is used to draw graphs between the amount of adsorbed material and the concentration at equilibrium and with a constant temperature. Although various adsorption isotherms are examined by researchers, Langmuir and Freundlich adsorption isotherms are the most commonly investigated isotherm models. Langmuir isotherm model which suggests homogeneous active sites existed on the surface of the biosorbent and monolayer is given by equation (3) (Wei, Xu, Mei & Tan, 2020):

$$1/q_e = 1/q_{max} + 1/K_L C_e q_{max} \quad (3)$$

Where q_e and C_e expressed the adsorption capacity (mg/g) and concentration of adsorbate (L/mg) at equilibrium, respectively. K_L is

the Langmuir constant (L/mg), and q_{max} expressed the maximum adsorption capacity. K_L and q_e values can be calculated from the plot of $1/C_e$ vs $1/q_e$.

Freundlich isotherm model describes the multilayer adsorption and heterogeneous active sites on the surface of the biosorbents are followed as (Nnadozie & Ajibade, 2020)

$$\ln q_e = \ln K_F + 1/n (\ln C_e) \tag{4}$$

Where K_F and n express the Freundlich constant (mg/g) and biosorption favorability, respectively. When the $\ln q_e$ vs $\ln C_e$ is plotted, K_F and n can be calculated from intersection and slope, respectively.

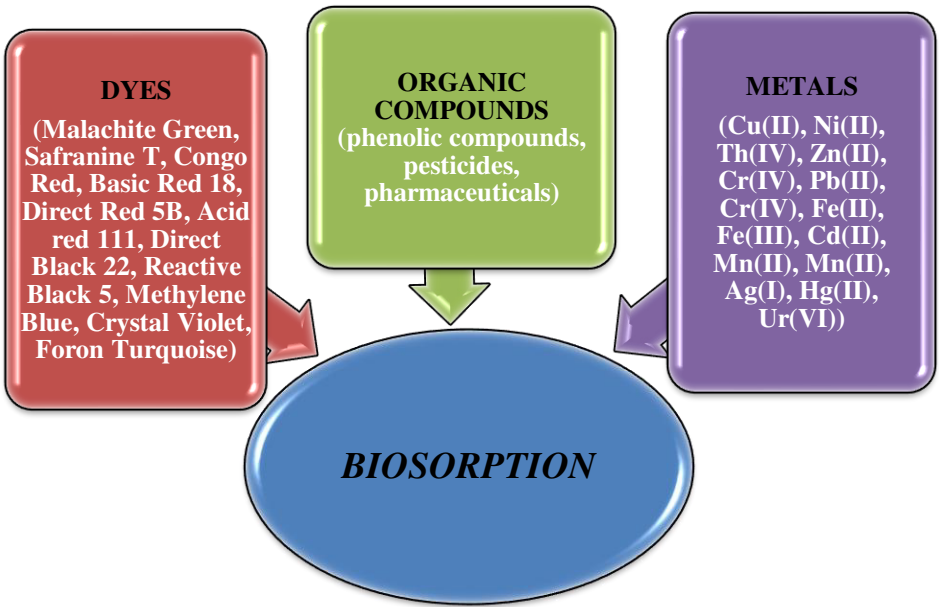


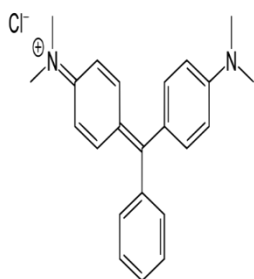
Figure 1: Type of Adsorbates by M/MBB in The Biosorption Process

4. ADSORBATES

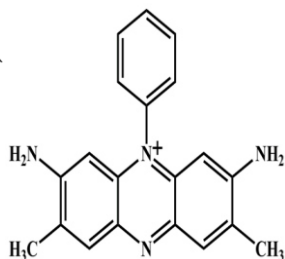
4.1. Biosorption of Dyes

Dyes are complex organic compounds with different structures and great differences in their chemical structure and toxicity. In worldwide, there are more than 10.000 dyes and pigments synthesized in industries and 10-15% of them are mixed into wastewater when applied. Dyes have three types according to their ionic structure: nonionic, anionic, and cationic (Ahmadipouya et al., 2021). Synthetic dyes used in the dye industry are stable structures especially due to their aromatic structure and are not biodegradable. Wastewater originating from textile industries is exposed to dangerous environmental problems due to the presence of dyes and similar pollutants. Therefore, the dyes from these industries must be removed from the wastewater before being discharged into rivers. In the literature, for this purpose, many types of mushrooms, mushroom waste, mushrooms-based composite materials, mushroom biomass, spent mushroom compost, spent mushroom substrate, etc. were used as biosorbents for dye removal (**Table 1**) Fungi were preferred in dye biosorption due to their containing different groups such as amino, carboxyl and thiol, which are responsible for binding dye molecules in the cell wall. **Figure 2** shows the chemical structure of different type of dyes that were investigated for biosorption by M/MBB. As it can be stated from the data in **Table 1**, the biosorption capacity of edible fungus substrate porous carbon material biosorbent for Rhodamine dye removal was obtained as 1497 mg/g and was determined as the

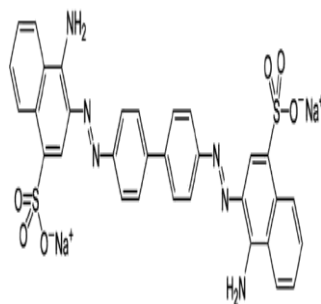
highest data among mushroom-based materials (Chen et al., 2021). Here, the pore structure formed on the material surface plays an important role in the adsorption process. The huge specific surface area ($2767.3 \text{ m}^2/\text{g}$) and highly total pore volume ($1.3936 \text{ cm}^3/\text{g}$) of edible fungus substrate porous carbon material could provide many pore filling sites and provides great adsorption capacity. In the evaluation of adsorption studies carried out in the last 10 years discussed in this chapter, it was observed that adsorption isotherms were compatible with the Langmuir model and the Pseudo-second-order kinetic model in most of the studies. This proved that the biosorption of dyes and M/MBB following monolayer biosorption and chemisorption.



Malachite Green



Safranin T



Congo Rred

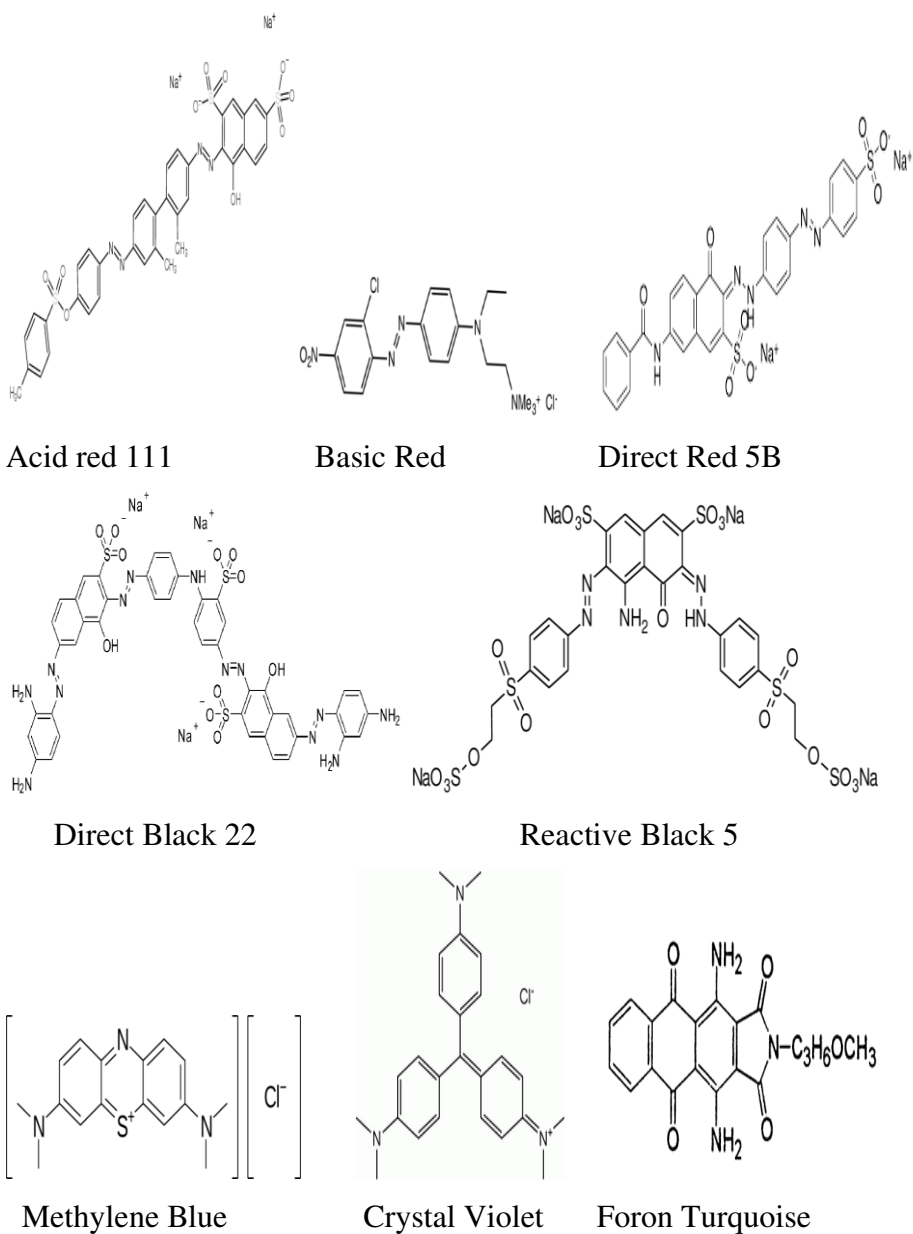


Figure 2: Chemical Structures of Different Dyes Adsorbed by M/MBB

Table 1: Type of M/MBB for Dye Biosorption

Biosorbent	Mushroom genus	Adsorbate	Kinetic Model	Isotherm Model	Biosorption Capacity	Reference
Mushroom Waste-derived g-C ₃ N ₄ (polymeric graphitic carbon nitride)	<i>Pleurotus ostreatus</i>	Methylene blue	Pseudo-second	Langmuir & Freundlich	-	(Yang, Chao, Chou, Wang & Hu, C 2020).
Spent substrate	<i>Ganodorma lucidum</i>	Malachite green, Safranin T Methylene blue	Pseudo-second	Langmuir & Freundlich	94 % 85 % 97 %	(Wu et al., 2018)
Edible fungus substrate porous carbon material	-	Rhodamine dye	Pseudo-second	Langmuir	1497 mg/g	(Chen, et al., 2021)
Agricultural waste edible fungus slag derived nitrogen-doped hierarchical porous carbon	-	Methylene blue	Pseudo-second	Langmuir	869 mg/g	(Cheng et al., 2019)
Derived <i>Penicillium janthinellum</i> strain fungus	<i>Penicillium janthinellum</i>	Congo red	-	Langmuir & Freundlich	102.4 mg/g	(Zhang, Lu, Bai, Lin & Yao, 2016)
<i>Pleurotus ostreatus</i> fungus	<i>Pleurotus ostreatus</i>	Malachite green	Pseudo-second	Freundlich	32.33 mg/g	(Chen, Deng, Chen, Yang & Xu, 2014)
Mushrooms	<i>Pleurotus ostreatus</i> <i>Armillaria tabescens</i> <i>Morchella conica</i>	Methylene blue Malachite green	Pseudo-second	Freundlich	82.81 mg/g 43.90 mg/g 38.47 mg/g 64.13 mg/g 56.80 mg/g 39.28 mg/g	(Yildirim, & Acay, 2020)
Mushroom-based bio-composite	<i>Pleurotus ostreatus</i>	Malachite green Methylene blue		Langmuir	77.11 mg/g 40.11 mg/g	(Yildirim, 2020)
Spent Mushroom Compost	<i>Agaricus</i>	Acid Red 111	Pseudo-second Pseudo-		140.9 mg/g 400.0 mg/g	

	<i>bisporus</i>	Basic Red 18 Levafix Braun	second Pseudo-first	Langmuir	169.5 mg/g	(Toptas, Demierege, Ayan & Yanik, 2014)
Hydrothermal treated shiitake mushroom	<i>Shiitake mushrooms</i>	Congo red	Pseudo-first	Langmuir	217.86 mg/g	(Yang et al., 2020)
Spent mushroom waste	<i>Pleurotus ostreatus</i>	Direct red 5B Direct black 22 Direct black 71 Reactive black 5	Pseudo-second	Langmuir	18.00 mg/g 15.46 mg/g 20.19 mg/g 14.62 mg/g	(Alhujaily, Yu, Zhang & Ma, 2020)
Spent mushroom substrate	-	Methylene blue	Pseudo-second	Temkin	63.5 mg/g	Yan & Wang, 2013)
Solid residues from mushroom production	<i>Pleurotus ostreatus</i>	Azure B Indigo carmine Malachite green Xylidine	-	Freundlich	-	(Leandro & Forchiassin, 2018)
Modified spent mushroom waste	<i>Pleurotus ostreatus</i>	Direct red 5B Direct blue 71 Reactive black 5	Pseudo-second	Langmuir	249.57 mg/g 338.67 mg/g 265.01 mg/g	(Alhujaily, Yu, Zhang & Ma, 2018)
Pretreated Fungus Biomass	<i>Agaricus bisporus</i>	Methylene blue Congo red	Pseudo-second	Langmuir	239.818 mg/g 76.412 mg/g	(Ahmed & Ebrahim, 2020),
Naturally Grown Fungi	<i>Daedalea africana</i> <i>Phellinus adamantinus</i>	Methylene blue	Pseudo-second	Langmuir	90 % 72 %	(Sintakindi & Ankamwa, 2020)
Inactive biomass of the fungus	<i>Diaporthe schini</i>	Crystal violet	Elovich	Sips	642.3 mg/g	(Grassi et al., 2019)
Mixed biomass of white rot fungi from synthetic effluents	<i>Ganoderma lucidum</i> <i>Coriolus versicolor</i>	Foron turquoise SBLN	Pseudo-second	Langmuir & Freundlich	37 %	(Sadaf & Bhatti, 2011)

T: Temperature, ET: Equilibrium time

4.2. Biosorption of Metals

Heavy metal pollution has been one of the most serious environmental problems today. Compared to organic pollutants, heavy metals are not biodegradable and therefore their removal is extremely important for the health of living specimens due to their high toxicity. Dumped new energy batteries and industrial wastes containing heavy metals such as mineral processing cause water pollution, which poses a great threat to the environment (Dou, Liu & Li, xxxx). The removal of these toxic heavy metals from contaminated water is becoming very important and urgent and has become the subject of research for many researchers to develop innovative ways (Liu, Yang, Gu, Liu & Yang, 2021). In the removal of heavy metals, M/MBB has gained an important place in the biosorption technique in recent years. The interaction of cationic metals with a wide variety of functional groups such as hydroxyl, carbonyl, and amide, in the structure of mushrooms, is one of the reasons why they are preferred in the biosorption process. These functional groups provide binding sites for metal ions and support the practice of removing toxic metal ions from polluted water. The studies conducted in recent years by removing heavy metals from polluted water with mushroom-based materials are summarized in **Table 2**. When **Table 2** is examined, Cu (II), Pb (II), Ni (II), Cr (IV), Ag (I), Fe (III), Hg (II), Cd (II), and many other heavy metal removal studies have been examined and generally fit the Langmuir isotherm model and Pseudo-second-order kinetic model, and very rarely fit the Freundlich isotherm model and Pseudo-first-order kinetic model. Also, according to the data obtained, the column technique was used

in several studies while the batch technique was preferred in many other studies. Jiang, Hao & Yang, (2016) investigated Pb(II) biosorption by *Lentinus edodes*, *Flammulina velutipes*, *Pleurotus eryngii*, *Hypsizygus marmoreus*, *Agrocybe cylindracea* mushrooms in their study and determined that *Flammulina velutipes* and *Pleurotus eryngii* have higher biosorption capacity than others. Besides, as can be seen from **Table 2**, biosorption of Cu(II), Ni(II), Pb(II), Zn (II) and Cr (IV) metals have been studied extensively, while Hg (II) and Ur (VI) metal biosorption seems to be less studied with M/MBB.

Table 2: Type of M/MBB for Metal Biosorption

Biosorbent	Mushroom genus	Adsorbate	Kinetic Model	Isotherm Model	Biosorption Capacity (mg/g)/(%)	Reference
Mushroom-derived chitosan-glucan nano paper filters	<i>A. bisporus</i>	Cu(II)	-	Langmuir	162 mg/g	(Janescha et al., 2020)
Mushroom biomass	<i>Lepiota hystrix</i>	Pb(II) Cu(II)	Pseudo-second	Langmuir	3.89 mg/g 8.50 mg/g	(Kariuki, Kiptoo & Onyancha, 2017).
Biochar derived from mushroom waste (agricultural waste)	<i>Lentinula edodes</i>	Cr(IV)	Pseudo-second	Langmuir	47.1 mg/g	(Wang et al., 2019a)
Composted spent mushroom substrate (CSMS)	<i>Lentinus edodes</i>	Pb(II)	-	Langmuir & Freundlich	31.56 mg/g	(Li, Zhanga, Sheng & Qing, 2018)
Spent Mushroom <i>Tricholoma lobayense</i>	<i>Tricholoma lobayense</i>	Pb(II)	-	Langmuir	210 mg/g	(Dai, Cen, Ji, Zhang & Xu, 2012)
A cationic surfactant spent	<i>Tricholoma lobayense</i>	Cr(IV)	-	Langmuir	43.86 mg/g	(Jing et al., 2011)

mushroom						
Plant gum-mushroom biocomposite	<i>Pleurotus platypus</i>	Ag(I) Zn(II)	pseudo-second	Langmuir & BDST	137.8 mg/g 287.9 mg/g	(Das, Vimala & Das, 2015)
Immobilized fungi residues	<i>Flammulina velutipes</i> <i>Auricularia polytricha</i> <i>Pleurotus eryngii</i> <i>Pleurotus ostreatus</i>	Cu(II) Zn(II) Hg(II)	Pseudo-second	Langmuir	8.1 mg/g 7.2 mg/g 8.5 mg/g	(Li, Zhanga, Sheng & Qing, 2018)
Fungus	<i>Cystosiera compressa</i> , <i>Sargassum vulgare</i> , <i>Turbinaria</i> , <i>Agaricus campestris</i>	Cu(II) Pb(II)	Pseudo-second	Freundlich	99 % 99%	(Negm, Abd El Wahed, Hassan & Kana, 2018)
Immobilized spent substrate of fragrant mushroom	-	Cu(II)	-	-	45.56 mg/g	(Xiao-jing, Hai-dong, Ting-ting, Yu & Juan-juan, 2014)
Spent substrate	<i>Auricularia auricula</i>	Cr(IV)	Pseudo-second	Langmuir & Freundlich	9.327 mg/g	(Dong et al., 2018)
Renewable biopolymer composite	<i>Agaricus bisporous</i>	Pb(II)	Pseudo-second	Langmuir	6.96 mg/g	(Kumari, and Sobha, 2016)
Superparamagnetic iron oxide nanoparticles	<i>Aspergillus niger</i>	Cr(IV)	Pseudo-second	Langmuir	-	(Chatterjee, Mahanty, Das, Chaudhuri & Das 2020)
Citric acid-treated mangrove endophytic fungus <i>Fussarium</i> sp.	<i>Fussarium</i>	Th(IV)	Pseudo-second	Langmuir	75.47 mg/g	(Yang et al., 2013)
Endophytic fungus (EF) <i>Microspheopsis</i> sp. LSE10	<i>Microspheopsis</i> sp.	Cd(II)	Pseudo-second	Langmuir	247.5 mg/g	(Xiao et al., 2010)
Mushroom <i>Pleurotus ostreatus</i>	<i>Pleurotus ostreatus</i>	(Pb) (Cr) (Ni)	-	-	-	(Suseem & Saral, 2014)

<i>Pleurotus</i> Spent Mushroom Compost	<i>Pleurotus</i> <i>ostreatus</i>	Mn(II)	-	-	3.3 mg/g	(Kamarudza aman, Chay, Ab Jalil & Talib, 2015a)
Mushroom Biomass and Spent Mushroom Substrate	<i>Pleurotus</i> <i>ostreatus</i>	Pb(II)	Pseudo- second	Freundlich	57.73 mg/g 85.91 mg/g	(Eliescu, et al., xxxx).
Spent Mushroom Compost	<i>Pleurotus</i> <i>ostreatus</i>	Fe(III)	Pseudo- second	Langmuir	% 80	(Kamarudza aman, Chay, Ab Jalil & Talib, 2013)
Spent mushroom compost	<i>Pleurotus</i> <i>ostreatus</i>	Ni(II)	Pseudo- second	Langmuir	3.04 mg/g	(Tay et al., 2011)
Spent Mushroom Compost Biochar		Zn(II) Cu(II) Pb(II)	Pseudo- second & Intraparticle diffusion	Langmuir	7.5 mg/g 12 mg/g 55 mg/g	(Abdallah, Ahmad, Walker, Leahy & Kwapinski, 2019)
Spent Mushroom Compost	<i>Pleurotus</i> <i>ostreatus</i>	Fe(II)	Pseudo- second	Langmuir	45 %	(Kamarudza aman, Chay, Ab Jalil & Talib, 2015b)
Edible Macrofungi	<i>Lentinus</i> <i>edodes</i> <i>Flammulina</i> <i>velutipes</i> <i>Pleurotus</i> <i>eryngii</i> <i>Hypsizygus</i> <i>marmoreus</i> <i>Agrocybe</i> <i>cylindracea</i>	Pb(II)	Pseudo- second	Freundlich Langmuir	84.314 mg/g 105.481 mg/g 107.170 mg/g 72.817 mg/g 84.345 mg/g	(Jiang, Hao & Yang, 2016)
Pilot-scale packed bed systems	<i>Agaricus</i> <i>bisporus</i> + <i>Pleurotus</i> <i>cornucopiae</i>	Cu(II) Cd(II) Pb(II) Ni(II) Zn(II)	Pseudo- second	Langmuir	6.0 mg/g 18.8 mg/g 26.1 mg/g 1.5 mg/g 1.1 mg/g	(Long, Li, Ni, Xua & Xu, 2015)

Amended mushroom	<i>Aspergillus versicolor</i>	Fe(II)	-	Langmuir & Freundlich	22.2 mg/g	(Hassouna, Marzouk, Elbably & El Maghrabi, 2018)
Mushrooms and Spent Substrate	<i>Pleurotus ostreatus</i>	Cd(II)	Pseudo-second	Langmuir & Freundlich	78 %	(Georgescu et al, 2019)
Biochar derived from spent mushroom substrate	<i>Pleurotus ostreatus Shiitake</i>	Pb(II)	Pseudo-second	Langmuir	326 mg/g 398 mg/g	(Wu et al, 2019)
Fe ₃ O ₄ nanoparticle-coated mushroom	<i>Agrocybe cylindracea</i>	Cr(VI)	Pseudo-second	Langmuir	98.92 %	(Wang et al., 2018)
Microfungus	<i>Ustilago maydis</i>	Cr(IV)	Pseudo-second	Langmuir & Freundlich	131.55 mg/g	(Serrano-Go'mez & Olguin, 2015)
Fungus mycelium modified by the bis-amidoxime-based groups	<i>Fusarium sp.</i>	Ur(VI)	Pseudo-second	Langmuir & Freundlich	370.85 mg/g	(He et al., 2019)
Fungus	<i>Pleurotus ostreatus</i>	Ni(II)	Pseudo-second	Langmuir	20.71 mg/g	(Mahmood, et al., 2016)
Fungal biomass	<i>Penicillium sp.</i>	Pb(II)	-	Langmuir-Freundlich	60.26 mg/g	(Ezzouhria, et al., 2010)
Loofa-immobilized fungus mycelia	<i>Phanerochaete chrysosporium</i>	Cr(II)	Pseudo-second	Langmuir	92.59 mg/g	(Bashardoust, Vahabzadeh, Shokrollahzadeh & Monazzami, 2010).

T: Temperature, ET: Equilibrium time, RT: Room temperature

4.3. Biosorption of Organic Pollutants

The discharge of phenolic compounds producing by phenol industrial to wastewater, has caused the massive environmental pollution. Chlorinated phenolic compounds generated by petroleum and petrochemical, coal conversion, other chemical processes, etc. are common pollutants among the phenolic groups in wastewater. Phenol and its derivatives have toxic and carcinogenic effects to aquatic life and humans. Prolonged exposure to phenolic pollutants can cause severe nervous system damage and damage to the lungs and kidneys (Kumar & Kim, 2011; Yao, Zhang, Long, Dai & Ding, 2020). It is important to remove phenolic compounds from dirty water. For this purpose, in this study, removal studies of phenolic compounds with biosorbents developed using M/MBB with biosorption technique were investigated and the results are given in **Table 3**. The chemical structure of some organic compounds adsorbed with M/MBB is shown in **Figure 3**. Cheng et al. (2019) have investigated the removal of Bisphenol A and 2,4-dichlorophenol pollutants with the preparation of carbonized fungus slag biosorbent and they found quite high biosorption capacities as 1249 mg/g and 1155 mg/g, respectively.

In Western civilizations, the use of all pharmaceutical active compounds such as antibiotics, analgesics, antidepressants are increasing significantly. Active pharmaceutical compounds are regarded as emerging pollutants since the wastewater operation boundaries are not yet known and continue to pose a serious problem among these organic compounds. Active pharmaceutical compounds

are formed in small quantities and become biologically damaging over a while since they are not hydrolyzed and biodegradable. With the increasing production and use of pharmaceutically active compounds, their release to the environment has increased and some of these substances enter water resources have reached serious levels (Shin et al., 2021; Zhao et al., 2016). As a result, in recent years, scientists have remarked on the removal of these and similar substances from polluted water. Some alternative studies on the removal of active pharmaceutical compounds from contaminated water using M/MBB are given in **Table 3**. de Jesus Menk and coworkers (2019) have studied the batch biosorption of paracetamol and 17 α -ethynyl estradiol as pharmaceutical compounds by mushroom stem waste by using two different mushrooms, *Agaricus bisporus* and *Lentinula edodes*. According to the results obtained from the biosorption experiments of paracetamol and 17 α -ethynyl estradiol pharmacological compounds, *Agaricus bisporus* mushroom waste (34.2 mg/g, 338 mg/g) has a higher biosorption capacity than *Lentinula edodes* waste (18.95 mg/g, 0.31 mg/g). When the isotherm data of this study conducted with the batch method were examined, it was emphasized that the results were compatible with both the Langmuir and Freundlich isotherm models.

Pesticides are organic pollutants that are used to increase the income of the agricultural product and potentially harmful to the environment and human health, as more than 70% remain in the soil environment (Li, Wang & Zhang, 2021). These impurities also become a serious

risk in terms of water pollution by mixing with water from the soil. In the study in which the biosorption of Linuron, Diazinon, and Myclobutanil was performed with the spent mushroom substrate biosorbent, all three pesticide biosorption processes were found to be suitable for Freundlich isotherm (**Table 3**) (Rodríguez-Cruz et al., 2012). According to the data obtained in this study, studies of the removal of pesticides using M/MBB are limited. Therefore, in this field, new studies can be developed by using new biosorbents based-mushroom for biosorption of different pesticides.

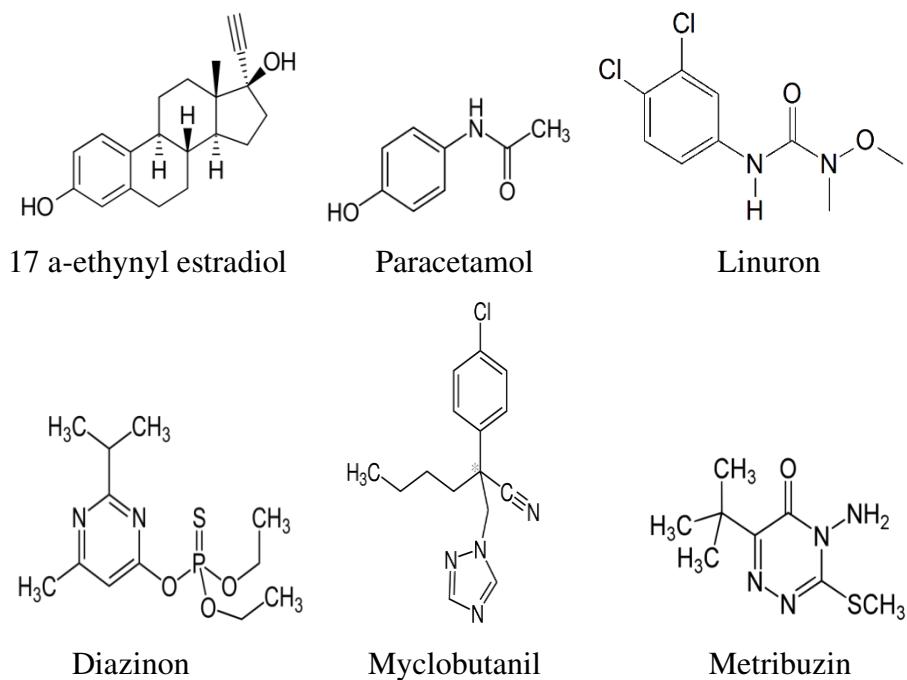


Figure 3: Chemical Structures of Different Organic Compounds Adsorbed with M/MBB.

Table 3: Type of M/MBB for Organic Compounds Biosorption

Biosorbent	Mushroom genus	Adsorbate	Kinetic Model	Isotherm Model	Biosorption Capacity (mg/g)	Reference
<i>Schizophyllum commune</i> fungus	<i>Schizophyllum commune</i>	Phenol 2-Chloro phenol 4-Chloro phenol	Pseudo-second	Langmuir	120 178 244	(Kumar & Kim, 2011)
Agricultural waste edible fungus slag derived nitrogen-doped hierarchical porous carbon	-	Bisphenol A, 2,4-dichlorophenol	Pseudo-second	Langmuir	1249 1155	(Cheng et al., 2019)
Mushroom stem waste	<i>Agaricus bisporus</i> <i>Lentinula edodes</i>	Paracetamol 17 α -ethynyl estradiol	-	Langmuir & Freundlich	34.2 338, 18.95 0.31	(Menk et al., 2019)
<i>Pleurotus mutilus</i> fungal biomass	<i>Pleurotus mutilus</i>	Metribuzin	-	-	3.0	(Behloul, Lounici, Abdi, Drouiche & Mameri, 2017)
Spent mushroom substrate	<i>Agaricus bisporus</i> <i>Pleurotus sp</i>	Linuron Diazinon Myclobutanol	-	Freundlich	-	(Rodríguez-Cruz et al., 2012)

T: Temperature, **ET:** Equilibrium time

CONCLUSION

According to the data obtained in this chapter, a batch method was used in most of the biosorption studies with M/MBB, and the column method was used in very few studies. Most of the pollutants (dyes, metals, organic compounds) biosorption studies have been well fitted

with the Langmuir isotherm model and pseudo-second-order kinetic model. The highest biosorption capacities were also observed in the studies of biosorbents obtained by the carbonization technique with a very high porosity structure. In the recent past, many studies about M/MBB for dyes, metals, and some organic compounds removal have been reported, but there is the deficiency in removing pesticides, pharmaceutical wastes, phenolic compounds, and other impurities in the wastewater. For research improvement, further studies should focus on investigating the pharmaceuticals, pesticides, and personal care products wastes which are known as emerging contaminants and becoming very dangerous with their increased use in the biosorption process.

REFERENCES

- Abdallah, M. M., Ahmad, M. N., Walker, G., Leahy, J. J., Kwapinski, W. (2019). Batch and Continuous Systems for Zn, Cu, and Pb Metal Ions Adsorption on Spent Mushroom Compost Biochar, *Ind. Eng. Chem. Res.*, Vol. 58, No.17 (2019), pp 7296–7307
- Ahmadipouya, S., Haris, M. H., Ahmadijokani, F., Jarahiyan, A., Molavi, H., Moghaddam, F. M., Rezakazemi, M., Arjmand, M. (2021). Magnetic $\text{Fe}_3\text{O}_4@\text{UiO}-66$ Nanocomposite For Rapid Adsorption Of Organic Dyes From Aqueous Solution, *Journal of Molecular Liquids*, Vol. 322, pp 114910.
- Ahmed, H. A. B., Ebrahim, S. E. (2020). Removal of Methylene Blue and Congo Red Dyes by Pretreated Fungus Biomass – Equilibrium and Kinetic Studies, *Journal of Advanced Research in Fluid Mechanics and Thermal Sciences*, Vol. 66, No.2 (2020), pp 84-100.
- Alhujaily, A., Yu, H., Zhang, X., Ma, F. (2018). Highly Efficient and Sustainable Spent Mushroom Waste Adsorbent Based on Surfactant Modification for the Removal of Toxic Dyes, *Int. J. Environ. Res. Public Health*, Vol. 15, (2018), pp 14-21.
- Alhujaily, A., Yu, H., Zhang, X., Ma, F. (2020). Adsorptive Removal of Anionic Dyes from Aqueous Solutions Using Spent Mushroom Waste, *Appl Water Sci.*, Vol. 10, No.183 (2020), pp 1-12.
- Balakrishnan, V. K., Shirin, S., Aman, A. M., de Solla, S.R., Mathieu-Denoncourt, J., Langlois, V.S. (2016). Genotoxic and Carcinogenic Products Arising From Reductive Transformations of The Azo Dye, Disperse Yellow 7. *Chemosphere*, Vol. 146, pp 206-215.
- Bao, X., Qiang, Z., Chang, J. H., Ben, W., Qu, J. (2014). Synthesis of Carbon-Coated Magnetic Nanocomposite ($\text{Fe}_3\text{O}_4@\text{C}$) and Its Application for Sulfonamide Antibiotics Removal from Water, *Journal of Environmental Sciences*, Vol. 26, pp 962-969.

- Bashardoost, R., Vahabzadeh, F., Shokrollahzadeh, S., Monazzami, A. R. (2010). Sorption Performance of Live and Heat-Inactivated Loofa-Immobilized *Phanerochaete chrysosporium* in Mercury Removal from Aqueous Solution, *Iran. J. Chem. Chem. Eng.*, Vol. 29, No. 4 (2010), pp 79-89.
- Behloul, M., Lounici, H., Abdi, N., Drouiche, N., Mameri, N. (2017). Adsorption Study Of Metribuzin Pesticide On Fungus *Pleurotus Mutilus*, *International Biodeterioration & Biodegradation*, Vol.119, (April 2017), pp 687-695.
- Bui, X.T., Vo, T. P. T., Ngo, H. H., Guo, W. S., Nguyen, T. T. (2016). Multicriteria Assessment Of Advanced Treatment Technologies For Micropollutants Removal At Large-Scale Applications, *Sci. Total Environ.*, 563, pp 1050–1067.
- Chatterjee, S., Mahanty, S., Das, P., Chaudhuri P., Das, S. (2020). Biofabrication of Iron Oxide Nanoparticles Using Manglicolous Fungus *Aspergillus Niger* BSC2 1 And Removal Of Cr(VI) From Aqueous Solution, *Chemical Engineering Journal*, Vol. 385, (1 April 2020), pp 123790.
- Chen, S., Zhang, B., Xia, Y., Chen, H., Chen, G., Tang, S. (2021). Influence Of Mixed Alkali On The Preparation of Edible Fungus Substrateporous Carbon Material and Its Application for The Removal of Dye, Colloids and Surfaces A, Vol. 609, (2021), pp 125675.
- Chen, Z., Deng, H., Chen, C., Yang Y., Xu, H. (2014). Biosorption of Malachite Green From Aqueous Solutions By *Pleurotus Ostreatus* Using Taguchi Method, *Journal of Environmental Health Science & Engineering*, Vol.12, N.o 63 (2014), pp 1-10.
- Cheng, J., Gu, J.J., Tao, W., Wang, P., Liu, L., Wang, C.-Y., Li, Y.-K., Feng, X.-H., Qiu, G.-H., Cao, F.-F. (2019). Edible Fungus Slag Derived Nitrogen-Doped Hierarchical Porous Carbon As A High-Performance Adsorbent For Rapid Removal Of Organic Pollutants From Water, *Bioresource Technology*, Vol. 294, (2019), pp 122149.
- Chequer, F. M., Lizier, T. M., de Felicio, R., Zanoni, M. V., Debonisi, H. M., Lopes, N. P., de Oliveira, D. P. (2015). The Azo Dye Disperse Red 13 And Its

- Oxidation and Reduction Products Showed Mutagenic Potential, *Toxicol. In Vitro.*, Vol. 29, No 7, pp 1906-1915.
- Dai, J., Cen, F., Ji, J., Zhang W., Xu, H. (2012). Biosorption of Lead(II) In Aqueous Solution By Spent Mushroom *Tricholoma Lobayense*, *Water Environment Research.*, Vol. 84, No. 4 (APRIL 2012), pp. 291-298.
- Das, D., Vimala R., Das, N. (2015). Removal of Ag(I) and Zn(II) Ions From Single And Binary Solution Using Sulfonated Form Of Gum Arabic-Powdered Mushroom Composite Hollow Semispheres: Equilibrium, Kinetic, Thermodynamic And Ex-Situ Studies, *Ecological Engineering*, Vol. 75, (2015), pp 116–122.
- Dong, L., Liang, J., Li, Y., Hunang, S., Wei, Y., Bai, X., Jin, Z., Zhang, M., Qu, J. (2018). Effect Of Coexisting Ions On Cr(VI) Adsorption Onto Surfactant Modified *Auricularia Auricula* Spent Substrate In Aqueous Solution, *Ecotoxicology and Environmental Safety*, Vol. 166, (2018), pp 390–400.
- Dou, W., Liu, J., Li, M. (xxxx). Competitive Adsorption of Cu^{2+} in Cu^{2+} , Co^{2+} and Ni^{2+} Mixed Multi-Metal Solution Onto Graphene Oxide (GO)-Based Hybrid Membranes, *Journal of Molecular Liquids* Vol. xx, pp xxx.
- Eliescu, A., Georgescu, A. A., Nicolescu, C. M., Bumbac, M., Cioateră, N., Mureșeanu, M., Buruleanu, L. C. (xxxx). Biosorption of Pb(II) from Aqueous Solution Using Mushroom (*Pleurotus ostreatus*) Biomass and Spent Mushroom Substrate, *Analytical Letters*, xxx(xxxx)xxx.
- Ezzouhria, E., Ruizb, E., Castrob, M., Moyab, F., Espínolab, L., Cherrata, H., Er-Raïouic, K., Lairinia, (2010). Mechanisms of Lead Uptake by Fungal Biomass Isolated From Heavy Metals Habitats, *Afinidad*, Vol. 545, (2010), pp 39-44.
- Georgescu, A. A., Eliescu, A., Nicolescu, C. M., Bumbac, M., Cioateră, N., Mureșeanu, M., Buruleanu, L. C. (2019). Performance of *Pleurotus ostreatus* Mushrooms and Spent Substrate for the Biosorption of Cd(II) From Aqueous Solution, *Analytical Letters*, Vol. 52, No. 13 (2019), pp 2007-2027.

- Ghasemi, E., Heydari, A., Sillanpää, M. (2017). Superparamagnetic Fe₃O₄@EDTA Nanoparticles as an Efficient Adsorbent for Simultaneous Removal of Ag (I), Hg (II), Mn (II), Zn (II), Pb (II) and Cd (II) From Water And Soil Environmental Samples, *Microchemical Journal*, 131, pp 51-56.
- Grassi, P., Reis, C., Drumm, F. C., Georgin, J., Tonato, D., Escudero, L. B., Kuhn, R., Jahn, S. L., Dotto, G. L. (2019). Biosorption Of Crystal Violet Dye Using Inactive Biomass Of The Fungus *Diaporthe Schini*, *Water Science & Technology*, Vol. 79, No. 4 (2019), pp 709-717.
- Gupta, V. K., Nayak, A., Agarwal, S. (2015). Bioadsorbents For Remediation Of Heavy Metals: Current Status And Their Future Prospects, *Environmental Engineering Research*, Vol. 20, pp 1-18.
- Hassouna, M. E. M., Marzouk, M. A., Elbably, M. A., El Maghrabi, A. H. (2018). Biosorption of Iron By Amended *Aspergillus versicolor* From Polluted Water Sources, *Biometrics & Biostatistics International Journal*, Vol. 7, No.6 (2018), pp 502–513.
- He, D., Tan, N., Luo, X., Yang, X., Ji, K., Han, J., Chen, C., Liu, Y. (2019). Preparation, Uranium (VI) Absorption And Reuseability Of Marine Fungus Mycelium Modified By The Bis-Amidoxime-Based Groups, *Radiochimica Acta*, Vol. 108, No. (2019), 1-13.
- Ismail, B., Hussain, S. T., Akram S. (2013). Adsorption of Methylene Blue onto Spinel Magnesium Aluminate Nanoparticles: Adsorption Isotherms, Kinetic and Thermodynamic Studies, *Chemical Engineering Journal*, Vol. 219, pp 395–402.
- Janescha, J., Jones, M., Bacher, M., Kontturi, E., Bismarck, A., Mautner, A. (2020). Mushroom-derived Chitosan-Glucan Nanopaper Filters For The Treatment Of Water, *Reactive and Functional Polymers*, Vol. 146, (2020), pp 104428.
- Jiang, Y., Hao, R., Yang, S. (2016). Equilibrium And Kinetic Studies on Biosorption of Pb(II) by Common Edible Macrofungi: A Comparative Study, *Canadian Journal of Microbiology*, Vol. 62, No. 4 (April 2016), pp 1-26.

- Jing, X., Cao, Y., Zhang, X., Wang, D., Wu, X., Xu, H. (2011). Biosorption of Cr(VI) From Simulated Wastewater Using A Cationic Surfactant Modified Spent Mushroom, *Desalination*, Vol. 269, (2011), pp 120–127.
- Kamarudzaman, A. N., Chay, T. C., Ab Jalil, M. F., Talib, S.A. (2013). Biosorption of Iron (III) from Aqueous Solution using *Pleurotus Ostreatus* Spent Mushroom Compost as Biosorbent. *Advanced Materials Research*, Vol. 781-784, (2013), pp 636-642.
- Kamarudzaman, A. N., Chay, T. C., Amir, A., Talib, S. A. (2015a). Biosorption of Mn(II) ions from Aqueous Solution by *Pleurotus* Spent Mushroom Compost in a Fixed-Bed Column, *Procedia - Social and Behavioral Sciences*, Vol. 195, (2015a), pp 2709 – 2716.
- Kamarudzaman, A. N., Chay, T. C., Amir, A., Talib, S. A. (2015b). Fe(II) Biosorption Using *Pleurotus* Spent Mushroom Compost as Biosorbent under Batch Experiment, *Applied Mechanics and Materials*, Vol. 695, (2015b), pp 314-318.
- Kariuki, Z., Kiptoo, J., Onyancha, D. (2017). Biosorption Studies Of Lead And Copper Using Rogers Mushroom Biomass '*Lepiota Hystrix*', *South African Journal of Chemical Engineering*, Vol. 23, pp 62-70.
- Khatri, A., Peerzada, M. H., Mohsin, M., White, M. (2015). A Review On Developments In Dyeing Cotton Fabrics With Reactive Dyes For Reducing Effluent Pollution, *J. Clean. Prod.*, Vol. 87, pp 50–57.
- Kumar, N. S., Min, K. (2011). Phenolic Compounds Biosorption Onto *Schizophyllum Commune* Fungus: FTIR Analysis, Kinetics And Adsorption Isotherms Modeling, *Chemical Engineering Journal*, Vol. 168, (2011), pp 562–57.
- Kumari, A. R., Sobha, K. (2016). Removal Of Lead By Adsorption With The Renewable Biopolymer Composite Of Feather (*Dromaius Novaehollandiae*) And Chitosan (*Agaricus Bisporus*), *Environmental Technology & Innovation*, Vol. 6, (Nov 2016), pp 11-26.
- Kuppusamy, S., Kakarla, D., Venkateswarlu, K., Megharaj, M., Yoon, Y.-E., Lee, Y.B. (2018). Veterinary Antibiotics (VAs) Contamination as a Global

- Agro-Ecological Issue: A Critical View, Agriculture, Ecosystems & Environment, Vol. 257, pp 47-59.
- Leandro, P., Forchiassin, F., (2011). Adsorption and Decolorization of Dyes Using Solid Residues from *Pleurotus ostreatus* Mushroom Production, Biotechnology and Bioprocess Engineering, Vol. 15, No. 6 (February 2011), pp 1102-1109.
- Lemaire, G., Franzluebbers, A., de Faccio Carvalho, P.C., Dedieu, B. (2014). Integrated Crop–Livestock Systems: Strategies to Achieve Synergy Between Agricultural Productiona Environmental Quality, Agriculture, Ecosystems & Environment, Vol. 190, pp 4-8.
- Li, H., Wang, F., Zhang, S. (2021). Adsorption Of Three Pesticides On Polyethylene Microplastics In Aqueous Solutions: Kinetics, Isotherms, Thermodynamics, And Molecular Dynamics Simulation, Chemosphere, Vol. 264(2), (2021), pp 128556.
- Li, X., Zhanga, D., Sheng, F., Qing, H. (2018). Adsorption Characteristics of Copper (II), Zinc (II) and Mercury (II) By Four Kinds Of Immobilized Fungi Residues, Ecotoxicology and Environmental Safety, Vol. 147, (2018), pp 357–366.
- Liu, X., Bai, X., Dong, L., Liang, J., Jin, Y., Wei, Y., Li, Y., Huang, S., Qu, J. (2018). Composting Enhances The Removal Of Lead Ions In Aqueous Solution By Spent Mushroom Substrate: Biosorption And Precipitation, Journal of Cleaner Production, Vol. 200, (2018), pp 1-11.
- Liu, X., Yang, S., Gu, P., Liu, S., Yang, G. (2021). Adsorption and Removal Of Metal Ions By Smectites Nanoparticles: Mechanistic Aspects, And Impacts Of Charge Location And Edge Structure, Applied Clay Science, Vol. 201, pp 105957.
- Long, Y., Li, Q., Ni, J., Xua, F., Xu, H. (2015). Treatment of Metal Wastewater in Pilot-Scale Packed Bed Systems: Efficiency of Single- vs. Mixed-Mushrooms, RSC Adv., Vol. 5, (2015), pp 29145.
- Mahmood, T., Khan, A., Naeem, A., Hamayun, M., Muska, M., Farooq, M., Hussain F. (2016) A.dsorption of Ni(II) Ions From Aqueous Solution onto A Fungus

- Pleurotus Ostreatus, Desalination and Water Treatment, Vol.57, (2016), pp 7209–7218.
- Menk, J. J., do Nascimento, A. I. S., Leite, F. G., de Oliveira, R. A., Jozala, A. F., de Oliveira Junior, J. M., Chaud, M. V., Grotto, D. (2019). Biosorption Of Pharmaceutical Products By Mushroom Stem Waste, Chemosphere, Vol. 237, (2019), pp 124515.
- Mishra, S., Sahoo, S. S., Debnath, A. K., Muthe, K. P., Das, N., Parhi, P. (2020). Cobalt Ferrite Nanoparticles Prepared By Microwave Hydrothermal Synthesis And Adsorption Efficiency For Organic Dyes: Isotherms, Thermodynamics And Kinetic Studies, Advanced Powder Technology, Vol. 31(11), pp 4552-4562.
- Nadaroğlu, H., Çelebi N., Kalkan, E., Tozsın G. (2013). Water Purification Of Textile Dye Acid Red 37 By Adsorption On Laccase Modified Silica Fume, Jökull, Vol. 5, pp 87 – 113.
- Nahar, K., Chowdhury, M., Chowdhury, M., Rahman, A., Mohiuddin, K. M. (2018). Heavy Metals In Handloom-Dyeing Effluents And Their Biosorption By Agricultural Byproducts, Environmental Science & Pollution Research, Vol. 25, pp 1-14.
- Negm, N. A., Abd El Wahed, M. G., Hassan, A. R. A., Kana, M. T. H. A. (2018). Feasibility Of Metal Adsorption Using Brown Algae And Fungi: Effect Of Biosorbents Structure On Adsorption Isotherm And Kinetics, Journal of Molecular Liquids, Vol. 264, (2018), pp 292-305.
- Nnadozie, E. C., Ajibade, P. A. (2020). Adsorption, Kinetic And Mechanistic Studies Of Pb(II) and Cr(VI) Ions Using APTES Functionalized Magnetic Biochar, Microporous And Mesoporous Materials, Vol. 309, pp 110573.
- Osman, A. M., Hendi, Saleh, T.A. (2020). Simultaneous Adsorption Of Dye And Toxic Metal Ions Using An Interfacially Polymerized Silica/Polyamide Nanocomposite: Kinetic And Thermodynamic Studies, Journal of Molecular Liquids, Vol. 314, pp 113640.
- Özdemir, S., Okumuş, V., Dündar, A. (2013). Preconcentration of Metal Ions Using Microbacteria, Microchim Acta, Vol. 180, pp 719–739.

- Rodríguez-Cruz, M. S., Herrero-Hernández, E., Ordax, J. M., Marín-Benito, J. M., Draoui, K., Sánchez-Martín, M. J. (2012). Adsorption of pesticides by sewage sludge, grape marc, spent mushroom substrate and by amended soils, *International Journal of Environmental Analytical Chemistry*, Vol. 92, No. 8 (2012), pp 933-948.
- Sadaf, S., Bhatti, H. N. (2011). Biosorption of Foron Turquoise SBLN Using Mixed Biomass of White Rot Fungi from Synthetic Effluents. *African Journal of Biotechnology* Vol. 10, No. 62 (12 October 2011), pp 13548-13554.
- Schneider, I. A. H., Rubio, J. (1999). Sorption Of Heavy Metal Ions By The Nonliving Biomass Of Freshwater Macrophytes, *Environmental Science & Technology*, Vol. 33, pp 2213-2217.
- Serrano-Go'mez, J., Olgu'n, M. T. (2015). Separation of Cr(VI) from Aqueous Solutions By Adsorption on The Microfungus *Ustilago Maydis*. *Int. J. Environ. Sci. Technol.*, Vol.
- Sewu, D. D., Boakye, P., Jung, H., Woo, S. H. (2017). Synergistic Dye Adsorption by Biochar from Co-Pyrolysis Of Spent Mushroom Substrate and *Saccharina Japonica*, *Bioresour Technol.*, Vol. 244, No.1 (2017), pp 1142-1149.
- Shin, J., Kwak, J., Lee, Y.-G., Kim, S., Choi, M., Bae, S., Lee, S.-H. Park, Y., Chon, K. (2021). Competitive Adsorption Of Pharmaceuticals In Lake Water And Wastewater Effluent By Pristine and NaOH-activated Biochars From Spent Coffee Wastes: Contribution of hydrophobic and p-p interactions. *Environmental Pollution* Vol. 270, pp 116244.
- Sintakindi, A., Ankamwar, B. (2020). Uptake of Methylene Blue from Aqueous Solution by Naturally Grown *Daedalea africana* and *Phellinus adamantinus* Fungi, *ACS Omega*, Vol. 5, No. 22 (2020), pp 12905–12914.
- Subbaiah, M. V., Yuvaraja, G., Vijaya, Krishnaiah, Y. A. (2011). Equilibrium, Kinetic and Thermodynamic Studies on Biosorption of Pb(II) And Cd(II) From Aqueous Solution By Fungus (*Trametes Versicolor*) Biomass, *Journal of the Taiwan Institute of Chemical Engineers*, Vol. 42, (2011), pp 965–971.

- Suseem S. R., Mary, S.A. (2014). Biosorption of Heavy Metals Using Mushroom *Pleurotus Eous*, *J. Chem. Pharm. Res.*, Vol. 6, No. 7, (2014), pp 2163-2168.
- Tay, C.-C., Liew, H.-H., Redzwan, G., Yong, S-Ki, Surif, S., Abdul-Talib, S. (2011). *Pleurotus Ostreatus* Spent Mushroom Compost As Green Biosorbent for Nickel (II) Biosorption, *Water Sci Technol.*, Vol. 64, No.12 (2011), pp 2425–2432.
- Toptas, A., Demierege, S., Ayan, E. M., Yanik, J. (2014). Spent Mushroom Compost as Biosorbent for Dye Biosorption, *Clean – Soil, Air, Water*, Vol. 42, (6 November 2014), pp 1–8.
- Wang, X., Wang, H., Lu, M., Teng, R., Du, X. (2017). Facile Synthesis of Phenyl-Modified Magnetic Graphene/Mesoporous Silica with Hierarchical Bridge-Pore Structure for Efficient Adsorption of Pesticides, *Materials Chemistry and Physics*, Vol. 198, pp 393-400.
- Wang, C., Liu, H., Liu, Z., Gao, Y., Wu, B., Xu, H. (2018). Fe_3O_4 Nanoparticle-Coated Mushroom Source Biomaterial For Cr (VI) Polluted Liquid Treatment And Mechanism Research, *R. Soc. open sci.*, Vol. 5, (2018), pp 171776.
- Wang, C., Tan, H., Liu, H., Wu, B., Xu, F., Xu, H. (2019a). A Nanoscale Ferroferric Oxide Coated Biochar Derived From Mushroom Waste To Rapidly Remove Cr(VI) And Mechanism Study, *Bioresource Technology Reports*, Vol. 7, pp 100253.
- Wang, Y., Yi, B., Sun, X., Yu, L., Wu, L., Liu, W., Wang, D., Li, Y., Jia, R., Yu, H., Li, X., (2019b). Removal and Tolerance Mechanism of Pb by A Filamentous Fungus: A Case Study, *Chemosphere*, Vol. 225, pp 200-208.
- Wei, J., Xu, J., Mei, Y., Tan, Q. (2020). Chloride Adsorption on Aminobenzoate Intercalated Layered Double Hydroxides: Kinetic, Thermodynamic And Equilibrium Studies, *Applied Clay Science*, Vol. 187, pp 105495.
- Wu, J., Zhang, T., Chen, C., Feng, L., Su, X., Zhou, L., Chen, Y., Xia, A., Wang, X. (2018). Spent Substrate of *Ganodorma Lucidumas* A New Bio-Adsorbent for Adsorption of Three Typical Dyes, *Bioresource Technology*, Vol. 6, (2018), pp 134-138.

- Wu, Q., Xian, Y., He, Z., Zhang, Q., Wu, J., Yang, G., Zhang, X., Qi, H., Ma, J., Xiao Y., Long, L.(2019). Adsorption Characteristics of Pb(II) Using Biochar Derived From Spent Mushroom Substrate, Scientific Reports, Vol. 9, (2019), pp 15999.
- Xiao, X., Luo, S., Zeng, G., Wei, W., Wan, Y., Chen, L., Guo, H., Cao, Z., Yang, L., Chen, J., Xi, Qia. (2010). Biosorption of Cadmium by Endophytic Fungus (EF) *Microsphaeropsis* sp. LSE10 Isolated from Cadmium Hyperaccumulator Solanum Nigrum L, Bioresource Technology, Vol. 101, (2010), pp 1668–1674.
- Xiao-jing, H., Hai-dong, G., Ting-ting, Z., Yu, J., Juan-juan, Q. (2014). Biosorption Mechanism Of Cu^{2+} By Innovative Immobilized Spent Substrate Of Fragrant Mushroom Biomass, Ecological Engineering, Vol. 73, (2014), pp 509–513.
- Yagub, M. T., Sen, T. K., Afroze, S., Ang, H. M. (2014). Dye and Its Removal From Aqueous Solution by Adsorption: A Review, Advances in colloid and interface science, Vol. 209, pp 172-184.
- Yan, T., Wang, L. (2013). Adsorptive Removal of Methylene Blue From Aqueous Solution by Spent Mushroom Substrate: Equilibrium, Kinetics, And Thermodynamics, BioRes., Vol. 8, No. 3 (2013), pp 4722-4734.
- Yang, K., Li, Y., Zheng, H., Luan, X., Li, H., Wang, Y., Du, Q., Sui, K., Li, H., Xia, Y. (2020). Adsorption of Congo Red With Hydrothermal Treated Shiitake Mushroom, Mater. Res. Express, Vol. 7, (2020), pp 015103.
- Yang, H.-C., Chao, M.-W., Chou, C.-J., Wang, K.-H., Hu, C. (2020). Mushroom Waste-Derived $\text{G-C}_3\text{N}_4$ for Methyl Blue Adsorption And Cytotoxic Test for Chinese Hamster Ovary Cells, Materials Chemistry and Physics, Vol. 244, (2020), pp 122715.
- Yang, S. K., Tan, N., Yan, X. M., Chen, F., Long, W., Lin, Y. C. (2013). Thorium(IV) Removal From Aqueous Medium By Citric Acid Treated Mangrove Endophytic Fungus *Fusarium* sp. #ZZF51, Marine Pollution Bulletin, Vol. 74, (2013), pp 213–219.

- Yao, L., Zhang, L., Long, B., Dai, Y., Ding, Y. (2020). N-Heterocyclic Hyper-Cross-Linked Polymers For Rapid And Efficient Adsorption Of Organic Pollutants From Aqueous Solution, *Journal of Molecular Liquids*, Vol. 325, pp115002.
- Yildirim, A. (xxxx). Kinetic, Equilibrium And Thermodynamic Investigations for The Bio-Sorption of Dyes onto Crosslinked *Pleurotus Ostreatus*-Based Biocomposite, *International Journal of Environmental Analytical Chemistry*, xxx(xxxx)xxx.
- Yildirim, A., Acay H. (2020). Biosorption Studies of Mushrooms for Two Typical Dyes, *JOTCSA*, Vol. 7, No.1 (2020), pp 295-306.
- Yildirim, A., Baran, M. F., Acay, H. (2020). Kinetic And Isotherm Investigation Into The Removal of Heavy Metals Using A Fungal-Extract-Based Bio-Nanosorbent, *Environmental Technology & Innovation*, Vol. 20, (2020), pp 101076.
- Zhang, Q., Lu, T., Bai, D.-M., Lin, D.-Q., Yao, S.-J. (2016). Self-Immobilization of A Magnetic Biosorbent And Magnetic Induction Heated Dye Adsorption Processes, *Chemical Engineering Journal*, Vol. 284, (15 January 2016), pp 972-978.
- Zhao, H., Liu, X., Cao, Z., Zhan, Y., Shi, X., Yang, Y., Zhou, J., Xu, J. (2016). Adsorption Behavior And Mechanism Of Chloramphenicols, Sulfonamides, And Nonantibiotic Pharmaceuticals On Multi-Walled Carbon Nanotubes, *J. Hazard Mater.* Vol 310, pp 235-245.
- Zhou, A., Zhang, Y., Li, R., Su, X., Zhang, L. (2016). Adsorptive Removal Of Sulfa Antibiotics From Water Using Spent Mushroom Substrate, *An Agricultural Waste, Desalination & Water Treatment*, Vol. 57, pp 388-397.

CHAPTER 2
CHEMISTRY, PRODUCTION AND APPLICATION
RELATIONSHIP OF GALYUM-68 USED IN NUCLEAR
MEDICAL IMAGING

Dr. Ayşe UĞUR¹

¹ Pamukkale University, Education and Research Hospital, Department of Nuclear Medicine, 20160, Denizli-Turkey. ayseugur@pau.edu.tr
<https://orcid.org/0000-0003-0913-6943>

INTRODUCTION

Radionuclides are used in imaging with PET/SPECT in Nuclear Medicine, where imaging has become a fundamental element in the diagnosis and diagnosis of diseases. Today, radionuclides used in the treatment of some diseases including cancer and diagnosis of many diseases with PET imaging are produced from reactors, generators or cyclotrons. In nuclear medicine, 95% of radiopharmaceuticals are used for diagnosis and 5% for treatment. While radiopharmaceuticals prepared with gamma ray emitting radionuclides are used for diagnosis in nuclear medicine, beta ray emitting radiopharmaceuticals are used in treatment (Chitambar, 2010). All of the radionuclides used in nuclear medicine are artificially produced (^{18}F , ^{76}Br , ^{124}I , ^{68}Ga , ^{64}Cu).

^{68}Ga (^{68}Ga) is one of the radionuclides that is widely used for diagnostic purposes in Nuclear Medicine. Electropositive gallium atom (Ga) is in period 4 in group 3A (boron group) in the periodic table. Ga was first discovered by Lecoq de Boisbaudran in 1878. Later, its place in the periodic table was determined by Dimitri Mendeleev (Chitambar, 2010). There is a large range between the boiling point (2204°C) and the melting point, which is not visible in any metal. The melting point of Ga (29.76°C) is one of the official temperature reference points of the International Temperature Scale (ITS-90) established by BIPM in 1990 (Preston–Thomas, 1990; Magnum & Furukawa, 1990)

Ga has two stable isotopes that occur naturally; ^{69}Ga (60.11% abundance), ^{71}Ga (39.89% abundance) (Meija, Coplen, Berglund, Brand, & et.al., 2016). Three Ga radionuclides are available in potential imaging pharmaceuticals for radiolabeling biomolecules. ^{66}Ga ($t = 9.49\text{ h}$, β^+ 4.153 MeV) and ^{68}Ga ($t = 67.71\text{ min}$, β^+ 1.92 MeV(%89); EC (%11)) degraded by positron emission. ^{67}Ga ($t = 3.26\text{ days}$ (78 hours), 93.3 keV (37%), 184.6 keV (20.4%), 300.2 keV (16.6%) and 888 keV (26%)) is degraded by gamma emission (Kumar, 2020). Other main isotopes of gallium are also shown in table 1.

Table 1. Main Isotopes of Gallium

Parent Isotope	Proton Number	Neutron Number	Half life (t ½; hour)	Decay Mode	Daughter Isotope
^{66}Ga	31	35	9.49	β^+	^{66}Zn
^{67}Ga	31	36	78.26	EC	^{67}Zn
^{68}Ga	31	37	1.1285	β^+	^{68}Zn
^{69}Ga	31	38	Kararlı		
^{70}Ga	31	39	0.3523	β^- (% 99,59)	^{70}Ge
				EC (% 0,41)	^{70}Zn
^{71}Ga	31	40	Kararlı		
^{72}Ga	31	41	14.095	β^-	^{72}Ge
^{73}Ga	31	42	4.86	β^-	^{73}Ge

The stable oxidation state of gallium is +3 and has an ionic radius of 47-62 pm. Due to its high charge density (2.6 pK) it is highly acidic and easily hydrolyzes to Ga(OH).

The purpose of this review is to evaluate the labeling properties of peptide macromolecules with ^{68}Ga .In particular, the following factors in labeling were discussed:

- Investigation of $^{68}\text{Ge}/^{68}\text{Ga}$ generators available on the market to determine the long-term efficient use potential for the ^{68}Ga radiopharmaceutical preparation.
- Gallium-68 chemistry, evaluating for conjugation of a peptide/nucleotide to a bifunctional chelator.

1. GALLIUM-68/GERMANIUM-68 ($^{68}\text{Ga}/^{68}\text{Ge}$) GENERATOR

Since the half-life of ^{68}Ge is 100 times longer than that of ^{68}Ga , a secular balance is defined between ^{68}Ge decay and ^{68}Ga accumulation (Equation (1)) (Velikyan, 2015).

$$\frac{t_{1/2} (^{68}\text{Ge})}{t_{1/2} (^{68}\text{Ga})} = 5762 \quad (1)$$

^{68}Ga accumulation with ^{68}Ge degradation has equal radioactivity 14 hours after elution (12th $t_{1/2}$). However, 50% of the maximum radioactivity accumulates after 68 minutes of elution, it is over 91% after 4 hours. Thus, three production (^{68}Ga production) can be made within a working day, depending on the age of the generator. The $t_{1/2}$ of ^{68}Ga in the European Pharmacopoeia monographs is 62–74 minutes (Pharmacopeia, 2011; Pharmacopeia, 2013).

The 271day $t_{1/2}$ of ^{68}Ge gives $^{68}\text{Ge}/^{68}\text{Ga}$ generators about 1 year of use (Velikyan, 2014). ^{68}Ge is produced by irradiation of the natural-gallium target (Meinkin, Kurczak, Mausner, Kolsky, & Srivastava, 2005) as a product of spallation after proton irradiation of molybdenum or rubidium (Roesch & Filosofov, 2010) The primary

long-lasting pollutant in ^{68}Ge production is zinc-65 (^{65}Zn), with a half-life of 244 days.

Commercial generators distributed today are solid phase based and use hydrochloric acid to separate produced ^{68}Ga regardless of phase type. The commercial $^{68}\text{Ge}/^{68}\text{Ga}$ generator with column matrices based on titanium dioxide (TiO_2) or tin dioxide (SnO_2) is the most widely used generator. Commercially produced $^{68}\text{Ge}/^{68}\text{Ga}$ generators are available from certain manufacturers; PARSIsootope (Iran), Eckert&Ziegler (Isotope Products-Germany), iThemba Labs (South Africa) and JSC (Obninsk Cyclotron Ltd.). Generator eluates obtained with hydrochloric acid provide ionic ^{68}Ga ($^{68}\text{GaCl}_3$). The existence of cationic species has been proved by electrophoretic analysis (Roesch F. , 2012). The efficiency of the ^{68}Ga generator spontaneously decreases. The presence of ^{68}Ga degradation product Zn(II) and the presence of non-radioactive metals such as Fe(III) , which are considered to be common chemical impurities, reduce the generator elution efficiency.

One of the advantages of $^{68}\text{Ga}/^{68}\text{Ge}$ generators is that they become an ideal and useful product in many aspects. If we list other advantages;

- Efficient separation of parent/daughter elements of $^{68}\text{Ge}/^{68}\text{Ga}$ generator.
- The long physical half-life of ^{68}Ge (allows rapid regrowth of ^{68}Ga after generator flushing).
- Long shelf life.

- Pyrogen-free and the sterile output of product from the generator.
- The versatile chemistry of ^{68}Ga .
- Suitable for automation and kit preparation.

2. GALLIUM-68 CHEMISTRY

The three basic components that make up the radiopharmaceutical; is a vector molecule, a radionuclide and a linker between them. While the radionuclide provides the radioactivity (radiation component); the vector molecule targets biomolecules in specific tissues and cells. Although the coordination chemistry of ^{68}Ga is the first effective factor in peptide / macromolecule binding, the chemistry of the vector and the chemistry of the chelator molecule also have an effect on the labeling efficiency.

2.1. Gallium-68 Complex Chemistry

According to the Pearson's acid-base concept, the Ga(III) cation is characterized as a hard acid due to the high charge density of the positive ion (+3). Formation of a chelate depends on the size of the center cation and the electron configuration. Due to its small size, the Ga(III) cation also prefers chelates containing five-membered rings and forms the stable complex with hard donors. Besides five ring chelates, sets of $\text{N}_x\text{O}_y\text{S}_z$ with four, five and six coordinates are also known. Some of these are stabilized by strong binding interactions between sulfhydryl (thiol) donor groups and the metal core. This is due to the electron configuration (i.e. completed d orbitals) and the presence of interactions between these electrons and the empty

orbitals of the sulfur shell. Ga(III) can form stable complexes with soft thiophenol donors (Bandoli, Dolmella, Tisato, Porchia, & Rifosco, 2009). The metal cation in the six-coordinate Ga (III) complexes that provides a stable complex with a filled d10 electron configuration has an octahedral geometry.

The Ga(III) cation is very sensitive to hydrolysis according to its pH values. While there is no hydrolysis below pH 3, cation rapidly forms oxide and hydroxide gallium at values above 3 and inclined to form collidal precipitates. Stable gallate anion ($\text{Ga}(\text{OH})_4^-$) is formed at pH values higher than 7.4. In in vitro experiments, $\text{Ga}(\text{OH})_4^-$ is formed by a clear difference compared to $\text{Ga}(\text{OH})_3$ in gallate anions generated by GaCl_3 (49:1; $\text{Ga}(\text{OH})_4^- : \text{Ga}(\text{OH})_3$). (Bandoli, Dolmella, Tisato, Porchia, & Rifosco, 2009; Harris & Pecoraro, 1983).

Discovered in the 1970s, the anticancer properties of gallium have been studied in many studies since its discovery and its mode of action has been tried to explain (Collery, Keppler, Madoulet, & Desoize, 2002). Ga(III) is easily reduced, similar to Fe(III), thus, its participation in redox reactions is prevented. This property supports cellular absorption of Ga(III) wherever gallium is needed in some proteins, particularly cancer cells. This natural similarity between Fe (III) and Ga (III) increases the affinity of high-spin Ga (III) to the iron carrier protein apo-transferrin.

2.2. Gallium-68 Labelling Chemistry

There are many studies on fast labeling with various chelators, especially at room temperature, considering generator impurities and labeling environment (Velikyan, 2015; Loktionova, Belozub, Filosofov, & Zhernosekov, 2011; Uğur, Yaylali, & Yüksel, 2021). In many studies conducted so far, the effect of parameters such as reaction temperature, impurity of generator eluate, pH and metal ion-ligand ratio on labeling efficiency with Ga(III) has been investigated. (Velikyan, 2015; Hancock & Martell, 1989).

+ 3 valence radiometals generally cannot form direct complexes with peptide or protein biomolecules, and this type in order for biomolecules to form a complex with radiometals, they must be with auxiliary agents such as chelates. There are two basic requirements for chelate selection. First and foremost, the radiometal-chelate complex has a high stability in the biological environment that cannot be separated from each other. Second, the chelating properties are not lost during the formation of the chelate-peptide complex (Sosabowski & Mather, 2006) . Some chelates that form a thermodynamically stable complex with Ga (III) have been described as bifunctional chelating ligands (bfcs) (Hancock & Martell, 1989). Bfcs should form conjugation with macromolecules (protein, antibody, etc.) on the one hand and radionuclides ($^{99\text{m}}\text{Tc}$, ^{68}Ga , ^{111}In etc.) on the other hand. (Jurisson, Berning, Jia, & Ma, 1993). Examples of very bi-functional chelating agent commonly used in ^{68}Ga labeling are 1,4,7,10-Tetraazacyclododecane-1,4,7,10-tetraacetic acid (DOTA), 1,4,7-

triazacyclononane-N, N', N''-triacetic acid (NOTA) derivatives (fig 1). An illustrative example of Ga (III) with bfc is the 1,4,7,10-Tetraazacyclododecane-1,4,7,10-tetraacetic acid (tetraxetan, DOTA) ligand. The advantage of DOTA is that it can be potentially used for both diagnosis and radiotherapy by labeling it with various radionuclides such as ^{68}Ga , ^{90}Y or ^{177}Lu . The main reason for this is that these bifunctional chelating agents rapidly form stable octahedral chelate complexes with Ga(III).

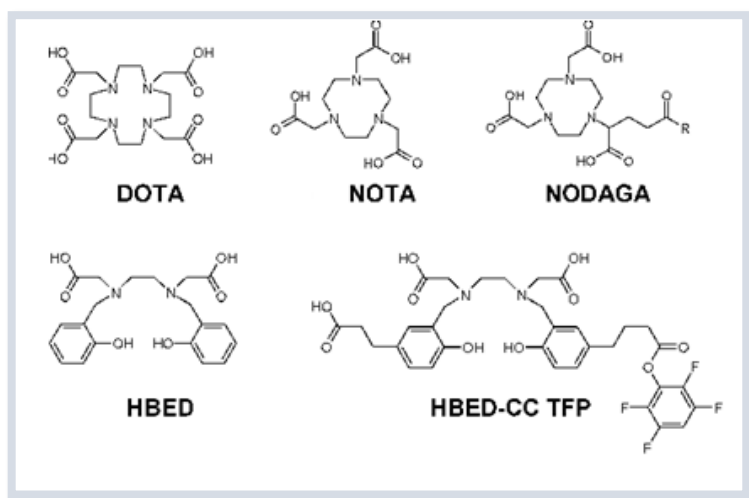


Figure 1. Structures of some ^{68}Ga chelators (Berry, Ma, & Ballinger, 2011)

Acyclic (HBED-CC) and macrocyclic (NOTA and DOTA) chelating agents are known to form thermodynamically kinetically stable inert metal chelates. Although radiometal-DOTA complexes have higher thermodynamic and kinetic stability than radiometal-DTPA complexes, the complex formation rate of radiometals with DOTA is slower and more difficult (Kukis, DeNardo, & DeNardo, 1998).

Worldwide clinical trials of ^{68}Ga labeled ligands PSMA-617 and PSMA-11 for prostate cancer imaging are still ongoing.

2.2.1. Factors affecting ^{68}Ga labeling

- **Effects of pH:** The most important factor in labeling efficiency with ^{68}Ga is pH. The Ga (III) ion hydrolyzes rapidly at values above pH 4, and the gallium cation rapidly forms oxide and hydroxide derivatives. The stable gallate anion $\text{Ga}(\text{OH})_4^-$ occurs at pH levels higher than 7.4 (Jackson & Byrne, 1996). Complex formation is prevented at low pH values. The high concentration of H^+ in solution generally tends to hydrolyze even stable complexes.
- **Effects of Buffer:** $^{67}\text{Ga}(\text{III})$ and $^{68}\text{Ga}(\text{III})$ are commonly labeled as $[\text{Ga}(\text{H}_2\text{O})_6]^{3+}$ in buffer solution at slightly acidic conditions between pH 2.8-3.8. Commonly used buffers are ammonium acetate, citrate buffer and HEPES (4- (2-hydroxyethyl) -1-piperazineethanesulfonic acid). These buffer compounds are used to protect Ga(III) from sudden hydrolysis by rapidly forming metastable complexes with Ga(III). At the same time, antioxidants such as ascorbic or gentisic acid are added to the reaction bottle to prevent radiolysis of the peptide. When the pH is 3 and above in the labeling process, if the buffer solution is not used, the formation of Ga (III) hydroxide and oxide species begins, sometimes insoluble gel-like colloids are observed (Roesch & Riss, 2010).

- Effects of temperature:*** The complexation reaction of ^{68}Ga with the macrocyclic chelator conjugated to the peptide begins at room temperature. HBED-CC, one of the acyclic complex ligands, is a urea-based PSMA inhibitor, a chelator suitable for room temperature radiolabeling with ^{68}Ga produced by the generator. Complex formation yields of the HBED chelator with ^{68}Ga are relatively low at ambient temperature (25°C- 40°C), and complex formation is obtained in 40% after 10 minutes reaction time (Eppard, Homann, de la Fuente, Essler, & Rösch, 2017). On the contrary, at high temperatures of 60°C to 90°C, the efficiency and complex formation kinetics are high and fast. There are studies showing that optimum labeling is made NODAGA and PSMA11 at 30°C, DOTATOC and DOTANOC at 95°C (25). It is known that ^{68}Ga -peptide labeling is incubated at ~ 4 pH with a standard labeling protocol and reaches maximum complexing efficiency in the temperature range of 90-100° C (Eppard, Homann, de la Fuente, Essler, & Rösch, 2017; Reverchon, Khayi, Roger, Moreau, & Kryza, 2020).
- Effects of generator eluate:*** Commercial generators used today are solid phase based as we mentioned earlier and use hydrochloric acid to decompose ^{68}Ga produced regardless the type of solid phase. Radioactive labeling procedures with ^{68}Ga are affected by the presence of some metals (Velikyan, 2015). Metal contamination can affect radioactive labeling processes that require high specific activities. Metals present during the radiolabeling reaction can bind to peptide ligands, resulting in

the formation of non-radioactive peptides. These peptides can compete with ^{68}Ga labeled peptides at the receptors. When examining generators in terms of their characteristics, first of all, the differences in HCl concentrations required to operate the generator draw attention. They are then evaluated for ^{68}Ga elution, frequency of use or physical half-life and ^{68}Ge excretion. Although the generator is used in principle for at least one year, the lifetime of the generator may not be parallel to this half-life. The efficiency of the ^{68}Ga generator spontaneously decreases and with the increase of ^{68}Ge (Velikyan, 2015; Roesch & Riss, 2010), it starts to give non-optimal performance. The presence of Zn(II) formed by ^{68}Ga degradation and the presence of non-radioactive metals such as Fe(III), which are considered as general chemical impurities, reduce the generator elution efficiency. Whichever generator is used, the large eluate volume, slow complexation, and the presence of metallic impurities such as Zn^{2+} , Ti^{4+} , Sn^{2+} , Mn^{2+} and Fe^{3+} , which can make labeling difficult with $^{68}\text{Ga}^{3+}$, compete with the chelator, reducing the labeling efficiency. For widespread use of ^{68}Ga generators in nuclear medicine routine, minimum chemical purity determination and radiochemical efficiency should be considered.

CONCLUSION

Molecular imaging is not only good imaging in Nuclear medicine, it is also considered the center of routine patient management in personalized medicine of the future. Molecular imaging is a new initiative with the production of drugs suitable for targeted tissues. However, various regulations, financial and practical obstacles to be overcome must be overcome to achieve this goal. ^{68}Ga labeled drug applications are believed to have a new future with current knowledge and techniques. While the ^{68}Ga radionuclide is used in diagnostic practice, it is important to know the chemistry of the radionuclide, its complexing kinetics and labeling chemistry to maximize the potential of the radiopharmaceutical.

One measure of the physicochemical parameters is the stability, the stability of the ^{68}Ga -complex formed in in vitro aqueous solution. Ligand binding and metal cation exchange processes (Fe, Zn, Cu, Ca, etc.) of the purified complex in saline are important for stability.

Research articles from all areas of ^{68}Ga -based radiopharmaceutical chemistry are followed with interest and there is a continuous increase in publications. In this study; the variety of complexation with generator eluate, labeling reagents and ligand has been studied chemically, radiochemically and physicochemically.

REFERENCE

- Bandoli, G., Dolmella, A., Tisato, F., Porchia, M., & Rifosco, F. (2009). Mononuclear six-coordinated Ga(III) complexes: A comprehensive survey. *Coord. Chem. Rev.*, 253, 56-77.
- Berry, D., Ma, Y., & Ballinger, J. e. (2011). Efficient bifunctional gallium-68 chelators for positron emission tomography: tris(hydroxypyridinone) ligands. *Chem Commun*, 7;47(25);7068-70.
- Chitambar, C. (2010). Medical Applications and Toxicities of Gallium Compounds. *Int. J. Environ. Res. Public Health*, 7; 2337-2361.
- Collery, P., Keppler, B., Madoulet, C., & Desoize, B. (2002). Gallium in cancer treatment. *Crit. Rev. Oncol. Hematol.*, 42(3):283-296.
- Eppard, E., Homann, T., de la Fuente, A., Essler, M., & Rösch, F. (2017). Optimization of Labeling PSMAHBED with Ethanol-Postprocessed ⁶⁸Ga and Its Quality Control Systems. *J Nucl Med.*, 58(3):432-437.
- Hancock, R., & Martell, A. (1989). Ligand design for selective complexation of metal ions in aqueous solution. *Chem. Rev.*, 89;1875-1914.
- Harris, W., & Pecoraro, V. (1983). Thermodynamic binding constants for gallium transferrin. *Biochem*, 22, 292-299.
- Jackson, E., & Byrne, M. (1996). Metal ion speciation in blood plasma: Gallium-67-citrate and MRI contrast agents. *J. Nucl. Med.*, 37, 379-386.
- Jurisson, S., Berning, D., Jia, W., & Ma, D. (1993). Coordination compounds in nuclear medicine. *Chem. Rev.*, 93,3; 1137-1156.
- Kukis, D., DeNardo, S., & DeNardo, G. (1998). Optimized conditions for chelation of ⁹⁰Y-DOTA- immunoconjugates. *J Nucl Med.*, 39, 2105-10.
- Kumar, K. (2020). The Current Status of the Production and Supply of Gallium-68. *Cancer Biother Radiopharm*, 35(3):163-166.
- Loktionova, N., Belozub, A., Filosofov, D., & Zhernosekov, K. e. (2011). Improved column-based radiochemical processing of the generator produced ⁶⁸Ga. *Appl. Radiat. Isot.*, 69, 942–946.

- Magnum, B., & Furukawa, G. (1990). Guidelines for Realizing the International Temperature Scale of 1990 (ITS-1990). *NIST Technical Note 1265 (U.S. Government Printing Office, Washington, D.C.)*, 5.
- Meija, J., Coplen, T., Berglund, M., Brand, W., & et.al. (2016). Atomic weights of the elements 2013 (IUPAC Technical Report). *Pure Appl. Chem.*, 88(3): 265-91.
- Meinkin, G., Kurczak, S., Mausner, L., Kolsky, K., & Srivastava, S. (2005). Production of high specific activity ^{68}Ge at Brookhaven National Laboratory. *J Radioanal Nucl Chem*, 263:553–557.
- Pharmacopeia, E. (2011). *01/2013:2482 Gallium (^{68}Ga) Edotreotide*. Eur Pharm.
- Pharmacopeia, E. (2013). *Gallium (^{68}Ga) chloride solution for radiolabelling*. European Directorate for the Quality of Medicines.
- Preston–Thomas, H. (1990). The International Temperature Scale of 1990 (ITS-90), *Metrologia* , 27, 3-10.
- Reverchon, J., Khayi, F., Roger, M., Moreau, A., & Kryza, D. (2020). Optimization of the radiosynthesis of ^{68}Ga -PSMA-11 using a Trasis MiniAiO synthesizer: do we need to heat and purify? *Nucl Med Commun.*, 41(9):977-985.
- Roesch, F. (2012). Maturation of a key resource – the germanium-68/gallium-68 generator: development and new insights. *Curr Radiopharm*, 5:202–211.
- Roesch, F., & Filosofov, D. (2010). Production, radiochemical processing and quality evaluation of ^{68}Ge . *IAEA Radioisot Radiopharm Se*, 2:11–30.
- Roesch, F., & Riss, P. (2010). The Renaissance of the $^{68}\text{Ge}/^{68}\text{Ga}$ Radionuclide Generator Initiates New Developments in ^{68}Ga Radiopharmaceutical Chemistry. *Current Topics in Medicinal Chemistry*, 10, 1633-1668.
- Sosabowski, J., & Mather, S. (2006). Conjugation of DOTA-like chelating agents to peptides and radiolabelling with trivalent metallic isotopes. *Nature Protocols*, 1, 972-976.
- Uğur, A., Yaylali, O., & Yüksel, D. (2021). Examination of metallic impurities of $^{68}\text{Ge}/^{68}\text{Ga}$ generators used for radioactive labeling of peptides in clinical PET applications. *Nucl Med Commun.*, 42(1):81-85.

- Velikyan, I. (2015). Continued rapid growth in Ga applications: Update 2013 to june 2014 . *J. Label. Compd. Radiopharm.*, 99–121.
- Velikyan, I. (2014). Prospective of ⁶⁸Ga-Radiopharmaceutical Development. *Theranostics*, 4(1):47-80.
- Velikyan, I. (2015). ⁶⁸Ga-Based Radiopharmaceuticals: Production and Application Relationship. *Molecules*, 20; 12913-12943.

CHAPTER 3

BODIPY-BASED FLUORESCENT CHEMOSENSORS

Dr. Seda CETINDERE¹
Dr. Semiha YILDIRIM SARIKAYA²

¹ Gebze Technical University, Faculty of Science, Department of Chemistry, Kocaeli, Turkey. sdemirer@gtu.edu.tr <https://orcid.org/0000-0001-7599-8491>

² Karabük University, Faculty of Science, Department of Chemistry, Karabük, Turkey. semihayildirim@karabuk.edu.tr <https://orcid.org/0000-0002-5993-3660>

INTRODUCTION

Chemosensors can be defined as devices used for detecting the presence of specific chemical molecules with accompanying alternate in one or more characters such as color, fluorescence or the potential of redox in a media (Rani, 2015). Chemosensors comprise of three constituent: a chemical receptor that can usually recognize the interesting guest with high particularity, a converter that transforms the binding event into a commensurable physical change, and the procedure of measurement this change and turning it into useful knowledge (Figure 1).

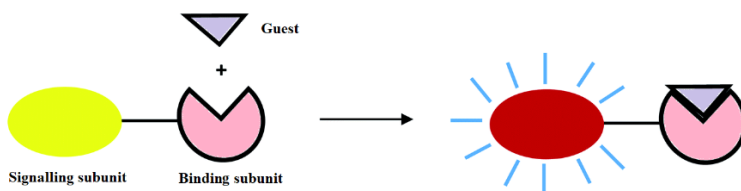


Figure 1: Binding Of An Analyte (guest) By A Chemosensor (host), Producing A Complex With Altered Optical Properties.

Luminescence, optical absorption, redox potential, etc., are the most popular applications used in the sensors of chemicals, but these sensors based on other spectroscopies as well as optical parameters such as the reflectivity and refractive index have also been developed. The improvement of fluorescent chemosensors for the unveiling of environmentally and biologically significant metal ions among known chemosensors has allured stable attention in variant areas such as materials, chemistry, environmental and biological sciences by the reason of the plain use, low cost, high certainty and definitiveness, concurrent monitoring and minimum response time (Quang & Kim,

2010; J.F. Zhang, Zhou, Yoon & Kim, 2011; Kim, Ren, Kim & Yoon, 2012; Sahoo, Kim & Choi, 2016; Jeong & Joo, 2012; Kaur & Kumar, 2011). Upon interactive relation with the metal ions, the intensity of fluorescence and/or the chemosensors' fluorescence band shift converts, and the ions of metal may be determined quantitatively and qualitatively (Chandrasekhar, Bag & Pandey, 2009). The three kinds of chemosensors, namely "off-on" and "on-off", "ratiometric" are classified in compliance with their changes of the fluorescence signal, and each kind is further divided into numerous parts in compliance with their structure of molecule characteristics and/or mechanisms' recognition. 'Off-on' and 'on-off' and chemosensors' fluorescent rely on alterations in intensity of emission in a particular wavelength, and these are instrumental efficiency, microenvironment and chemosensor concentration. On the contrary, proportional fluorescent chemosensors proves alteration proportion to emission intensities at two divergent wavelengths, and can be used to assess analyte concentration and ensure a built-in rectification for the effects of the environmental (Wu, Li, Li, Tang & Liu, 2014; Coskun & Akkaya, 2015).

1. FLUORESCENT CHEMOSENSORS

Fluorescent chemosensors are described as combined that contain a fluorophore, a binding site, and a mechanism for transmission between the two sites (Czarnik, 1994). In a number of areas, including environmental chemistry, analytical chemistry, and bio-medical science, fluorescent chemosensors are extremely useful. These provide reliable and low-cost characterization with high particularity and

sensitivity of toxic heavy metal ions, enzymes and anions. The first fluorescent chemosensor was notified in 1867. A process for determining aluminum ions (Al^{3+}) by forming a powerful fluorescent morine chelate was described in this report (Czarnik, 1993; Czarnik, 1994). This led to a sequence of fluorescent chemosensors being improved in order to the assignation of many other metal ions. Early experiments on fluorescent chemosensors intened initially on the estimation of metal ions rather than the estimation of anions or neutral species, since the selective binding of metal ions in water is considerably easier than that of neutral species or anions (Sousa & Larson, 1977; Konopelski, Kotzyba-Hibert, Lehn, Desvergne, Fages, Castellan & Bouas-Laurent, 1985; de Silva & de Silva, 1986; Grynkiewicz, Poenie & Tsien, 1985; Huston, Haider & Czarnik, 1988). Fluorescent chemosensors were widely developed following these pioneering days (de Silva *et al.*, 1997; Yang, Zhao, Feng & Li, 2013; Li, Gao, Shi & Ma, 2014). Compared to other biological detection techniques, fluorescent chemosensors have been used as an important technique to detect a number of intracellular reactive species because of their obvious benefits, such as high sensitivity and selectivity (Wang, Li, Yu, Song, Sun, Yang, Lou & Han, 2013; Wang, Yu, Li & Shao, 2015; Chen, Tian, Kallio, Oleson, Ji, Borchardt, Jiang, Remington & Ai, 2016; Wang, Zhu, Jiang, Hua, Na & Li, 2017). The development of fluorescent chemosensors for different analytes has been actively maintained by chemists. On the other hand, because of the high levels of sensibility and particularly capability of them to be used for temporal and spatial exemplification for in vivo imaging applications, they have

been generally used in a variety of fields such as, pharmacology, biology, and environment (Wu, Sedgwick, Gunnlaugsson, Akkaya, Yoon & James, 2017). Fluorescent chemosensor detection of an analyte is normally accomplished by one or more standard photophysical processes, such as intramolecular charge transfer (ICT), photoinduced electron transfer (PET), etc. (de Silva, Gunaratne, Gunnlaugsson, Huxley, McCoy, Rademacher & Rice, 1997; Daly, Ling & de Silva, 2015). These mechanisms have been utilized in the search for longer wavelength emission, higher quantum yields and higher signal response. Currently, many fluorescent chemosensors use “turn-on” methods, with advantages in terms of their reliability, as well as freedom from background noise, compared with “turn-off” fluorescent sensors. In this case, strategies, such as PET, ratiometric approaches, and Fluorescence Resonance Energy Transfer (FRET) can be employed to control the “turn-on” and “turn-off” behavior of a luminescent system.

2. FLUORESCENCE CHARACTERISTICS OF BODIPY DYES

Boron-dipyrromethene (BODIPY) dyes (Figure 2), which were first discovered in 1968, are compounds that are rapidly increasing in importance among fluorescent organic dyes today (Treibs & Kreuzer, 1968). These dyes possess unique photophysical properties like high quantum yields of fluorescence (generally between 60 and 90 %), long excited state lifetimes (around 1 to 10 ns), large molar absorptive coefficients (generally in the region of 40000 to 112000 M⁻¹cm⁻¹ and small Stokes shifts (about 10 nm) (Yao, Xiao & Dan, 2013). Also they

have good solubility in many organic solvents and high chemical stability and photostability. The fact that BODIPY dyes are one of the most important characteristics is that their optical properties can be changed by changing the molecular backbone (Ulrich, Ziesse, Harriman, 2008; Bozdemir, Guliyev, Buyukcakil, Selduk, Kolemen, Gulseren, Nalbantoglu, Boyaci & Akkaya, 2010). BODIPY derivatives can emit in different regions of the electromagnetic spectrum (Figure 3). Thus, different BODIPY derivatives can be screened largely, which causes a considerable expansion of the area of use (Laudet & Burgess, 2007). BODIPY dyes are usually immune to aggregation in a solution. Due to the intense transitions corresponding to the $S_0 - S_1$ phase and the absorption from S_0 to S_2 states, together with the fine structure with net vibration, the absorption spectra registered in the solution exhibit a more modest set of transitions. Characteristic of $C = C$ bond system of the BODIPY nucleus, both transitions typically display a fine vibration structure in the range of 1200 to 1400 cm^{-1} . Strong fluorescence from S_1 state is tracked when excited in either of the S_1 or S_2 states, which indicates good mirror symmetry with the lowest energy absorption band. No fluorescence was tracked from the S_2 state and the internal transformation seems to be quantitative (Ulrich *et al.*, 2008). BODIPY's absorption and fluorescence behaviors are excessively affected by the extent of the delocalization's electron around the core and throughout conjugated substituents and because of this, their particular photophysical characteristics can be tuned (Laudet *et al.*, 2007).

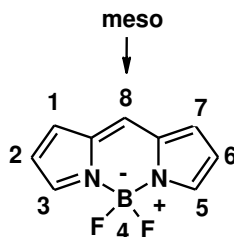


Figure 2: Structure And Numbering Of BODIPY Core.

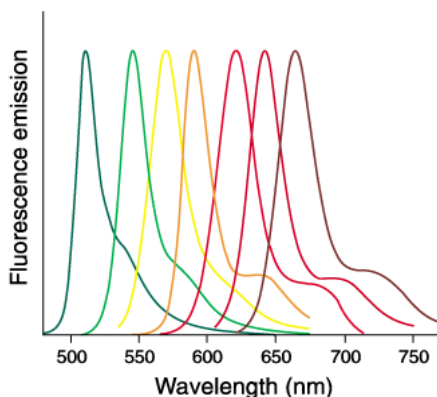


Figure 3: Fluorescence Emission Graphs Of Different BODIPY Dyes

3. BODIPYS AS FLUORESCENT CHEMOSENSORS

Fluorescence detection technology has the characteristics of high sensitivity, good selectivity, low cost, easy operation and wide application and it has taken a place in the field of chemical and biological analysis. The core of fluorescence detection technology lies in the performance of high-performance fluorescent dyes directly affects the accuracy and sensitivity of detection, so finding fluorescent dyes with excellent performance is of great significance for the development of chemical and biological analysis technology. Among these fluorescent dyes because of their excellent optical properties,

BODIPY dyes have been extensively used as the chemosensors of fluorescent for the assignation of cations and anions in different applications in recent years (Isaad & Achari, 2020; Kursunlu, Ozmen & Güler, 2019; Xue, Liu & Liu, 2019; Haldar & Lee, 2019; Gao, Chen, Chen, Meng, Wang, Li & Feng, 2019; 35. Haldar, Sharma, Ruidas & Lee, 2020; Li, Cao, Hu, Li, Meng, Han & Ma, 2019; Li, Han, Sun, Shana, Ma, He, Merguc, Park, Kim & Son, 2020). For the BODIPY-based fluorescent chemosensors, different ligand groups for the illumination of the photophysical and photochemical properties prepared the BODIPY derivatives. The synthesized BODIPY-based fluorescent chemosensors have remarkable photophysical properties, such as intense absorption in the visible and near-IR ranges high molar absorption coefficient, a high quantum yield, long excited state lifetimes etc. Moreover, these chemosensors were successfully implemented on living organisms for the detection of analytes. After chemically modifying the basic structural unit of BODIPY, it can be made into a fluorescent probe that can achieve specific functions in the body. Fluorescent probes are mainly composed of structural units such as recognition groups, link arms and fluorescent chromophores. In recognition when detecting the object, the photophysical properties of the fluorescent chromophore affected, the output form of the fluorescence signal changes, such as the shift of the fluorescence peak position, the fluctuation of the fluorescence quantum yield and the appearance of new fluorescence peaks, etc., so the fluorophore can play the role of information conversion, that is, the identification information is converted into fluorescence signal, the mechanisms

involved in this conversion process mainly include PET, ICT, and FRET, *etc.* (Figure 4-6). Following three more widely used approaches: displacement, binding site signaling unit and chemodosimeter, the BODIPY core has been successfully used in the chemosensors' design. Fluorescent responses depending on the position of the reactive unit in the BODIPY nucleus has been obtained. In most cases, analyte-induced alterations may be tracked with the naked eye. You can detect anions, cations, and neutral molecules in various environments: aqueous or organic. In biological applications, the biocompatibility of many of these compounds enables them to be used.

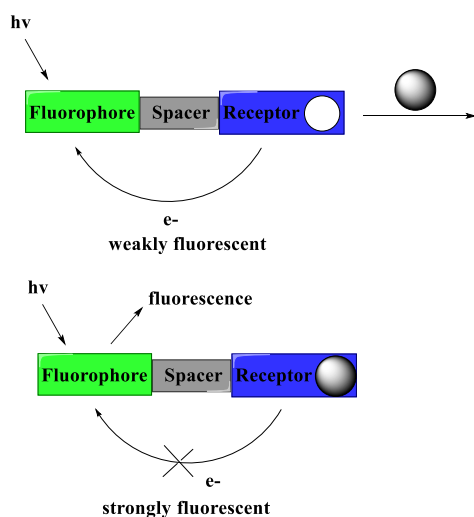


Figure 4: ‘Turn-on’ Sensing Mechanism Of PET Sensors

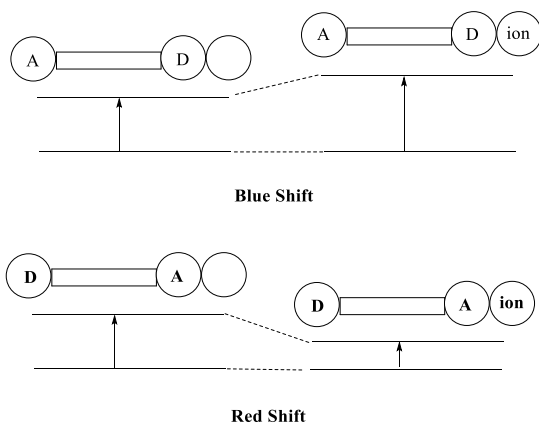


Figure 5: ICT Fluorescent Sensors And Sensing Mechanisms

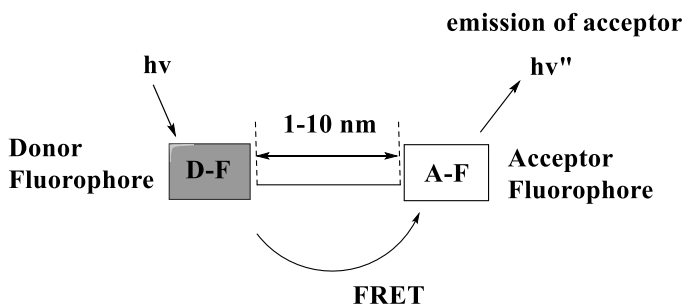


Figure 6: Fluorescence Mechanism Of FRET Sensors

4. BODIPY-BASED SENSORS FOR METAL CATIONS

Metal ions play a major role in some chemical and biological processes at the cellular level to a limited concentration. Some of them play a critical role in a variety of enzymatic processes, vital activities and biochemical processes in the human body, and various environmental cycles. An enhancement in the concentration of some metal ions beyond their permissible limit may lead to diverse neurological sicknesses like the disease of Wilson, the disease of Alzheimer, the disease of prion, and Menkes to humans (Gul, 2020). There are various conventional

analytical techniques for the metal ions' detection and these techniques often require samples of large size and not suitable for quick and online monitoring. Besides, these methods are time-consuming and complicated; they need expensive instruments for analysis. In contrast to this, the techniques based on fluorogenic and colorimetric sensors offer some important advantages such as selectivity, sensitivity, simplicity, the capability of real-time analysis, response time, cost-effectiveness, and the local observation by using fluorescence imaging spectroscopy (Gul, 2020).

As it was mentioned above, fluorescent sensors are classified as turn-off, turn-on, ratiometric, these are quenched, enhanced and target analyte respectively (Zhu, 2015). In this chapter we summarize some of the BODIPY-based fluorescent probes for the detection of transition metal cations (e. g. Fe^{2+} , Fe^{3+} , Zn^{2+} , Cd^{2+} , Cu^{2+} , Pt^{2+} , Al^{3+} , Hg^{2+} , Ag^+ , Cr^{3+}) and the alkali and alkaline earth metal cations (e. g. Na^+ , Cs^+ , and Ca^{2+}).

4.1. Turn-on Fluorescent BODIPY Probes

Tang and co-workers discovered a fluorescent chemosensor (**1**) with high selectivity for Pt^{2+} (Figure 7). The detection of Pt^{2+} by the probe could work in aqueous medium in the pH range of 5-10. The probe bind to Pt^{2+} in a 1:1 ratio and complex formation caused strong green fluorescence at 520 nm based on the PET mechanism. The selectivity performance showed that (**1**) was applicable to distinguish Pt^{2+} from other relevant soft metal ions (Tang, 2020).

A water-soluble fluorescence turn-on chemosensor (**2**) consisting of BODIPY fluorophore functionalized with a dicarboxylate pseudo-crown ether receptor was developed by Maity et al. Selectively detecting Cd^{2+} in aqueous sample over other related metal ions by mediating the PET process (Figure 7). At 512 nm after excitation, the free chromophore displays a very small fluorescence band ($\Phi_F = 0.057$). After Cd^{2+} was applied, the fluorescence intensity increased significantly (almost $\Phi_F = 0.43$) by approx. Four folds of the emission wavelength with a negligible red change (about 2 nm) could be monitored. A visually visible colour shift to brilliant green was also monitored, under UV light at 365 nm by the naked eye. Fluorescence titration results indicated 1:1 metal-ligand stoichiometry, fluorescence life time was found to be 3.81 ns (Maity, 2019).

A water-soluble, BODIPY-added, and semicarbazone-based polymeric chemosensor (**3**) was reported by Haldar and co-workers for selective detection of Hg (II) ions. (Figure 7). In presence of (**3**) at pH 7.4 (detection time ~ 72 s) in pure aqueous media, Hg (II)-ion-induced turn-on fluorescence was easily obtained. A negligible blue shift (~ 4 nm) upon addition to it of Hg (II) ions is showed for the absorption maximum of solution of (**3**). Whereas, a new emission band that induced the solution to achieve a brilliant yellow colour seemed at 545 nm ($\Phi_F = 0.17$). Limit of detection (LOD) for (**3**) was found as $0.37 \mu\text{M}$ (Haldar, 2019).

Kursunlu improved a fluorescent sensor (**4**) for monitoring Al^{3+} (Figure 7). Within a methanol/water (9/1, v:v) solutions, sensor (**4**) created a

1:2 complicated with Al^{3+} resulting a remarkable increasing in fluorescence intensity owing to ICT effect. Suitable pH range for Al (III) ion sensing was determined as 4-7 and LOD was found to be 1.8×10^{-8} M (Kursunlu, 2015).

Three bichromophoric compounds (**5**, **6**, **7**) consisting BODIPY and anthracene fragments attached by variant spacers were synthesized by Saura and co-workers (Figure 7). The compounds showed communication of interchromophoric by way of Electronic Energy Transfer (EET). The fluorescence of the compounds in an aqueous environment was pH sensitive, a typical behavior of PET probes. A turn-on response to Cu^{2+} in water at neutral pH was found in the presence of several metallic cations studied (Cu^{2+} , Ni^{2+} , Cd^{2+} , Zn^{2+}) (Saura, 2017).

Sui et al. reported a highly water soluble BODIPY-based fluorescence switch-on sensor (**8**) for Ca^{2+} (Figure 7). Its selectivity as a Ca^{2+} sensor was investigated in the 30 mM HEPES buffer (pH 7.4). The particularity high-energy unbound electron pair of the Ca^{2+} receptor's electronegative nitrogen atom will carry an electron to the excited fluorophore in the absence of Ca^{2+} , the fluorescence is thereby quenched by PET treatment. After Ca^{2+} (1: 1) bound, PET treatment from Ca^{2+} receptor to fluorophore was attenuated and the fluorophore showed an increase in fluorescent emission signal at 511 nm. It was determined that the dissociation constant (K_d) of the sensor was 0.92 mM, which is very similar to the extracellular level of Ca^{2+} (Sui, 2016).

A fluorescent sensor (**9**) was developed by Xiao and co-workers to evaluate Hg^{2+} (Figure 7). The formation of complex (**2**)- Hg^{2+} (1:1) induced outstanding fluorescence enhancement induced by Hg^{2+} (almost 249-fold) at 515 nm in the EtOH/tris-HCl (v/v, 1/9) medium pH of 7.3, with quantum yields increasing from 0.007 to 0.58. Only Al^{3+} provided a poor response to the addition of other metal ions. The Hg^{2+} binding constant (K_a) of the probe was determined to be $9.43 \times 10^4 \text{ M}^{-1}$ and LOD was assessed to be as low as $1.73 \text{ }\mu\text{M}$ (Xiao, 2015).

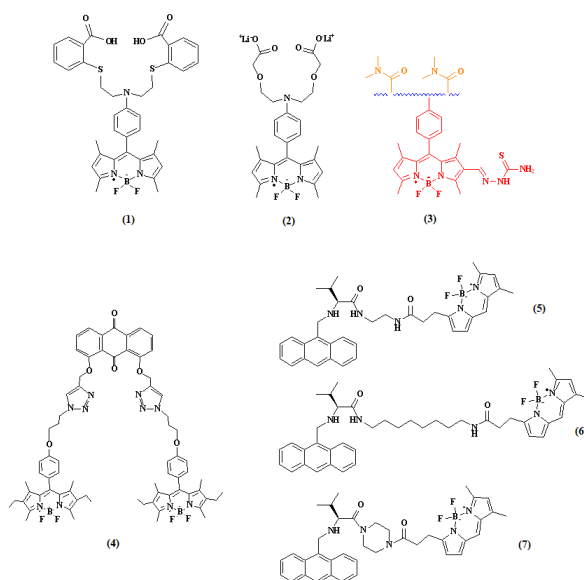


Figure 7: Structures Of Turn-on Fluorescent BODIPY Probes

4.2. Turn-off Fluorescent BODIPY Probes

A BODIPY-based turn-off fluorescent probe (**10**) for the detection of the selective of Cs^+ ions was developed by Özcan and Çoşut (Figure 8). In a DMSO/water (9:1, v/v) solutions, sensor- Cs^+ formation complex (1:1) caused significant decreases in both fluorescence and absorption

intensities. To evaluate the binding abilities of **(10)**, various metal ions (Li^+ , K^+ , Cs^+ , Mg^{2+} , Pb^{2+} , Hg^{2+} , Na^+ , Ca^{2+} , Ba^{2+} , Mn^{2+} , Ni^{2+} , Cd^{2+} , Ag^+ , Cu^{2+} , Co^{2+} , Zn^{2+} , Cr^{3+} and Fe^{3+}) were tested. The foreign ions' interference was found to be negligible (Özcan, 2018).

By inserting amide receptors into the BODIPY system, Sun and coworkers synthesized probe **(11)** (Figure 8), and phenolic hydroxyl and carbonyl groups were attached to the skeleton as donors. The coordination between Cu^{2+} and **(11)** caused fluorescence quenching at 510 nm. Also Cu^{2+} addition to the solution of this probe induced a 20 nm bathochromic shift of the absorption maximum in UV region and 2 nm blue shift in visible region. **(11)** replied to Cu^{2+} quickly under near neutral conditions, and indicated good detection ability towards Cu^{2+} in the concentration range of 0.35-7 μM . The fluorescence quantum yield of the probe in EtOH was measured to be 0.06 and the lifetime of fluorescence was 2.03 ns (45.46%), 0.4878 ns (54.54%) (Sun, 2020).

The sensor **(12)** (Figure 8) developed by Herten et al. **(12)**, which combined the bright emission of the recognized BODIPY fluorophore with the sensory activity of bipyridine, was itself strongly fluorescent and displayed an emission band typical for BODIPY derivatives at 517 nm.. Solid quenching due to the PET mechanism of fluorescence emission observed on Cu^{2+} coordination. By adding EDTA, the quenching of Cu^{2+} ions could be reversed (Herten, 2018).

Turn-off fluorescent chemosensors based on the BODIPY adorned with triazine derivatives **(13, 14)** developed by Şenkuytu et al for the detection of silver (Ag^+) ions (Figure 8). These molecules had nitrogen

atoms in three different regions (BODIPY, triazole and triazine rings) that could bind metals. The BODIPY-decorated triazine demonstrated high familiarity and selectivity over other competitive metal ions for silver ions. The complex stoichiometry of the BODIPY-triazines and Ag^+ ions were determined as 3:1 (L/M) for **(13)** and 2:1 (L/M) for **(14)** by fluorescence titrations. Fluorescence emission and maximum absorbance wavelength were tracked 500 and 511 nm ($\Phi_F = 0.60$) for **(13)**, 683 and 720 nm ($\Phi_F = 0.10$) for **(14)** in tetrahydrofuran, respectively (Şenkuytu, 2018).

Çetindere et al. designed hexa-BODIPY substituted triazole linked cyclotriphosphazene **(15)** for the sensitive and selective detection of Fe^{2+} ions (Figure 8). The absorption and emission maxima of **(15)** in THF solution were tracked at 502 and 513 nm, respectively. The formation of complex **(15)**- Fe^{2+} (1:1) caused fluorescence quenching accompanied by changing color from yellow to brown. LOD of **(15)** was calculated as 2.03 μM (0.114 ppm) (Çetindere, 2016).

A " turn-off " fluorescent sensor **(16)** was identified by Kursunlu and co-workers for the selective signaling of Cu^{2+} , consisting of double triazole moieties and BODIPY groups (Figure 8). The photophysical properties of **(16)** were tested in methanol/water (9:1, v/v). Due to suppression of the PET mechanism upon metal binding, an efficient quenching of the fluorescence intensity at 548 nm was enhanced. The fluorescence intensity shift has reported that 8 minutes of reaction time is required to form the complex **(16)**- Cu^{2+} (1:2) (Kursunlu, 2019).

A near infrared (NIR) fluorescent probe based on BODIPY (**17**) was reported by Ji et al. for highly sensible and selective estimation of biologically significant Fe^{3+} in aqueous environment (Figure 8). A pair of side arms of 2-sulfonatostyryl attached as a convertible chelator unique to Fe^{3+} to the BODIPY heart. Because of paramagnetic feature of Fe^{3+} , the NIR fluorescence of (**17**) was fully quenched following disulfonate chelation to Fe^{3+} (LOD as low as $14.2 \mu\text{M}$). In addition, upon the addition of sodium ascorbate as a reduction agent or EDTA as a stronger chelator, the quenched NIR fluorescence was instantly recovered (Ji, 2018).

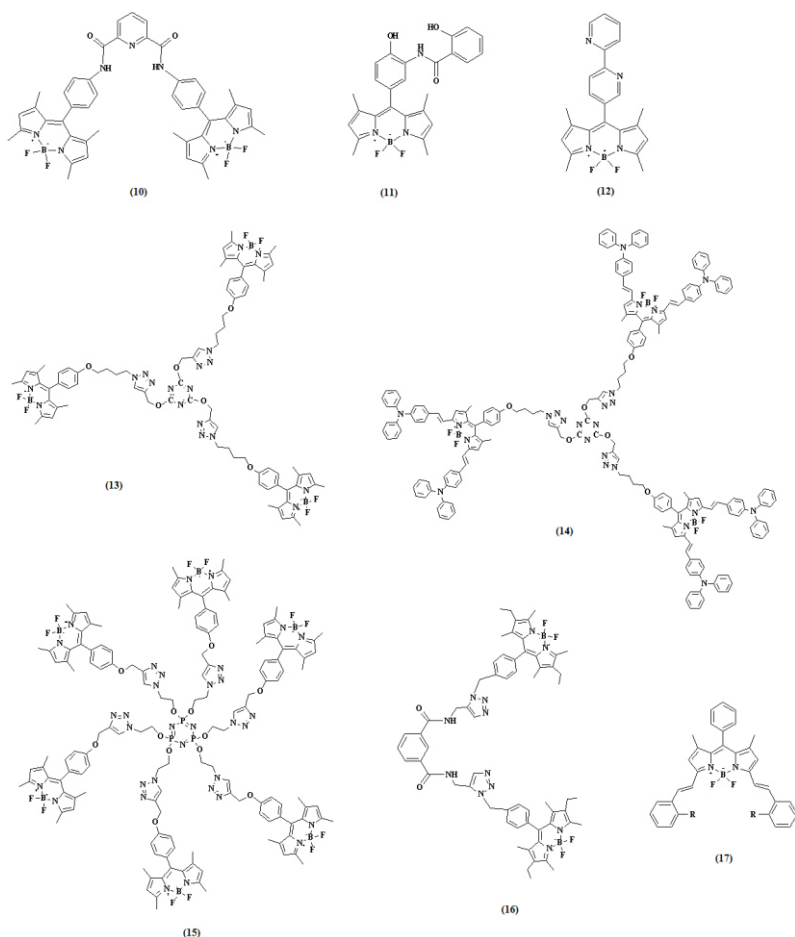


Figure 8: Structures Of Turn-off Fluorescent BODIPY Probes

4.3. Ratiometric BODIPY Probes

Many variables, like as sensor concentration, change of conditions around the sensor (pH, polarity, temperature, etc.) may affect the measurement of fluorescence with a decline or increament in emission intensity without excitation or too much change in the emission wavelength. Proportional measurement, that is, synchronous recording of fluorescence intensities at two wavelengths and estimation of their

ratios, is used to minimize these effects. Various signaling mechanisms such as ICT, excimer / exciplex generation, excited state intramolecular proton transfer (ESIPT), FRET, and throughbond energy transfer (TBET) (Zhu, 2015). By combining the biaryl BODIPY fluorophore with an oligoethyleneglycol bridge serving as a binding site, Yamada and coworkers produced a proportional BODIPY probe (**18**) for Na^+ cations (Figure 9). Using the corresponding perchlorate salt, the spectral response to the addition of alkaline ions was calculated. A characteristic change in maximum absorption to a longer wavelength of 12 nm results from the addition of NaClO_4 . As for other alkali ions, the greater the difference between their ionic radii and Na^+ , the lower the redshift (Yamada, 2005).

A BODIPY-based sensor of near-infrared distyryl (**19**) carrying a bis(1,2,3-triazole) amino receptor was identified by Huang et al. (Figure 9). In $\text{CH}_3\text{CN}/\text{H}_2\text{O}$ (5:1 v/v), this probe was rigorously bound to Hg^{2+} and Cu^{2+} cations and showed considerably blue-shifted absorption and fluorescence bands due to inhibition of the transfer mechanism of intramolecular charge. When bound to the Hg^{2+} or Cu^{2+} ion, the fluorescence changes of this probe were exactly various, subject to a proportional fluorescence increment (for Hg^{2+}) or a fluorescence quenching mechanism (for Cu^{2+}). To the naked eye, the resulting vibrant color shifts are smoothly noticeable (Huang, 2019).

On the basis of ICT effect, Zhang et al. developed a Ag^+ selecting fluorescent sensor (**20**) (Figure 9). This sensor showed the blue shift of its ICT absorption, ICT emission and excitation caused by Ag^+ , with

the exception of raising its intrinsic emission to 587 nm. LOD of this sensor was obtained to be 17 μM (~ 0.002 ppm). With a colour transition from blue to purple, the **(20)**-doped PVC film demonstrated 1 ppm Ag^+ sensitivity, giving this sensor the ability to sensitively measure Ag^+ in total water solution by naked-eye detection (Zhang, 2018).

Xia and co-workers have identified the identification of zinc ions in solution and living cells by colorimetric and ratiometric fluorescence with a BODIPY-based probe **(21)** (Figure 9). The sample **(21)** shows high absorption at 525 nm and heavy fluorescence emissions at 540 nm ($\Phi_F = 0.67$) in the $\text{CH}_3\text{CN}/0.02$ M HEPES (1:1, v/v, pH 7.0) buffer. A new 580 nm emission band with 40 nm red-shift was achieved with the addition of Zn^{2+} , followed by a color transition from green to salmon pink.. The **(21)**- Zn^{2+} complex (1:1) demonstrated reduced quantum yield of fluorescence (0.52) (Xia, 2018).

Centered on TBET, Cherreddy et al. reported a fluorescent BODIPY-rhodamine dyad probe (Figure 9) which can be used for identification of trivalent metal ions (Al^{3+} , Cr^{3+} and Fe^{3+}). In the aqueous acetonitrile buffer (1:1, acetonitrile/0.01 M tris HCl buffer at pH 7.4), the sample **(22)** alone was yellow and showed two absorption bands based at 374 and 499 nm, respectively. Trivalent ions (Al^{3+} or Cr^{3+} or Fe^{3+}) selectively caused new absorption and emission bands centered at 559 and 585 nm among the different metal ions introduced, explicitly demonstrating the ring opening mechanism of the rhodamine B unit in the probe. In addition, due to the efficient energy transfer from BODIPY to rhodamine with the trivalent metal ion-induced spirolactam

ring opened, a decline in the strength of the BODIPY emission band at 517 nm was observed (Cherreddy, 2016).

Shen and Qian have synthesized a ratiometric fluorescent probe (**23**) (Figure 9) based on the rhodamine B and BODIPY platform for sensing Fe^{3+} and Hg^{2+} ions. The fluorescence spectrum of free probe ($\text{H}_2\text{O}/\text{CH}_3\text{CN}$, 1:1, v/v) showed a single peak at 505 nm. A new emission band was tracked at 575 nm after excitation in the presence of Hg^{2+} and Fe^{3+} ions, which is due to the spirolactam ring opened by the rhodamine device. A shift of color from green to salmon pink was noticed. From titration outcomes, the low LOD was determined with a value of 7.74×10^{-8} M for (**23**)/ Hg^{2+} and 3.91×10^{-7} M for (**23**)/ Fe^{3+} , in severalty. The test was exceptionally sensitive and the detection time was less than 2 s (Shen, 2018).

Cheng and co-workers reported a fluorophore dyad (**24**) as a Hg^{2+} selective fluorescent sensor dependent on FRET from BODIPY to rhodamine B (Figure 9). The fluorescence intensity at around 535 nm was dramatically decreased when Hg^{2+} ions were applied to the sensor solution, and a new red-shifted emission band at 570 nm was formed, resulting in a major color change. The task's plot indicated the probe and Hg^{2+} in a 1:1 binding model to create a complex. Hg^{2+} ions with a very low LOD of 1.56 ppb and very high selectivity against Hg^{2+} ions could be observed by probe (**24**) (Cheng, 2016).

A distyryl-BODIPY based NIR red-shifting the fluorescent of ratiometric probe **(25)** (Figure 9) was stated by Hiruta et al. for Ag^+ and Hg^{2+} detection. In the presence of many metal ions, fluorescence emission spectra of **(25)** were observed in the ethanol/HEPES buffer solution (10 μM , pH = 7,8). Spectral red shifts were tracked with Ag^+ and Hg^{2+} , as predicted, based on the ICT method. Only fluorescence emission rate variations have been observed for other metal cations (Hiruta, 2015).

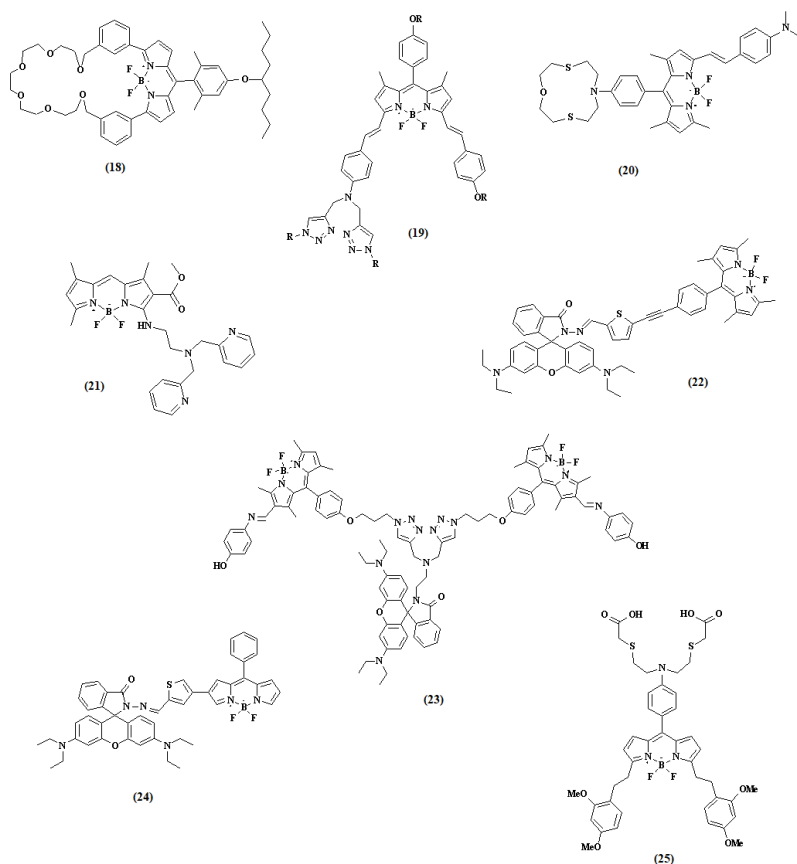


Figure 9: Structures Of Ratiometric BODIPY Probes

CONCLUSION

Some of the BODIPY-based fluorescent probes for transition metal cation detection (e.g. Fe^{2+} , Fe^{3+} , Cu^{2+} , Cd^{2+} , Al^{3+} , Zn^{2+} , Pt^{2+} , Cr^{3+} , Hg^{2+} , Ag^{+}) and alkali and alkaline earth metal cations (e.g. Na^{+} , Cs^{+} , and Ca^{2+}) have been briefly summarized throughout this chapter. BODIPY dyes are very popular as a fluorescent chemosensor especially in last decades, because of their excellent photophysical and photochemical properties. Based on the recent sensor studies on BODIPY dyes, it has seen that they have many applications especially on biological and environmental studies. It appears that BODIPY dyes are still an opened door for better more efficient derivatives and will stay popular in the future.

REFERENCES

- Bozdemir, O. A., Guliyev, R., Buyukcakir, O., Selcuk, S., Kolemen, S., Gulseren, G., Nalbantoglu, T., Boyaci, H., Akkaya, E. U. (2010). Selective manipulation of ICT and PET processes in styryl-bodipy derivatives: Applications in molecular logic and fluorescence sensing of metal ions. *Journal of American Chemical Society*, 132(23), 8029–8036.
- Chandrasekhar, V., Bag, P., Pandey, M. D. (2009). Phosphorus-supported multidentate coumarin-containing fluorescence sensors for Cu^{2+} . *Tetrahedron*, 65, 9876–9883.
- Chen, Z. J., Tian, Z., Kallio, K., Oleson, A. L., Ji, A., Borchardt, D., Jiang, D., Remington, S. J., Ai, H. W. (2016). The N-B interaction through a water bridge: Understanding the chemoselectivity of a fluorescent protein based probe for peroxynitrite. *Journal of American Chemical Society*, 138, 4900–4907.
- Cheng, D., Zhao, W., Yang, H., Huang, Z., Liu, X., Han, A. (2016). Detection of Hg^{2+} by a FRET ratiometric fluorescent probe based on a novel BODIPY-RhB system. *Tetrahedron Letters*, 57, 2655–2659.
- Cherreddy, N. R., Raju, M. V. N., Reddy, B. M., Krishnaswamy, V. R., Korrapati, P. S., Reddy, B. J. M., Rao, V. J. (2016). A TBET based BODIPY-rhodamine dyad for the ratiometric detection of trivalent metal ions and its application in live cell imaging. *Sensors and Actuators B*, 237, 605–612.
- Coskun, A., Akkaya, E.U. (2005). Ion sensing coupled to resonance energy transfer: a highly selective and sensitive ratiometric fluorescent chemosensor for Ag(I) by a modular approach. *Journal of American Chemical Society*, 127, 10464–10465.
- Czarnik, A. W. (1994). Chemical communication in water using fluorescent chemosensors. *Accounts of Chemical Research*, 27, 302–308.
- Czarnik, A. W. (1993). *Fluorescent Chemosensors for Ion and Molecule Recognition*, American Chemical Society, Washington, DC.

- Çetindere, S., Tümay, S. O., Kılıç, A., Durmuş, M., Yeşilot, S. (2016). Hexa-BODIPY linked-triazole based on a cyclotriphosphazene core as a highly selective and sensitive fluorescent sensor for Fe^{2+} ions. *Journal of Fluorescence*, 26, 1173–1181.
- Daly, B., Ling, J., de Silva, A. P. (2015). Current developments in fluorescent PET (photoinduced electron transfer) sensors and switches. *Chemical Society Reviews*, 44, 4203–4211.
- de Silva, A. P., de Silva, S. A. (1986). Fluorescent signalling crown ethers; “switching on” of fluorescence by alkali metal ion recognition and binding in situ. *Journal of the Chemical Society, Chemical Communications*, 1709–1710.
- de Silva, A. P., Gunaratne, H. Q. N., Gunnlaugsson, T., Huxley, A. J. M., McCoy, C. P., Rademacher, J. T., Rice, T. E. (1997). Signaling recognition events with fluorescent sensors and switches. *Chemical Reviews*, 97, 1515–1566.
- Gao, J., Chen, X., Chen, S., Meng, H., Wang, Y., Li, C., Feng, L. (2019). The BODIPY-based chemosensor for fluorometric/colorimetric dual channel detection of RDX and PA. *Analytical Chemistry*, 91, 13675–13680.
- Gryniewicz, G., Poenie, M., Tsien, R. Y. (1985). A New generation of Ca^{2+} indicators with greatly improved fluorescence properties. *Journal of Biological Chemistry*, 260, 3440–3450.
- Gul, A., Oguz, M., Kursunlu, A. N., Yilmaz, M. (2020). A novel colorimetric/fluorometric dual-channel sensor based on phenolphthalein and bodipy for Sn (II) and Al (III) ions in half-aqueous medium and its applications in bioimaging. *Dyes and Pigments*, 176, 108221.
- Haldar, U., Sharma, R., Ruidas, B., Lee, H. (2020). Toward rapid and selective detection of hypochlorous acid in pure aqueous media and its application to cell imaging: BODIPY-derived water-soluble macromolecular chemosensor with high sensitivity. *Dyes and Pigments*, 172, 107858.
- Haldar, U., Lee, H. (2019). BODIPY-derived polymeric chemosensor appended with thiosemicarbazone units for the simultaneous detection and separation of Hg(II) ions in pure aqueous media. *ACS Applied Materials & Interfaces*, 11, 13685–13693.

- Herten, D.-P., Haderspeck, A., Braun, F., Wadepohl, H. (2018). Copper (II)-induced fluorescence quenching of a bodipy fluorophore. *Zeitschrift für anorganische und allgemeine Chemie*, 644, 735–739.
- Hiruta, Y., Koiso, H., Ozawa, H., Sato, H., Hamada, K., Yabushita, S., Citterio, D., Suzuki, K. (2015). Near IR emitting red-shifting ratiometric fluorophores based on borondipyrromethene. *Organic Letters*, 17, 3022–3025.
- Huang, Y., Li, C.-F., Shi, W.-J., Tan, H.-Y., He, Z.-Z., Zheng, L., Liu, F., Yan, J.-W. (2019). A near-infrared BODIPY-based fluorescent probe for ratiometric and discriminative detection of Hg^{2+} and Cu^{2+} ions in living cells. *Talanta*, 198, 390–397.
- Huston, M. E., Haider, K. W., Czarnik, A. W. (1988). Chelation enhanced fluorescence in 9,10-bis[[2-(dimethylamino)ethyl]-methylamino]methyl anthracene. *Journal of the American Chemical Society*, 110, 4460–4462.
- Isaad, J., El-Achari, A. (2020). BODIPY-modified silica-coated magnetite nanoparticles/Copper (II) complex as fluorescent chemosensor for cyanide anions detection in aqueous medium. *International Journal of Environmental Analytical Chemistry*, 1-16.
- Jeong, Y., Yoo, J. (2012). Recent progress on fluorescent chemosensors for metals. *Inorganica Chimica Acta*, 381, 2–14.
- Ji, J., Chereddy, S. S., Ren, Y., Chen, X., Su, D., Zhong, Z., Mori, T., Inoue, Y., Wu, W., Yang, C. (2018). A BODIPY-based near infrared fluorescent probe for Fe^{3+} in water. *Journal of Photochemistry and Photobiology A: Chemistry*, 355, 78–83.
- Kaur, N., Kumar, S. (2011). Colorimetric metal ion sensors. *Tetrahedron* 67, 9233–9254.
- Kim, H. N., Ren, W. X., Kim, J. S., Yoon, J. (2012). Fluorescent and colorimetric sensors for detection of lead, cadmium, and mercury ions. *Chemical Society Reviews*, 41, 3210–3244.
- Konopelski, J. P., Kotzyba-Hibert, F., Lehn, J. M., Desvergne, J. P., Fagès, F., Castellan, A., Bouas-Laurent, H. (1985). synthesis, cation binding, and

- photophysical properties of macrobicyclic anthraceno-cryptands. *Journal of the Chemical Society, Chemical Communications*, 433–436.
- Kursunlu, A. N. (2015). A fluorescent “turn on” chemosensor based-on bodipy-anthraquinone for Al(III) ion: Synthesis and complexation-spectroscopic studies. *RSC Advances*, 5, 41025-41032.
- Kursunlu, A. N., Ozmen, M., Güler, E. (2019). A novel fluorescent chemosensor for Cu(II) ion: click synthesis of dual-bodipy including the triazole groups and bioimaging of yeast cells. *Journal of Fluorescence*, 29:1321–1329.
- Loudet, A., Burgess, K. (2007). BODIPY dyes and their derivatives: Syntheses and spectroscopic properties. *Chemical Reviews*, 107, 4891-4932.
- Li, X., Gao, X., Shi W., Ma, H. (2014). Design strategies for water-soluble small molecular chromogenic and fluorogenic probes. *Chemical Reviews*, 114, 590–659.
- Li, X., Han, Y., Sun, S., Shana, D., Ma, X., He, G., Merguc, N., Park, J. S., Kim, C. H., Son, Y. A. (2020). A diaminomaleonitrile-appended BODIPY chemosensor for the selective detection of Cu²⁺ via oxidative cyclization and imaging in SiHa cells and zebrafish. *Spectrochimica Acta Part A: Molecular and Biomolecular Spectroscopy*, 233, 118179.
- Li, S., Cao, D., Hu, Z., Li, Z., Meng, X., Han, X., Ma, W. (2019). A chemosensor with a paddle structure based on a BODIPY chromophore for sequential recognition of Cu²⁺ and HSO₃⁻. *RSC Advances*, 9, 34652–34657.
- Maity, A., Ghosh, U., Giri, D., Mukherjee, D., Maiti, T. K., Patra, S. K. (2019). A Water-soluble BODIPY based 'OFF/ON' fluorescence probe for the detection of Cd²⁺ ions with high selectivity and sensitivity. *Dalton Transactions*, 48, 2108-2117.
- Özcan, E., Coşut, B. (2018). Fluorescent sensing of cesium ions by an amide-linked bodipy dye: Synthesis and photophysical properties. *ChemistrySelect*, 3, 7940-7944.
- Quang, D. T., Kim, J. S. (2010). Fluoro- and chromogenic chemodosimeters for heavy metal ion detection in solution and biospecimens. *Chemical Reviews*, 110, 6280–6301.

- Rani, P. (2015). Chemosensor and its applications. *International Refereed Journal of Reviews and Research*, 3 (5), 1-10.
- Sahoo, S. K., Kim, G. D., Choi, H. J. (2016). Optical sensing of anions using C_{3v} -symmetrictripodal receptors. *Journal of Photochemistry and Photobiology C: Photochemistry Reviews*, 27, 30–53.
- Saura, A. V., Burguete, M. I., Galindo, F., Luis, S. V. (2017). Novel fluorescent anthracene–bodipy dyads displaying sensitivity to pH and turn-on behaviour towards Cu(II) ions. *Organic and Biomolecular Chemistry*, 15, 3013.
- Shen, B., Qian, Y. (2018). Building Rhodamine-BODIPY fluorescent platform using Click reaction: Naked-eye visible and multi-channel chemodosimeter for detection of Fe^{3+} and Hg^{2+} . *Sensors and Actuators B*, 260, 666–675.
- Sousa, L. R., Larson, J. M. (1977). Crown ether model systems for the study of photoexcited state response to geometrically oriented perturbors. The effect of alkali metal ions on emission from naphthalene derivatives. *Journal of the American Chemical Society*, 99, 307–310.
- Sui, B., Liu, X., Wang, M., Belfield, K. D. (2016). A highly selective fluorescence turn-on sensor for extracellular calcium ion detection. *Chemical European Journal*, 22, 10351-10354.
- Sun, R., Wang, L., Jiang, C., Du, Z., Chen, S., Wu, W. (2020). A highly efficient bodipy based turn-off fluorescent probe for detecting Cu^{2+} . *Journal of Fluorescence*, 30, 883-890.
- Şenkuytu, E., Eçik, E. T., Çoşut, B. (2018). Bodipy decorated triazine chemosensors for Ag^+ ions with high selectivity and sensitivity. *Journal of Luminescence*, 203, 639–645.
- Tang, F. K., Zhu, J., Kong, F. K-W., Ng, M., Bian, Q., Yam, V. W-W., Tse, A. K-W., Tse, Y-C., Leung, K. C-F. (2020). A BODIPY-based fluorescent sensor for the detection of Pt^{2+} and Pt drugs. *Chemical. Communications*, 56, 2695-2698.
- Treibs, A., Kreuzer, F. H. (1968). Difluoroboryl-komplexe von di- und tripyrrylmethenen. *Justus Liebigs Annalen der Chemie*, 718 (1), 208–223.

- Ulrich, G., Ziessel, R., Harriman, A. (2008). The chemistry of fluorescent bodipy dyes: Versatility unsurpassed. *Angewandte Chemie*, 47, 1184–1201.
- Wang, B. S., Li, P., Yu, F., Song, P., Sun, X., Yang, S., Lou, Z., Han, K. (2013). A reversible fluorescence probe based on Se-BODIPY for the redox cycle between HClO oxidative stress and H₂S repair in living cells. *Chemical Communications*, 49, 1014–1016.
- Wang, J. M., Yu, H., Li, Q., Shao, S. J. (2015). A BODIPY-based turn-on fluorescent probe for the selective detection of hydrogen sulfide in solution and in cells. *Talanta*, 144, 763–768.
- Wang, Y., Zhu, M., Jiang, E., Hua, R., Na, R., Li, Q. X. (2017). A simple and rapid turn on ESIPT fluorescent probe for colorimetric and ratiometric detection of biothiols in living cells. *Scientific Reports*, 7, 4377.
- Wu, D., Sedgwick, A. C., Gunnlaugsson, T., Akkaya, E. U., Yoon, J. James, T. D. (2017). Fluorescent chemosensors: the past, present and future. *Chemical Society Reviews*, 46, 7105–7123.
- Wu, Y.S., Li, C.Y., Li, Y.F., Tang, J.L., Liu, D. (2014). A ratiometric fluorescent chemosensor for Cr³⁺ based on monomer? excimer conversion of a pyrene compound. *Sensors and Actuators B: Chemical*, 203, 712–718.
- Xia, S., Shen, J., Wang, J., Wang, H., Fang, M., Zhou, H., Tanasova, M. (2018). Ratiometric fluorescent and colorimetric BODIPY-based sensor for zinc ions in solution and living cells. *Sensors and Actuators B*, 258, 1279–1286.
- Xiao, H., Li, J., Wu, K., Yin, G., Quan, Y., Wang, R. (2015). A turn-on BODIPY-based fluorescent probe for Hg(II) and its biological applications. *Sensors and Actuators B*, 213, 343–350.
- Xue, Z., Liu, T., Liu, H. (2019). Naked-eye chromogenic and fluorogenic chemosensor for mercury (II) ion based on substituted distyryl BODIPY complex. *Dyes and Pigments*, 165, 65–70.
- Yamada, K., Nomura, Y., Citterio, D., Iwasawa, N., Suzuki, K. (2005). Highly sodium-selective fluoroionophore based on conformational restriction of oligoethyleneglycol-bridged biaryl boron-dipyrromethene. *Journal of the American Chemical Society*, 2005, 127, 6956–6957.

- Yang, Y., Zhao, Q., Feng, W., Li, F. (2013). Luminescent chemodosimeters for bioimaging. *Chemical Reviews*, 113, 192–270.
- Yao, Y., Xiao, S., Dan, F. (2013). Boron-fluorine photosensitizers for photodynamic therapy. *Journal of Chemistry*. Article ID 697850, 1-10.
- Zhang, J. F., Zhou, Y., Yoon, J., Kim, J.S. (2011). Recent progress in fluorescent and colorimetric chemosensors for detection of precious metal ions (silver, gold and platinum ions). *Chemical Society Reviews*, 40, 3416–3429.
- Zhang, C., Han, Z., Wang, M., Yang, Z., He, W., Ran, X. (2018). A new bodipy-derived ratiometric sensor of internal charge transfer (ICT) Effect: colorimetric/fluorometric sensing for Ag⁺. *Dalton Transactions*, 2018, 47, 2285-2291.
- Zhu, H., Fan, J., Wang, B., Peng, X. (2015). Fluorescent, MRI, and colorimetric chemical sensors for the first-row d-block metal ions. *Chemical Society Reviews*, 44 (13), 4337-4366.

CHAPTER 4

**A REVIEW OF DNA BINDING ACTIVITIES
OF METAL(II) COMPLEXES CONTAINING
AROMATIC AMINO ACIDS AND INTERCALATING
LIGANDS**

Assist. Prof. Dr. Duygu İNCİ^{1*}
Prof. Dr. Rahmiye AYDIN

^{1*} Department of Chemistry, Faculty of Arts and Sciences, Kocaeli University,
41380 Kocaeli, Turkey, duygu.inci@kocaeli.edu.tr, ORCID: 0000-0002-0483-9642

INTRODUCTION

DNA, deoxyribonucleic acid, is the intermolecular information transport in our cells. It occurs of two polymer strands. The polymer strands are formed of nucleotides with four different building blocks. These nucleotide forms of a phosphoric acid esterified with a deoxyribose sugar, which is covalently linked to different DNA bases: guanine (G), adenine (A), cytosine (C) or thymine (T) (Figure 1). DNA bases exhibit a hydrogen bonding pattern, ending up G pairing with C and A with T. Compared to the A-T base pair, the C-G base pair includes three hydrogen bonds, therefore base pair sequences rich in C-G are more stable than those rich in A-T. In addition, at physiological pH, the phosphate backbone of DNA has a negative charge. The DNA structure shows a large groove and a small groove. The small groove is narrow and shallow while the main groove is deep and wide.

There are various types of interactions with which compounds bind to DNA. The DNA interactions with compounds can be classified as covalent and non-covalent, where non-covalent interactions could also be subdivided into electrostatic, intercalation, minor and major groove binding

(Tse and Boger, 2004). The type of interactions between compounds and DNA is a significant tool for the prediction of potential physiological results of such interactions.

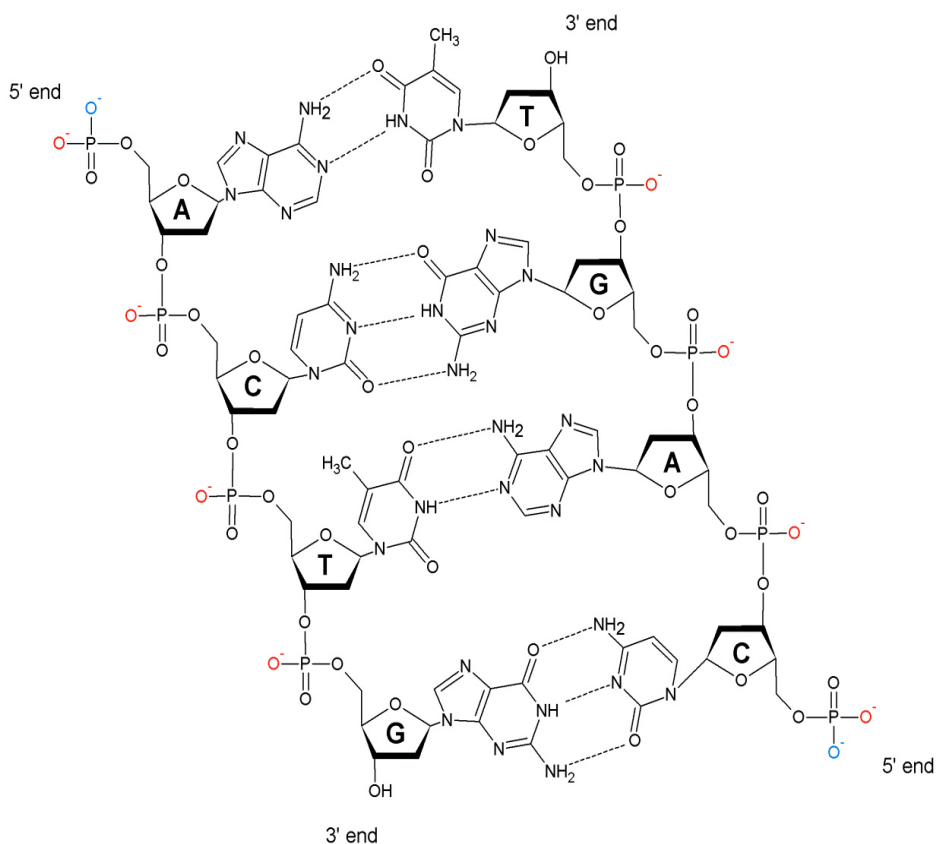


Figure 1: DNA Structure of Nucleotides Connected by 5' to 3' Phosphodiester Bonds

1. COVALENT BINDING

The covalent bonding is a type of DNA interaction that is irreversible and prevents cell replication. Figure 2 shows the structure of cisplatin and the binding of the cisplatin to the DNA.

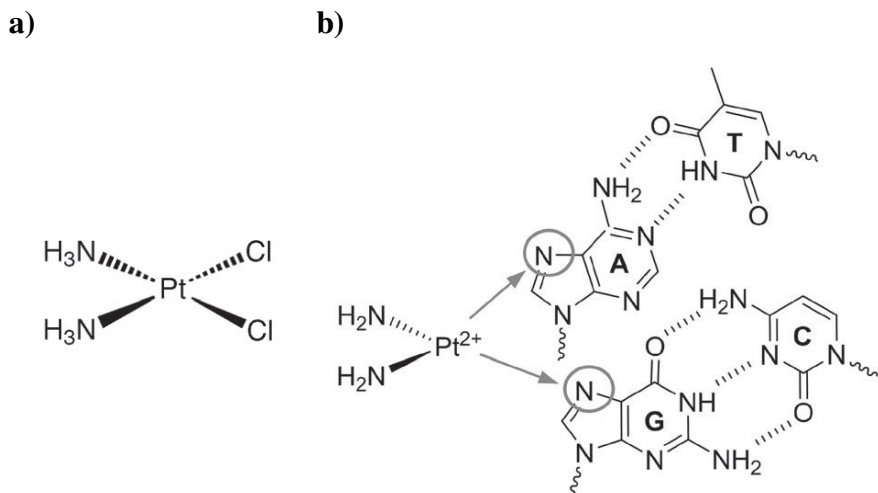


Figure 2: a) Cisplatin b) Cisplatin Irreversible Binding (covalent) with DNA (Gill and Thomas, 2012).

2. NON-COVALENT BINDING

2.1. Electrostatic Interactions

Electrostatic interaction occurs when positively charged ions such as Na⁺, K⁺, Mg²⁺ and cationic compounds interact with the sugar-phosphate DNA backbone. These interactions neutralize the phosphate charges and give rise to the release of concentrated counter ions (Strekowski and Wilson, 2007).

2.2. Groove Binding Interactions

DNA consists of two grooves called minor and major groove. Small molecules generally interact with the minor groove of DNA on the other hand proteins typically interact with the major groove of DNA. The interaction of netropsin, which is known to bind to the DNA

minor groove, has been proven by various crystallographic and NMR techniques (Figure 3). It has been reported that the interactions are mostly by hydrogen bonding and van der Waals forces. It is known that when a compound is binded to the minor groove, they cause only minor changes in the conformation of DNA and the natural shape of DNA remains the same (Pućkowska, Bielawski, Bielawska and Midura-Nowaczek, 2004).

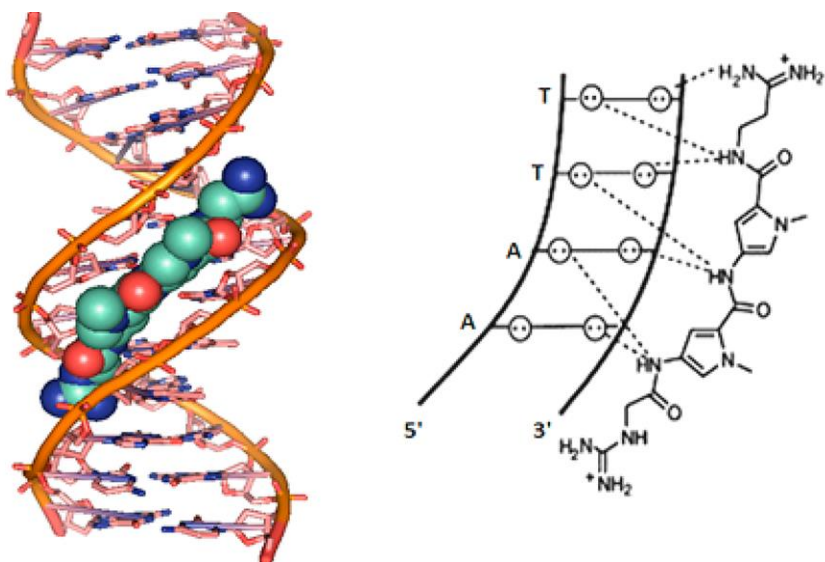


Figure 3: X-ray Crystal Structure of 1:1 Complex of Netropsin:DNA (Taberner, Verdaguer, Col, Fita, van der Marel, van Boom, Rich and Aymami, 1993)

Molecular docking is an important technique to figure out the interaction between DNA and compound. To discover the binding mode of the nickel (II) complex were performed to molecular docking studies with DNA. As illustrated in Figure 4, these results suggest that possible conformation of the nickel (II) complex is inside the DNA

major groove. Additionally, hydrogen bonding and van der Waals force also play a significant role in the interaction between DNA and the complex (Dong, Gao, Zhang, Xu, Wang, Kong and Li, 2020).

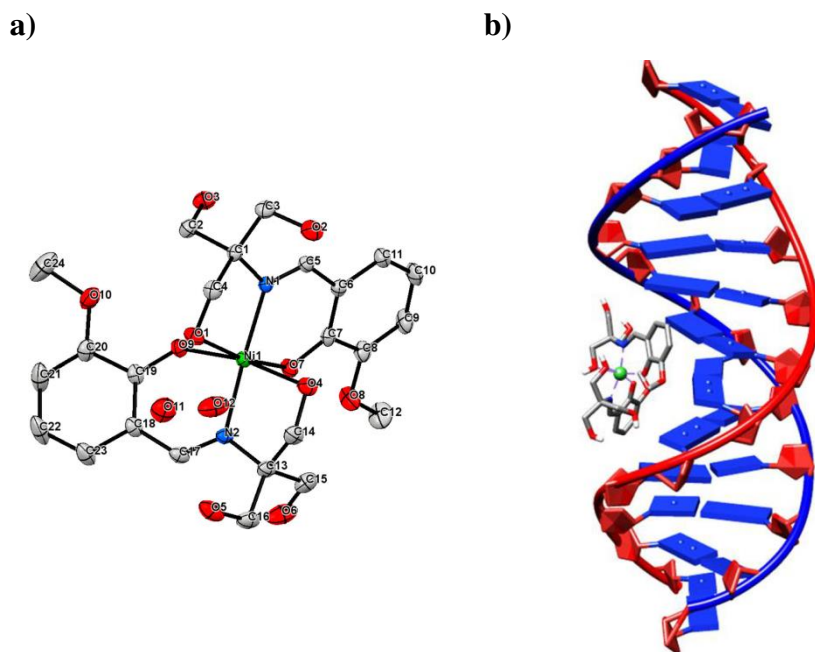


Figure 4. a) Crystal Structure of Nickel(II) Complex ($[\text{Ni}(\text{o-van-tris})_2] \cdot 2\text{H}_2\text{O}$) b) Molecular Docking of the Nickel(II) Complex at the Major Groove of DNA

2.3. Intercalation

The aromatic compounds interact with DNA by means of intercalation. Intercalation takes place when cationic planar compounds containing aromatic rings insert between the DNA base pairs (Lerman, 1961) (Figure 5).

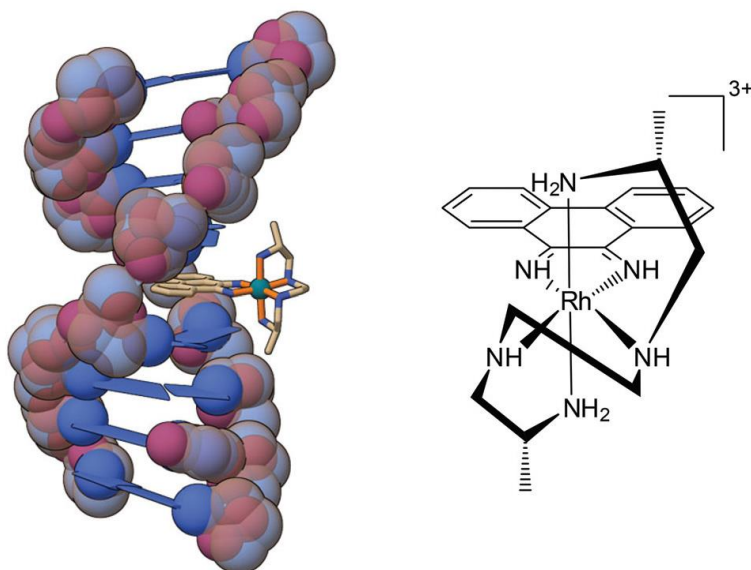


Figure 5: X-ray Data of the Sequence Selective Intercalation of $[\text{Rh}(\text{Me}_2\text{trien})(\phi)]^{3+}$ into the DNA (Kielkopf, Erkkila, Hudson, Barton and Rees, 2000)

3. TECHNIQUES FOR MEASURING DNA INTERACTIONS

Various methods are used to investigate metal complexes-DNA interactions. NMR and X-ray provide detailed information at the atomic level details of the host-guest binding (Andersen and Sletten, 2000). Mass spectrometry, MALDI (matrix assisted laser desorption ionization) and ESI (electrospray ionization) methods, allow the analysis of biomolecules (Beck, Colgrave, Ralph and Sheil, 2001). Assays with gel electrophoresis, different incubation protocols help verify DNA cleavage (Tan, Wang and Zhu, 2009). Fluorescence and electronic absorption spectroscopy are the most used techniques due to their repeatability, sensitivity and versatility. The fluorescence and absorbance spectra of metal complexes change their maxima after

interacting with DNA. Also, an increase in fluorescence or quenching can be observed as a result of the interaction of metal complexes with DNA (Busto, Garcia, Leal, Gaspar, Martins, Boggioni and Secco, 2011).

4. DNA BINDING ACTIVITIES OF METAL(II) COMPLEXES CONTAINING AROMATIC AMINO ACIDS AND INTERCALATING LIGANDS

Electronic absorption spectroscopy is common a technique used to study the interactions of metal complexes with DNA. After metal complexes interact with DNA base pairs, an interaction occurs between the π^* orbitals of the ligands that form metal complexes and the π orbitals of the nucleic acid base pairs in the DNA structure. This interaction causes changes in the absorbance and wavelength of systems containing metal complex+DNA solutions. With the interaction between the π^* orbitals of the ligands that metal complexes and the π orbitals of the nucleic acid base pairs in the DNA structure, the π - π^* transition energy decreases and a red shift in wavelength (bathochromic effect) is observed (Sharma, Toupet, Ahmad and Arjmand, 2016). A decrease in absorbance intensity is observed simultaneously with the red shift observed in the wavelength (hypochromic effect). In solution systems containing metal complex+DNA, the decrease in the absorbance intensity of the metal complex and the red shift in the wavelength generally indicate that metal complexes interact with DNA by intercalation. In the solution systems containing metal complex + DNA, the increase in the

absorbance intensity of the metal complex (hyperchromic effect) and the blue shift in the wavelength (hypsochromic effect) generally indicate that metal complexes interact with DNA electrostatically or as minor / major groove binding in the DNA structure (Rao, Patra and Chetana, 2007). K_b , intrinsic binding constant, is an important parameter for measuring the interaction affinity between metal complexes and DNA (Hadjiliadis and Sletten, 2009). Current methods for determining K_b are: McGhee and von Hippel (McGhee and von Hippel, 1974), Scatchard (Scatchard, 1949), Wolfe et al. (Wolfe, Shimer and Meehan, 1987), Rodger and Norden (Rodger and Norden, 1997), Norden and Tjerneld (Norden and Tjerneld, 1976), Carter et al. (Carter, Rodriguez and Bard, 1989).

In order to verify the type of binding of metal complexes to DNA by fluorescence spectroscopy studies and to compare the binding forces of metal complexes to DNA with the results obtained using electronic absorption spectroscopy, displacement studies are carried out using EB, which is known to interact to DNA via intercalation. In the solution system containing EB+DNA, there is usually an increase in the fluorescence of the EB+DNA solution when EB binds to DNA. When another molecule is added to the EB+DNA solution, it is thought that the newly added molecule with EB is replaced by a reduce in the fluorescence of the EB+CT-DNA+molecule system (Dhara, Roy, Ratha, Manassero and Banerjee, 2007). From the spectra obtained from fluorescence spectroscopy studies, the values of K_{sv} (Stern-Volmer constant, which indicates the fluorescence quenching

capabilities of the compounds) and K_{app} (the apparent DNA binding constant where the complexes reduce the fluorescence intensity of the EB+DNA solution to 50 %) constants are calculated (Lakowicz and Weber, 1973).

Complexes involving intercalating ligands (1,10-phenanthroline and derivatives) and various metal ions are known for their ability to interact with DNA. As in the case of most intercalating ligands, the type of interaction depending on the DNA form as well as the structural properties of the complexes. In fact, complexes containing intercalating ligands could interact with DNA in an intercalative mode. Furthermore, metal complexes containing intercalating ligands can also interact with DNA by simply inserting them into the minor or major Groove (Zeglis, Pierre and Barton, 2007). Amino acids are significant molecules involved in many biologically important processes. Amino acids could be chelating agents by means of amine ($-NH_2$) and carboxylate (COO^-) groups. Aromatic amino acids have many important properties. The aromatic amino acids are tyrosine, phenylalanine and tryptophan. Whereas tryptophan is aromatic because of its indole ring, while phenylalanine contains a phenyl group, tyrosine contains a hydroxy phenyl group. Both tyrosine and tryptophan could contribute to hydrogen bond formation.

The results of electronic absorption and fluorescence spectroscopy titrations provide an effective DNA binding ability to these complexes (Tables 1-4). The observed tendency of the K_b , K_{sv} and K_{app} values indicates planarity of the metal(II) complexes, seems to increase the

DNA intercalation ability. The binding between the complexes in the polymeric structure and DNA is by means of electrostatic binding. If hypochromicity is observed with bathochromic shift, it indicates the nature of the complexes binding a groove to CT-DNA (Tables 1-4).

Table 1: The Binding Constants, K_b , for the Interaction of Ternary Metal(II) Complexes Containing Intercalating Ligands and Tyrosine with CT-DNA

Compounds	Electronic absorption spectroscopy				
	K_b	$\log K_b$	Hypo %*	Binding mode	Ref
[Cu(phen)(L-tyr)BPEI]ClO ₄	2.10x10 ⁴	4.32	-	Electrostatic	Lakshmipraba et al, 2015
[Cu(Fc-try)(aip)]ClO ₄	6.80x10 ⁵	5.83	-	Intercalation	Goswami et al, 2014
[Cu(Fc-tyr)(pyip)]ClO ₄	6.30x10 ⁶	6.80	-	Intercalation	Goswami et al, 2014
[Cu(Fc-Tyr)(phen)]ClO ₄	7.60x10 ⁴	4.88	-	Groove binding	Goswami et al, 2013
[Cu(Fc-Tyr)(dpq)]ClO ₄	2.30x10 ⁵	5.36	-	Groove binding	Goswami et al, 2013
[Cu(Fc-Tyr)(dppz)]ClO ₄	4.20x10 ⁵	5.62	-	Intercalation	Goswami et al, 2013
[Cu(Fc-Tyr)(nip)]ClO ₄	2.10x10 ⁵	5.32	-	Groove binding	Goswami et al, 2013
[(Cu-Phen-Tyr)(H ₂ O)]ClO ₄	2.44x10 ⁶	6.39	-	Intercalation	Yang et al, 2011
[Cu(saltyr)(phen)]	3.47x10 ⁴	4.54	20.0	Intercalation	Reddy and Shilpa, 2011
[Cu(L-tyr)(phen)]ClO ₄	4.00x10 ³	3.60	43.0	Intercalation	Ramakrishnan et al, 2009
[Cu(L-tyr)(5,6-dmp)]ClO ₄	6.50x10 ³	3.81	44.0	Intercalation /hydrophobic	Ramakrishnan et al, 2009
[Cu(L-tyr)(dpq)]ClO ₄	9.80x10 ³	3.99	49.0	Intercalation	Ramakrishnan et al, 2009
[Cu(phen)(L-Tyr)(H ₂ O)]	3.75x10 ³	3.57	-	Intercalation	Reddy and Manjula, 2009

[Cu(dmphen)(tyr)(H ₂ O)]NO ₃ ·H ₂ O	1.56x10 ⁵	5.19	52.1	Intercalation	İnci et al, 2015a
[Cu(nphen)(L-tyr)(H ₂ O)]NO ₃ ·2H ₂ O	1.05x10 ³	3.02	10.1	Intercalation	İnci et al, 2015b
[Cu(phen)(tyr)(H ₂ O)]NO ₃ ·2H ₂ O	1.89x10 ³	3.28	14.8	Intercalation	İnci et al, 2015b
[Cu ₂ (py-phen) ₂ (tyr) ₂ (H ₂ O) ₂](NO ₃) ₂ ·3H ₂ O	2.21x10 ³	3.34	-	Intercalation	İnci et al, 2018
[Cu(4-mphen)(tyr)(H ₂ O)]ClO ₄	9.65x10 ³	3.98	10.2	Intercalation	İnci et al, 2019a
[Cu(5-mphen)(tyr)(H ₂ O)]ClO ₄ ·1.5H ₂ O	5.05x10 ³	3.70	10.9	Intercalation	İnci et al, 2019a
[Cu(tmphen)(tyr)(NO ₃)]0.5H ₂ O	2.33x10 ⁵	5.37	30.2	Intercalation	İnci et al, 2019a
[Pd(phen)(tyr)]NO ₃ ·H ₂ O	7.33x10 ²	2.82	-	Intercalation	İnci et al, 2019b
[Pd(5-mphen)(tyr)]NO ₃	6.66x10 ²	3.30	-	Intercalation	İnci et al, 2019b

*Hypo: Hypochromism ($\text{Hypo \%} = A - A_0/A_0$); BPEI: branched polyethyleneimine (Lakshmipraba et al, 2015); Fc-tyr: ferrocenylmethyl-L-tyrosine, aip: 2-(9-anthryl)-1H-imidazo[4,5-f][1,10] phenanthroline, pyip: 2-(1-pyrenyl)-1H-imidazo[4,5-f][1,10]phenanthroline (Goswami et al, 2014); Fc-TyrH:ferrocene(Fc)-conjugated reduced Schiff base of L-tyrosine, phen:1,10-phenanthroline, dpq:dipyrido[3,2-d:2',3'f]quinoxaline, dppz: dipyrido[3,2-a:2',3'-c]phenazine, nip:2-(naphthalen-1-yl)-1H-imidazo[4,5-f][1,10]phenanthroline (Goswami et al, 2013); saltyr: salicylidene tyrosine (Reddy and Shilpa, 2011); 5,6-dmp:5,6-dimethyl-1,10-phenanthroline (Ramakrishnan et al, 2009); dmphen:4,7-dimethyl-1,10-phenanthroline (İnci et al, 2015a); nphen:5-nitro-1,10-phenanthroline (İnci et al, 2015b); py-phen:pyrazino[2,3-f][1,10]phenanthroline (İnci et al, 2018); 4-mphen: 4-methyl-1,10-phenanthroline, 5-mphen: 5-methyl-1,10-phenanthroline, tmphen: 3,4,7,8-tetramethyl-1,10-phenanthroline (İnci et al, 2019a).

Table 2: The Binding Constants, K_b , for the Interaction of Ternary Metal(II) Complexes Containing Intercalating Ligands and Phenylalanine with CT-DNA

Compounds	Electronic absorption spectroscopy				
	K_b	$\log K_b$	Hypo %*	Binding mode	Ref
[Ni(sal-L-phe)(phen)(CH ₃ OH)]CH ₃ OH	1.82x10 ⁴	4.26	-	Intercalation	Zhao et al, 2018
[Ni(naph-L-phe)(phen)(CH ₃ OH)]	1.96x10 ⁴	4.29	-	Intercalation	Zhao et al, 2018
[Ni(o-van-L-phe)(phen)(CH ₃ OH)]5CH ₃ OH	2.02x10 ⁴	4.31	-	Intercalation	Zhao et al, 2018
[Cu(PAIC)(phen)]2H ₂ O	2.60x10 ⁴	4.41	-	Intercalation	Annaraj et al, 2016
[Cu(phen)(L-phe)(BPEI)]ClO ₄ ·4H ₂ O	4.34x10 ⁵	5.64	-	Electrostatic, van der Waals, hydrogen bonding intercalation	Kumar and Arunachalam, 2009
[Cu(Fc-Phe)(phen)]ClO ₄	7.40x10 ⁴	4.87	-	Groove binding	Goswami et al, 2013
[Cu(Ph-Phe)(phen)(ClO ₄)]	5.00x10 ⁴	4.70	-	Groove binding	Goswami et al, 2013
[Cu(L-phe)(phen)(H ₂ O)]NO ₃	3.60x10 ⁵	5.56	-	Intercalation	Patra et al, 2008
[Cu(L-phe)(dpq)(H ₂ O)]NO ₃	6.10x10 ⁵	5.79	-	Intercalation	Patra et al, 2008
[Cu(L-phe)(dppz)(H ₂ O)]NO ₃	1.20x10 ⁶	6.08	-	Intercalation	Patra et al, 2008

Sal-L-phe: a Schiff base derived from salicylaldehyde and L-phenylalanine, naph-L-phe: a Schiff base derived from 2-hydroxy-1-naphthaldehyde and L-phenylalanine, o-van-L-phe: a Schiffbase derived from o-vanillin and L-phenylalanine (Zhao et al, 2018); PAIC = phenylalanine imidazole carboxylic acid (Annaraj et al, 2016); BPEI: branched polyethyleneimine (Kumar and Arunachalam, 2009); Fc-Phe: reduced Schiff base derived from L-phenylalanine and ferrocenecarboxaldehyde, Ph-Phe: reduced Schiff base of L-phenylalanine and benzaldehyde (Goswami et al, 2013).

Table 3: The Binding Constants, K_b , for the Interaction of Ternary Metal(II) Complexes Containing Intercalating Ligands and Tryptophan with CT-DNA

Compounds	<i>Electronic absorption spectroscopy</i>				
	K_b	$\log K_b$	Hypo %*	Binding mode	Ref
[Cu(Sal-Trp)(phen)]	2.40×10^5	5.38	-	Groove binding	Banaspatia et al, 2019
[Cu(Sal-Trp)(dpq)]	4.35×10^5	5.64	-	Groove binding	Banaspatia et al, 2019
[Cu(Sal-Trp)(dppz)]	6.38×10^5	5.80	-	Intercalation	Banaspatia et al, 2019
[Cu(Sal-Trp)(aip)]	5.30×10^5	5.72	-	Intercalation	Banaspatia et al, 2019
[Cu(<i>o</i> -vanillin-L-tryptophan)(phen)]	9.50×10^5	5.98	-	Intercalation	Theetharappan et al, 2017
[Cu(<i>o</i> -vanillin-L-tryptophan)(5,6-dmphen)]	7.70×10^5	5.89	-	Intercalation	Theetharappan et al, 2017
[Cu(Fc-Trp)(aip)]ClO ₄	7.50×10^5	5.88	-	Intercalation	Goswami et al, 2014
[Cu(Fc-Trp)(pyip)]ClO ₄	7.70×10^6	6.89	-	Intercalation	Goswami et al, 2014
[Cu(Trp Schiff base)(phen) ₂]Cl	3.90×10^5	5.59	31	Intercalation	Raman et al, 2012
[Ni(Trp Schiff base)(phen) ₂]Cl	1.70×10^5	5.23	28	Intercalation	Raman et al, 2012
[Co(Trp Schiff base)(phen) ₂]Cl	2.20×10^5	5.34	29	Intercalation	Raman et al, 2012
[Zn(Trp Schiff base)(phen) ₂]Cl	1.30×10^5	5.11	24	Intercalation	Raman et al, 2012
[VO(Naph-trp)(phen)]CH ₃ OH	6.80×10^4	4.83	-	Intercalation	Bian et al, 2012
[VO(<i>o</i> -Van-trp)(phen)]CH ₃ OH·H ₂ O	4.00×10^4	4.60	-	Intercalation	Bian et al, 2012
[Cu(Fc-Trp)(phen)]ClO ₄	1.89×10^5	5.28	-	Groove binding	Goswami et al, 2011
[Cu(Fc-Trp)(dpq)]ClO ₄	1.09×10^6	6.04	-	Groove binding	Goswami et al, 2011
[Cu(Fc-Trp)(dppz)]ClO ₄	1.67×10^6	6.22	-	Intercalation	Goswami et al, 2011

[Cu(Ph-Trp)(phen)(H ₂ O)]ClO ₄	2.05x10 ⁵	5.31	-	Groove binding	Goswami et al, 2011
[Cu(Ph-Trp)(dppz)(H ₂ O)]ClO ₄	1.28x10 ⁶	6.11	-	Intercalation	Goswami et al, 2011
[Zn(Fc-Trp)(dppz)]ClO ₄	1.61x10 ⁶	6.21	-	Intercalation	Goswami et al, 2011
{[Cu(phen)(trp)]ClO ₄ ·3H ₂ O} _n	8.24x10 ²	2.92	-	Intercalation	Şenel et al, 2019
{[Cu(4-mphen)(trp)]ClO ₄ ·3H ₂ O} _n	1.77x10 ³	3.25	-	Intercalation	Şenel et al, 2019
[[Cu(dmphen)(trp)(MeOH)] [Cu(dmphen)(trp)(NO ₃)]][NO ₃	5.52x10 ³	3.84	-	Intercalation	Şenel et al, 2019
[Cu(L-trp)(phen)(H ₂ O)]NO ₃	2.20x10 ⁴	4.34	-	Intercalation	Patra et al, 2008
[Cu(L-trp)(dpq)(H ₂ O)]NO ₃	4.30x10 ⁵	5.63	-	Intercalation	Patra et al, 2008
[Cu(L-trp)(dppz)(H ₂ O)]NO ₃	7.30x10 ⁵	5.86	-	Intercalation	Patra et al, 2008
[Cu(py-phen)(trp)(H ₂ O)]NO ₃	4.03x10 ³	3.61	-	Intercalation	İnci et al, 2020

Sal-TrpH: *N*-salicylyl-L-Tryptophan, aip: 2-(anthracen-1-yl)-1H-imidazo[4,5-f][1,10]phenanthroline (Banaspata et al, 2019); *o*-vanillin-L-tryptophan: (E)-2-(2-hydroxy-3-methoxybenzylideneamino)-3-(1H-indol-3-yl)propanoic acid, 5,6-dmphen: 5,6-dimethyl-1,10-phenanthroline (Theetharappan et al, 2017); Fc-Trp: ferrocenylmethyl-L-tryptophan, aip: 2-(9-anthryl)-1H-imidazo[4,5-f][1,10]phenanthroline, pyip: 2-(1-pyrenyl)-1H-imidazo[4,5-f][1,10]phenanthroline (Goswami et al, 2014); Naph-Trp: Schiff base derived from 2-hydroxy-1-naphthaldehyde, *o*-Van-trp: Schiff base derived from *o*-vanillin and L-tryptophan (Bian et al, 2012); Fc-Trp: ferrocene-appended reduced Schiff base of L-tryptophan, Ph-TrpH: reduced Schiff base derived from benzaldehyde and L-tryptophan (Goswami et al, 2011)

Table 4: Comparison of the K_{sv} and K_{app} Values for the Quenching of Fluorescence Intensity by Displacement of EB from CT-DNA by Ternary Metal(II) Complexes Containing Intercalating Ligands and Tyrosine/Phenylalanine/Tryptophan

Compounds	<i>Ethidium bromide (EB)</i>					Ref
	K_{sv}	$\log K_{sv}$	K_{app}	$\log K_{app}$	Binding mode	
[Cu(phen)(L-tyr)BPEI]ClO ₄	2.13x10 ⁴	4.33	-	-	Electrostatic	Lakshmipraba et al, 2015
[(Cu-Phen-Tyr)(H ₂ O)]ClO ₄	1.56x10 ⁵	5.19	-	-	Intercalation	Yang et al, 2011
[Cu(dmphen)(tyr)(H ₂ O)] NO ₃ ·H ₂ O	1.08x10 ⁵	5.04	1.77x10 ⁴	4.20	Intercalation	İnci et al, 2015a
[Cu(nphen)(L-tyr)(H ₂ O)] NO ₃ ·2H ₂ O	1.64x10 ³	3.21	2.17x10 ⁴	4.34	Intercalation	İnci et al, 2015b
[Cu(phen)(tyr)(H ₂ O)] NO ₃ ·2H ₂ O	1.61x10 ⁴	4.21	2.06x10 ⁵	5.31	Intercalation	İnci et al, 2015b
[Cu ₂ (py-phen) ₂ (tyr) ₂ (H ₂ O) ₂] (NO ₃) ₂ ·3H ₂ O	3.02x10 ³	3.48	1.41x10 ⁵	5.15	Intercalation	İnci et al, 2018
[Cu(4-mphen)(tyr)(H ₂ O)] ClO ₄	1.21x10 ³	3.08	4.17x10 ⁴	4.62	Intercalation	İnci et al, 2019a
[Cu(5-mphen)(tyr)(H ₂ O)] ClO ₄ ·1.5H ₂ O	9.47x10 ²	2.96	3.13x10 ⁴	4.49	Intercalation	İnci et al, 2019a
[Cu(tmphen)(tyr)(NO ₃)] 0.5H ₂ O	1.69x10 ⁵	5.21	8.33x10 ⁶	6.92	Intercalation	İnci et al, 2019a
[Pd(phen)(tyr)]NO ₃ ·H ₂ O	4.47x10 ³	3.65	1.66x10 ⁵	5.22	Groove binding	İnci et al, 2019b
[Pd(5-mphen)(tyr)]NO ₃	4.37x10 ³	3.64	2.63x10 ⁵	5.42	Groove binding	İnci et al, 2019b
[Cu(PAIC)(phen)]2H ₂ O	2.90x10 ⁴	4.46	3.50x10 ⁴	4.54	Intercalation	Annaraj et al, 2016
[Cu(L-phe)(phen)(H ₂ O)] NO ₃	-	-	1.08x10 ⁶	6.03	Intercalation	Patra et al, 2008
[Cu(L-phe)(dpq)(H ₂ O)]NO ₃	-	-	5.60x10 ⁶	6.75	Intercalation	Patra et al, 2008
[Cu(L-phe)(dppz)(H ₂ O)] NO ₃	-	-	9.33x10 ⁶	6.97	Intercalation	Patra et al, 2008
[Cu(<i>o</i> -vanillin-L-tryptophan)(phen)]	2.16x10 ⁴	4.33	8.00x10 ⁵	5.90	Intercalation	Theetharappa n et al, 2017

[Cu(<i>o</i> -vanillin-L-tryptophan)(5,6-dmphen)]	2.12x10 ⁴	4.33	7.00x10 ⁵	5.85	Intercalation	Theetharappan et al, 2017
{[Cu(phen)(trp)]ClO ₄ ·3H ₂ O} _n	1.51x10 ³	3.16	5.88x10 ⁴	4.77	Intercalation	Şenel et al, 2019
{[Cu(4-mphen)(trp)]ClO ₄ ·3H ₂ O} _n	3.79x10 ³	3.56	1.67x10 ⁵	5.22	Intercalation	Şenel et al, 2019
[[Cu(dmphen)(trp)(MeOH)] [Cu(dmphen)(trp)(NO ₃)]] NO ₃	1.23x10 ⁴	4.06	1.00x10 ⁶	6.00	Intercalation	Şenel et al, 2019
[Cu(L-trp)(phen)(H ₂ O)]NO ₃	-	-	2.42x10 ⁵	5.38	Intercalation	Patra et al, 2008
[Cu(L-trp)(dpq)(H ₂ O)]NO ₃	-	-	2.81x10 ⁶	6.45	Intercalation	Patra et al, 2008
[Cu(L-trp)(dppz)(H ₂ O)]NO ₃	-	-	4.66x10 ⁶	6.67	Intercalation	Patra et al, 2008
[Cu(py-phen)(trp)(H ₂ O)] NO ₃	6.19x10 ³	4.79	5.88x10 ⁵	5.77	Intercalation	İnci et al, 2020

BPEI: branched polyethyleneimine (Lakshmipraba et al, 2015); dmphen: 4,7-dimethyl-1,10-phenanthroline (İnci et al, 2015a); nphen: 5-nitro-1,10-phenanthroline (İnci et al, 2015b); py-phen: pyrazino[2,3-*f*][1,10]phenanthroline (İnci et al, 2018); 4-mphen: 4-methyl-1,10-phenanthroline, 5-mphen: 5-methyl-1,10-phenanthroline, tmphen: 3,4,7,8-tetra methyl-1,10-phenanthroline (İnci et al, 2019a), PAIC: phenylalanine imidazole carboxylic acid (Annaraj et al, 2016); *o*-vanillin-L-tryptophan: (E)-2-(2-hydroxy3methoxybenzylideneamino)3(1H-indol3yl)propanoicacid, 5,6-dmphen: 5,6-dimethyl-1,10-phenanthroline (Theetharappan et al, 2017)

CONCLUSIONS

In this study we have reviewed DNA binding activities of metal(II) complexes containing aromatic amino acids and intercalating ligands. The development of new cell-selective therapeutic agents offers possibilities for novel design of metal complexes. The structural characterization of the interaction between complexes and DNA is important and provides insight into what changes could be made to increase affinity and specificity for DNA. Structure-function relationships could also provide a significant information. It is clear that combinations of DNA interaction modes can be used to improve the binding affinity and selectivity of metal complexes, but there are many more examples. What is clear is that the inherent physicochemical diversity of transition metals and the design flexibility provided by the virtually unlimited range of ligands for coordination makes metal complexes powerful biologically active agents that could be used to investigate the structural diversity of DNA.

REFERENCES

- Andersen, B., Sletten, E. (2000). NMR studies on metal complexes of DNA oligomers. *Journal of Inorganic Biochemistry*, 79(1-4), 353-358.
- Annaraj, B., Balakrishnan, C., Neelakantan, M. A. (2016). Synthesis, structure information, DNA/BSA binding affinity and in vitro cytotoxic studies of mixed ligand copper(II) complexes containing a phenylalanine derivative and diimine co-ligands. *Journal of Photochemistry & Photobiology, B: Biology*, 160, 278-291.
- Banaspatia, A., Dasa, D., Choudhury, C. J., Bhattacharyya, A., Goswami, T. K. (2019). Photocytotoxic copper(II) complexes of *N*-salicylyl-L-tryptophan and phenanthroline bases. *Journal of Inorganic Biochemistry*, 191, 60-68.
- Beck, J. L., Colgrave, M. L., Ralph, S. F., Sheil, M. M. (2001). Electrospray ionization mass spectrometry of oligonucleotide complexes with drugs, metals, and proteins. *Mass Spectrometry Reviews*, 20(2), 61-87.
- Bian, L., Li, L., Zhang, Q., Dong, J., Xu, T., Li, J., Kong, J. (2012). Synthesis, crystal structures, DNA binding and cleavage studies of two oxovanadium(IV) complexes of 1,10-phenanthroline and Schiff bases derived from tryptophan. *Transition Metal Chemistry*, 37, 783-790.
- Busto, N., Garcia, B., Leal, J. M., Gaspar, J. F., Martins, C., Boggioni, A., Secco, F. (2011). ACMA (9-amino-6-chloro-2-methoxy acridine) forms three complexes in the presence of DNA. *Physical Chemistry Chemical Physics*, 43(13), 19534-19545.
- Carter, M. T., Rodriguez, M., Bard, A. J. (1989). Voltammetric studies of the interaction of metal chelates with DNA. 2. Tris-chelated complexes of cobalt(III) and iron(II) with 1,10-phenanthroline and 2,2'-bipyridine. *Journal of the American Chemical Society*, 111(24), 8901-8911.
- Dhara, K., Roy, P., Ratha, J., Manassero, M., Banerjee, P. (2007). Synthesis, crystal structure, magnetic property and DNA cleavage activity of a new terephthalate-bridged tetranuclear copper (II) complex. *Polyhedron*, 26, 4509-4517.

- Dong, J., Gao, L., Zhang, B., Xu, T., Wang, L., Kong, J., Li, L. (2020). Synthesis, crystal structure, Hirshfeld surface analysis, DNA binding, DNA cleavage activity and molecular docking of a new Schiff base nickel(II) complex. *Journal of Biomolecular Structure and Dynamics*, DOI: 10.1080/07391102.2020.1784789.
- Gill, M. R., Thomas, J. A. (2012). Ruthenium(II) polypyridyl complexes and DNA- from structural probes to cellular imaging and therapeutics, *Chemical Society Reviews*, Vol. 41, pp 3179–3192
- Goswami, T. K., Chakravarthi, B. V. S. K., Roy, M., Karande, A. A., Chakravarty, A. R. (2011). Ferrocene-Conjugated L-Tryptophan Copper(II) Complexes of Phenanthroline Bases Showing DNA Photocleavage Activity and Cytotoxicity. *Inorganic Chemistry*, 50, 8452–8464.
- Goswami, T. K., Gadadhar, S., Karande, A. A., Chakravarty, A. R. (2013). Photocytotoxic ferrocene-appended (L-tyrosine)copper(II) complexes of phenanthroline bases. *Polyhedron*, 52, 1287-1298.
- Goswami, T. K., Gadadhar, S., Balaji, B., Gole, B., Karande, A. A., Chakravarty, A. R. (2014). Ferrocenyl-L-amino acid copper(II) complexes showing remarkable photo-induced anticancer activity in visible light. *Dalton Transactions*, 43, 11988-11999.
- Hadjiliadis, N. D., Sletten, E. (2009). Metal Complexes-DNA Interactions. Wiley-Blackwell, Chichester.
- İnci, D., Aydin, R., Yılmaz, D., Gençkal, H. M., Vatan, O., Çinkılıç, N., Zorlu Y. (2015a). New water-soluble copper (II) complexes including 4,7-dimethyl-1,10-phenanthroline and Ltyrosine: synthesis, characterization, DNA interactions and cytotoxicities. *Spectrochimica Acta Part A: Molecular and Biomolecular Spectroscopy*, 136(Part B), 761-770.
- İnci, D., Aydin, R., Vatan, O., Yılmaz, D., Gençkal, H. M., Zorlu Y., Cavaş, T. (2015b). Binary and ternary new water soluble copper(II) complexes of L-Tyrosine and substitute 1,10-phenanthroline: Effect of substitution on DNA interactions and cytotoxicities. *Spectrochimica Acta Part A: Molecular and Biomolecular Spectroscopy*, 145, 313-324.

- İnci, D., Aydın, R., Huriyet, H., Zorlu, Y., Çinkılıç, N. (2018). Newly synthesized Cu(II) pyrazino[2,3-f][1,10]phenanthroline complexes as potential anticancer candidates. *Applied Organometallic Chemistry*, 32, e4309.
- İnci, D., Aydın, R., Huriyet, H., Vatan, Ö., Zorlu, Y., Çoşut, B., Çinkılıç, N. (2019a). *Applied Organometallic Chemistry*, 33(1), e4652.
- İnci, D., Aydın, R., Vatan, Ö., Şahin, O., Çinkılıç, N. (2019b). Water soluble binary and ternary palladium(II) complexes containing amino acids and intercalating ligands: Synthesis, characterization, biomolecular interactions and cytotoxicities. *New Journal of Chemistry*, 43(12), 4681-4697.
- İnci, D., Aydın, R., Vatan, Ö., Zorlu, Y. (2020). A potent drug candidature of Cu(II) pyrazino[2,3-f][1,10]phenanthroline complexes with bioactive ligands: Synthesis, crystal structures, biomolecular interactions, radical scavenging and cytotoxicities. *Journal of Biomolecular Structure and Dynamics*, DOI: 10.1080/07391102.2020.1808070
- Kielkopf, C. L. K., Erkkila, E., Hudson, B. P., Barton, J. K., Rees, D. C. (2000). Structure of a photoactive rhodium complex intercalated into DNA. *Nature Structural & Molecular Biology*, 7, 117-121.
- Kumar, R. S., Arunachalam, S. (2009). DNA binding and antimicrobial studies of polymer-copper(II) complexes containing 1,10-phenanthroline and L-phenylalanine ligands. *European Journal of Medicinal Chemistry*, 44, 1878-1883.
- Lakowicz, J.R., Weber, G. (1973). Quenching of fluorescence by oxygen. Probe for structural fluctuations in macromolecules. *Biochemistry*, 12, 4161-4170.
- Lakshmi praba, J., Arunachalam, S., Riyasdeen, A., Dhivya, R., Akbarsha, M. A. (2015). Polyethyleneimine anchored copper(II) complexes: Synthesis, characterization, in vitro DNA binding studies and cytotoxicity studies. *Journal of Photochemistry and Photobiology B: Biology*, 142, 59-67.
- Lerman, L. S. (1961). Structural considerations in the interaction of DNA and acridines. *Journal of Molecular Biology*, 3, 18-30.
- McGhee, J. D., von Hippel P. H. (1974). Theoretical aspects of DNA-protein

- interactions: co-operative and non-co-operative binding of large ligands to a one-dimensional homogeneous lattice. *Journal of Molecular Biology*, 86(2), 469-489.
- Norden, B., Tjernelund, F. (1976). High-sensitivity linear dichroism as a tool for equilibrium analysis in biochemistry. Stability constant of DNA-ethidiumbromide complex. *Biophysical Chemistry*, 4(2), 191-198.
- Patra, A. K., Bhowmick, T., Ramakumar, S., Nethajia, M., Chakravarty, A. R. (2008). DNA cleavage in red light promoted by copper(II) complexes of α -amino acids and photoactive phenanthroline bases. *Dalton Transactions*, 48, 6966-6976.
- Pućkowska, A., Bielawski, K., Bielawska, A., Midura-Nowaczek, K. (2004). Aromatic analogues of DNA minor groove binders-synthesis and biological evaluation. *European Journal of Medicinal Chemistry*, 39(1), 99-105.
- Ramakrishnan, S., Rajendiran, V., Palaniandavar, M., Periasamy, V. S., Srinag, B. S., Krishnamurthy, H., Akbarsha, M. A. (2009). Induction of Cell Death by Ternary Copper(II) Complexes of L-Tyrosine and Diimines: Role of Coligands on DNA Binding and Cleavage and Anticancer Activity. *Inorganic Chemistry*, 48, 1309-1322.
- Raman, N., Sobha, S., Selvaganapathy, M. (2012). Probing the DNA-binding behavior of tryptophan incorporating mixed-ligand complexes. *Monatshefte für Chemie-Chemical Monthly*, 143, 1487-1495.
- Rao, R., Patra, A. K., Chetana, P. R. (2007). DNA binding and oxidative cleavage activity of ternary (L-proline)copper(II) complexes of heterocyclic bases. *Polyhedron*, 26, 5331-5338.
- Reddy, P. R., Manjula, P. (2009). Synthesis, Characterization, and DNA-Binding Studies of Mononuclear Copper(II)-Phenanthroline-Tyrosine Complex. *Chemistry & Biodiversity*, 6, 71-78.
- Reddy, P. R., Shilpa, A. (2011). Oxidative and hydrolytic DNA cleavage by Cu(II) complexes of salicylidene tyrosine schiff base and 1,10 phenanthroline/bipyridine. *Polyhedron*, 30, 565-572.
- Rodger, A., Norden, B. (1997). Circular Dichroism and Linear Dichroism. Oxford

University Press, Oxford.

- Scatchard, G. (1949). The Attractions of Proteins for Small Molecules and Ions. *Annals of the New York Academy of Sciences*, 51(4), 660-672.
- Sharma, S., Toupet, L., Ahmad, M., Arjmand, F. (2016). Synthesis, characterization, and crystal structure of RNA targeted L- and D-phenylalanine-(1,10-phen)-copper(II) conjugate complexes: comparative in vitro RNA binding profile of enantiomers and their biological evaluation by morphological studies and antibacterial activity. *RSC Advance*, 6, 79372-79382.
- Strekowski, L., Wilson, B. (2007). Noncovalent interactions with DNA: an overview. *Mutation Research*, 623(1-2), 3-13.
- Şenel, P., İnci, D., Aydın, R., Huriyet, H., Zorlu, Y., Çinkılıç, N. (2019). Methyl substituent effect on one-dimensional copper(II) coordination polymers containing biologically active ligands: Synthesis, characterization, DNA interactions and cytotoxicities. *Applied Organometallic Chemistry*, 33(10), e5122.
- Tabernero, L., Verdaguer, N., Coll, M., Fita, I., van der Marel, G. A., van Boom, J. H., Rich, A., Aymami, J. (1993). Molecular structure of the A-tract DNA dodecamer d(CGCAAATTTGCG) complexed with the minor groove binding drug netropsin. *Biochemistry*, 32(33), 8403-8410.
- Tan, J., Wang, B., Zhu, L. (2009). DNA binding and oxidative DNA damage induced by a quercetin copper(II) complex: potential mechanism of its antitumor properties. *Journal of Biological Inorganic Chemistry*, 14(5), 727-739.
- Theetharappan, M., Subha, L., Balakrishnan, C., Neelakantan, M. A. (2017). Binding interactions of mixed ligand copper(II) amino acid Schiff base complexes with biological targets: Spectroscopic evaluation and molecular docking. *Applied Organometallic Chemistry*, 31, e3713.
- Tse, W. C., Boger, D. L. (2004). Sequence-selective DNA recognition: natural products and nature's lessons. *Chemical Biology*, 11(12), 1607-1617.
- Wolfe, A., Shimer, G. H., Meehan, T. (1987). Polycyclic aromatic hydrocarbons physically intercalate into duplex regions of denatured DNA. *Biochemistry*,

26(20), 6392-6396.

- Yang, Z., Wang, Y., Yang, G. (2011). Copper (II) complex of 1,10-phenanthroline and L-tyrosine with DNA oxidative cleavage activity in the gallic acid. *Biometals*, 24, 737-745.
- Zeglis, B. M., Pierre, V. C., Barton, J. K. (2007). Metallo-intercalators and metallo-insertors. *Chemical Communication*, 44, 4565-4579.
- Zhao, P., Zhai, S., Dong, J., Gao, L., Liu, X., Wang, L., Kong, J., Li, L. (2018). Synthesis, Structure, DNA Interaction, and SOD Activity of Three Nickel(II) Complexes Containing L-Phenylalanine Schiff Base and 1,10-Phenanthroline. *Bioinorganic Chemistry and Applications*, Article ID 8478152, 16.

CHAPTER 5

THE EFFECT OF SAMPLE AGE OF N-METHYL-BİS-TRİFLUOROACETAMİDE IN GALVINOXYL RADICAL ON DYNAMIC NUCLEAR POLARIZATION PARAMETERS

Assoc. Prof. Dr. Hüseyin OVALIOĞLU¹

¹ Bursa Uludag University, Faculty of Arts and Sciences, Physics Department, Bursa/Turkey. ovali@uludag.edu.tr ORCID NO: 0000-0002-7224-7526

INTRODUCTION

The first synthesis of Galvinoxyl or namely “Coppinger's” radical (as shown in Figure 1) was realized in 1957 by Galvin M. Coppinger (Coppinger, 1957). From that time many derivatives of Galvinoxyl radical have been synthesized and their characteristics have been reported (Lamp, Azarkh, Drescher, Imming, 2019; Gierke, Harrer, Kurreck, Reusch, 1973; Gierke, Harrer, Kurreck, Reusch, 1976; Harrer, Kurreck, Reusch, Gierke, 1975).

DNP (Dynamic Nuclear Polarization) is a class of methods developed to address the low-sensitivity problem concerning the calculation of NMR (Nuclear Magnetic Resonance). They depend on the transfer by MW (Microwave) of the high spin polarization of a PA (Polarizing Agent) to the coupled target nuclei (Ardenkjaer-Larsen et al., 2015). DNP at room temperature in liquids is also called Overhauser DNP (Overhauser, 1953; Hausser & Stehlik, 1968) is a spin relaxation process triggered by the time modulation of the hyperfine coupling between a target nuclear spin and unpaired electron via molecular motions. Furthermore, this technique facilitates the direct polarization of the target nuclei and thus has the potential to turn into a powerful method for NMR spectroscopy (Denysenkov & Prisner, 2019; Bennati & Orlando, 2019). DNP in liquids on ^1H nuclei was thoroughly explored in many magnetic fields during the last decade (Bennati, Tkach, Türke, 2011; Franck, Pavlova, Scott, Han, 2013; Griesinger et al., 2012; Bentum, Meerten, Sharma, Kentgens, 2016; Levien, Hiller, Tkach, Bennati, Orlando, 2020).

DNP in strong magnetic fields has been one of the main areas for studying magnetic resonance spectroscopy and imagery in recent years (Prisner, Denysenkov, Sezer, 2016).

1. MATERIALS AND EQUIPMENT

The technical details and equipment of the double resonance spectrometer used in this work have been extensively described in prior publications (Yalciner, 1978; Kirimli & Ovalioglu, 2014; Kirimli, Ovalioglu, Akay, 2017). Further information on the theory and applications of DNP for liquid samples is available in the literature (Kirimli & Ovalioglu, 2014; Kirimli et al., 2017; Hausser & Stehlik, 1968; Potenza, 1972; Müller-Warmuth, & Meise-Gresch, 1983). DNP experiments were performed at 1.53 mT with 61.2 kHz resonance frequency for the ¹⁹F nuclei and 45.5 MHz for the electrons. The sample was prepared at 3mM concentration.

Table 1: Basic constants and NMR sensitivity of MBFA (N-Methyl-bis-trifluoroacetamide)

Solvent	Purity ≥	Molecular Weight (g mol ⁻¹)	Boiling Point (°C)	Melting Point (°C)	Density (g cm ⁻³)	NMR Sensitivity (x10 ²² spin/cm ³)
N-Methyl- bis- trifluoroacet amide (MBFA) (C ₅ H ₃ F ₆ NO ₂)	% 97	223.08	122	< - 10	1.569	2.54

The solvent was bought from the US, Aldrich Chemical Co. The main properties of MBFA (N-Methyl-bis-trifluoroacetamide) in Figure 2 used as a solvent in this study are given in Table 1. The samples placed in 18-mm-diameter Pyrex tubes were degassed and sealed at about 10^{-3} Pa. Degassing is required, otherwise, the oxygen in the sample would not allow an EPR line to be quickly stimulated.

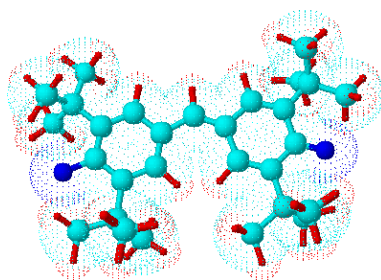


Figure 1: Open structure of the Galvinoxyl free radical ($C_{29}H_{41}O_2$). Turquoise shows carbon, blue oxygen, and red hydrogen.

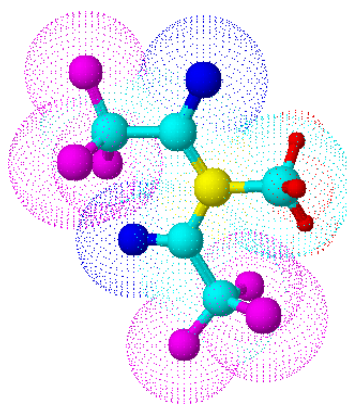


Figure 2: Open structure of the N-Methyl-bis-trifluoroacetamide molecule ($C_5H_3F_6NO_2$). Here, turquoise represents carbon, magenta fluorine, yellow nitrogen, red hydrogen, and navy blue represents oxygen.

2. RESULTS AND DISCUSSION

2.1. EPR Spectra

To calculate the DNP parameters in a certain magnetic field the EPR spectrum of free radical is necessary. ESR spectrum should not be affected by the solvents (Yalciner, 1978). Figure 3 puts forward the EPR spectrum of the Galvinoxyl/MBFA solvent medium based on four different temperatures and Table 2 shows Gaussian functions parameters of the Galvinoxyl/MBFA solvent medium for four different temperatures.

The spectrum was known as single Gaussian only, created by the overlap of a variety of Lorentzians. The experimental points can be in accordance with a sum of seven Gaussians as follows:

$$y = \sum_{i=1}^7 K_i \exp \left(-0.5 \cdot \left(\frac{x-x_{ci}}{w_i} \right)^2 \right) \quad (1)$$

Where the x_{ci} 's are ESR frequencies at the peak points and $y = -(P_z - P_0)/P_0$, the K_i values are the enhancements at the peak points, and w_i 's are the standard deviations of the singular Gaussians. For the temperatures 263K, 280K, 296K, and 311K in Table2, all fit parameters are listed. R^2 values, which are the degree of fit between experimental fit function (1) and experimental values, range between 0.950 and 0.990.

Table 2: The experimental points of the GALV/MBFA spectrum can be in accordance with a sum of seven Gaussians shown in (1). For four temperature values, fit parameters are tabulated.

		263 K		280 K		296 K		311 K	
		2008 Data	2021 Data	2008 Data	2021 Data	2008 Data	2021 Data	2008 Data	2021 Data
ESR Frequency at the Peak Point (MHz)	X_{c1}	33.16	33.05	32.99	33.00	32.90	32.86	33.09	33.15
	X_{c2}	36.81	36.72	36.61	36.62	36.63	36.63	36.79	36.77
	X_{c3}	40.18	40.15	40.22	40.22	40.20	40.20	40.20	40.18
	X_{c4}	44.58	44.67	44.69	44.70	44.75	44.78	44.67	44.60
	X_{c5}	49.02	48.91	49.13	49.14	49.02	49.04	49.15	49.15
	X_{c6}	52.51	52.79	52.66	52.66	52.62	52.62	52.57	52.57
	X_{c7}	56.31	57.07	56.38	56.38	56.32	56.32	56.37	56.37
Weight of the individual Gaussian	K₁	6.73	3.71	6.64	3.36	6.47	2.98	5.07	1.79
	K₂	11.20	6.00	10.53	5.32	11.68	4.59	8.01	2.95
	K₃	9.38	4.93	8.79	4.43	8.13	3.67	7.26	3.11
	K₄	5.61	3.04	5.33	2.71	5.21	2.39	4.96	1.91
	K₅	10.50	5.35	10.10	5.07	9.32	4.25	9.17	3.59
	K₆	16.42	8.26	15.15	7.78	14.80	6.72	14.49	5.68
	K₇	11.72	6.02	10.88	5.45	9.93	4.50	9.31	3.64
Standard Deviation of the individual Gaussian (MHz)	w₁	1.45	1.32	1.17	1.17	1.00	0.97	2.30	2.43
	w₂	0.88	0.98	1.04	1.04	1.00	1.08	0.89	0.95
	w₃	1.06	1.02	1.05	1.04	0.94	0.94	1.14	1.08
	w₄	1.87	2.15	1.87	1.87	2.36	2.40	1.72	1.81
	w₅	1.09	0.90	1.19	1.20	1.03	1.01	1.15	1.14
	w₆	0.97	1.45	0.94	0.93	0.96	0.96	0.90	0.91
	w₇	1.48	1.35	1.26	1.28	1.33	1.35	1.39	1.41

2008 Data (Ovalioglu et al., 2010).

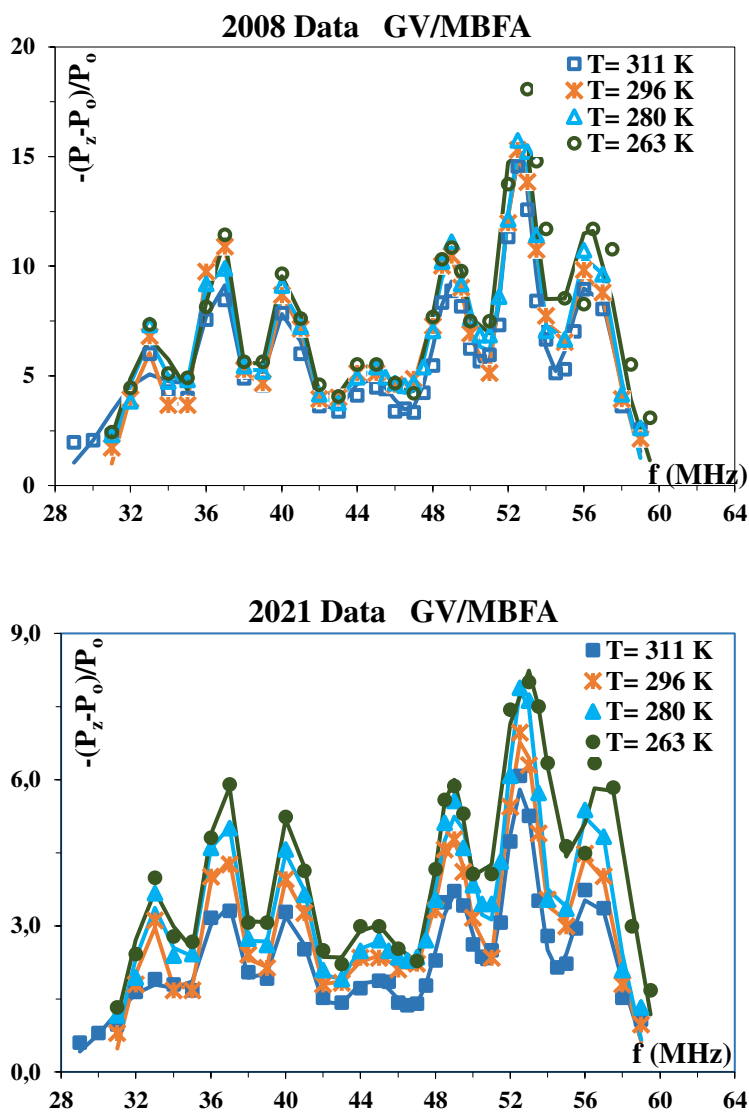


Figure 3: (a) EPR Spectra of the Galvinoxyl /MBFA sample with respect to four temperature values. Experimental data of the year 2008. (b) EPR Spectra of the Galvinoxyl /MBFA sample with respect to four temperature values. Experimental data of 2021.

2.2 DNP parameters

The NMR enhancement factor is figured out as follows (Hausser & Stehlik, 1968; Kramer & Müller-Warmuth, 1964; Enkin et al., 2015)

$$A = -\frac{(P_z - P_0)}{P_0} = \rho \cdot f \cdot s \left| \frac{\gamma_s}{\gamma_I} \right| \quad (2)$$

where P_0 and P_z correspond to the NMR signal amplitudes excluding and including ESR saturation power, γ_s and γ_I correspond to electronic and nuclear gyromagnetic ratios, respectively, Furthermore, $\left| \frac{\gamma_s}{\gamma_I} \right| = 700$ for ^{19}F . In this equation f stands for the leakage factor for the nuclear relaxation, s stands for the saturation factor, and for the full EPR saturation that value equals 1, and finally, ρ stands for the nuclear-electron coupling parameter, that is a measurement unit for the nuclear-electron interaction. All saturation tests mentioned above were saturated at 45.5 MHz.

The saturation tests were conducted with a precision of ± 2 °C for each sample in the liquid phase. For the sample that we have, P_0 has been tested four times at four distinct temperatures, and P_z values have been collected from at least 7 distinct ESR power so as to saturate electronic spin polarization.

The saturation factor is calculated by using the following equation

$$S = \frac{\Pi_0 - \Pi_z}{\Pi_0} \quad (3)$$

In this equation, Π_0 stands for the electronic spin polarization and Π_z is the dynamic polarization in the thermal equilibrium level. For the infinite ESR power, Π_z corresponds to 0 and s corresponds to 1, and in line with Equation (2) enhancement factor, A will get the A_∞ value.

In order to determine the A_∞ value, $A^{-1} = [(P_z - P_0)/P_0]^{-1}$, namely the reciprocal of the enhancement factor, should be attained as a function of ESR power's reciprocal value. This value is proportional to H_{1e}^{-2} or V_{eff}^{-2} . Here, V_{eff} stands for the high-frequency voltage on the ESR coil. Whereas, A^{-1} corresponds to A_{end}^{-1} for the maximum attainable ESR power. In the event that ESR saturation is complete, the ESR power should be infinitive or V_{eff}^{-2} equals zero. For Galvinoxyl/MBFA, the variation of $-(P_z - P_0)/P_0$ with respect to V_{eff}^{-2} based on four distinct temperatures is demonstrated in Figure 4. There, A_∞^{-1} values stand for the points of intersection of the extrapolated best-fit line and $V_{\text{eff}}^{-2} = 0$ line.

For the sample, f , the leakage factor, was defined as 0.90 ± 0.05 for sample by utilizing the information on fluorinated Galvinoxyl solutions in the literature (Müller-Warmuth & Meise-Gresch, 1983; Peksoz, Yalciner, Cimenoglu, 2009). Based on the equation $\left| \frac{\gamma_s}{\gamma_I} \right| = 700$ for ^{19}F corresponds to 700. Considering this, ρ values were extracted from the equation as follows

$$\rho = -\frac{A_\infty}{700 \cdot f} \quad (4)$$

In the low field, extreme narrowing condition ($\omega s \tau_1 \ll 1$) can be met at high-temperature levels.

In this study, the measurement was only performed at 311K maximum temperature level. Here, K can be calculated by using the equation below

$$K = \frac{0.966 - 1.953\rho}{1 + \rho} \quad (5)$$

$A_\infty - 10^3/T$ and $\rho - 10^3/T$ graphics for Galvinoxyl/MBFA are given in Figure 5 and Figure 6 respectively. Our sample was prepared at a concentration of 3 mM. Table 3 provides gauged DNP parameters for the same sample and attained DNP parameters, which were found by utilizing results obtained in 2008. In the equation, respectively, A_∞ stands for the enhancement factor; ρ stands for the nuclear–electron coupling parameter; s stands for the saturation factor, and lastly, K stands for the importance of dependent scalar coupling parameter. In reference to 2008 data, particularly ρ -value at 311K equals 0.142 that is the greatest coupling parameter value for all temperature levels as seen in Table 3. For the temperature levels 311K, 295K, 280K, 263K respectively, we have declining percentages for ρ values of our sample, roughly 9, 10, 8, and 9. This condition indicates that at the end of the thirteen years period solvents move slower. Saturations in tests range from 64.2% to 69.6%. A_∞ values are all negative at all of the signal enhancements, since P_z , the observed dynamic polarization, are inverted, based on P_0 , the pure NMR signal. This also leads to a

differentiation between values of ρ , the nuclear-electron coupling parameter, for various temperature levels.

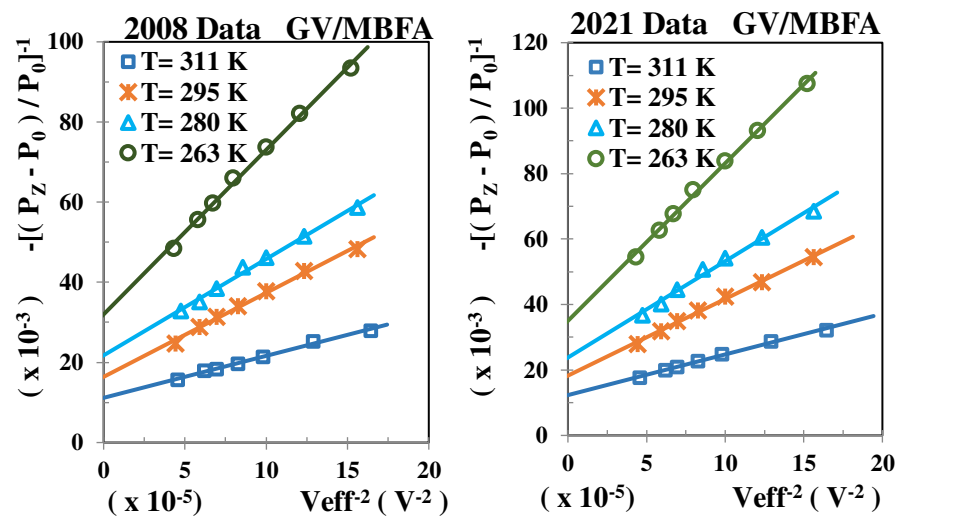


Figure 4: Variation of $\left[\frac{(P_z-P_0)}{P_0}\right]^{-1}$ with respect to V_{eff}^{-2} for asphaltene/meta-difluorobenzene sample based on four distinct temperature levels. Here, A_{∞}^{-1} values stand for the intersection points of the extrapolated best-fit line and the $V_{eff}^{-2} = 0$ line. On the other hand, the R^2 values present the agreement degree between the experimental points and the linear fit function. Above, graph (a) is based on 2008 data, and graph (b) is based on 2021 data.

Table 3: DNP parameters for Galvinoxyl/MBFA suspensions.

c(mM)	T (K)	A_{∞}^*	A_{∞}	ρ^*	ρ	s^*	s	K^*	K
3,0	311	-89,5	-81,2	0,142	0,129	0,712	0,696	0,60	0,63
	295	-61,0	-54,7	0,097	0,087	0,664	0,652	0,71	0,73
	280	-46,0	-42,0	0,073	0,067	0,663	0,646	0,77	0,78
	263	-31,3	-28,6	0,050	0,045	0,659	0,642	0,83	0,84

* 2008 Data (Peksoz et al., 2009)

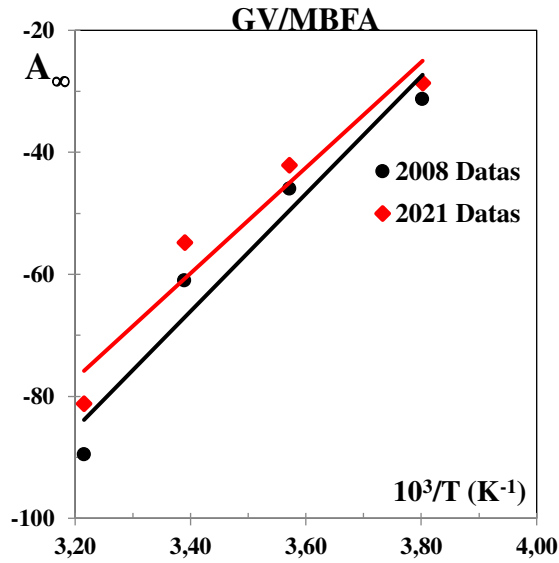


Figure 5: For GV/MBFA, it is seen that the A_∞ values obtained from the experiments performed at distinct temperature levels vary with respect to $10^3/T$.

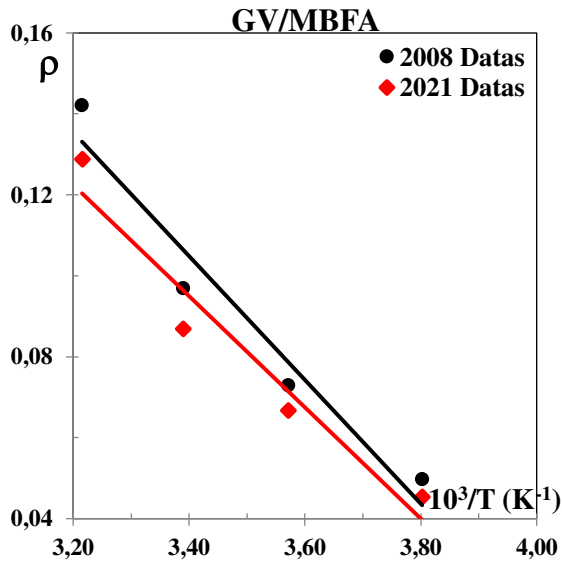


Figure 6: For GV/MBFA, it is seen that the ρ , the nuclear-electron coupling parameter, values obtained from the experiments performed at distinct temperature levels vary with respect to $10^3/T$.

CONCLUSION

DNP experimentations were carried out to investigate suspension of galvinoxyl in MBFA solvent at 1.53 mT. We have observed a single Gaussian which was peaked around 45.5 MHz in the EPR spectra of the galvinoxyl.

The following results can be deduced for the context of the scientific research implemented and discussed in this paper.

First of all, the spectrum was monitored as a single Gaussian generated by the overlap of multiple Lorentzians. The shape of the spectrum conforms with data obtained in 2008. After 13 years of the waiting period for samples forming colloidal suspensions with MBFA solvent galvinoxyl, the ρ -value, the parameter for nuclear electron coupling, was found to be lower. More clearly, the ρ -value, the nuclear-electron coupling parameter, differs between +0.5, which stands for pure dipolar, and -1.0, which stands for pure scalar within the low magnetic fields. Additionally, the ρ values obtained in this analysis are between those limits in question. In this analysis, ρ values are all positive. In fact, this indicates the dipolar section of intermolecular spin-spin interactions is overwhelming. Almost for all temperatures, the K value has risen due to the value of the parameter of dependent scalar coupling. This has a crucial outcome, that is the scalar section of intermolecular spin-spin interactions has risen in samples waited for years, in other words, the dipolar section of the interactions has degraded.

REFERENCES

- Ardenkjaer-Larsen, J. H., Boebinger, G. S., Comment, A., Duckett, S., Edison, A., Engelke, F., Griesinger, C., Griffin, R. G., Hilty, C., Maeda H., Parigi G., Prisner, T., Ravera, E., Bantum, J. V., Vega, S., Webb A., Luchinat C., Schwalbe, H., Frydman, L. (2015). Facing and Overcoming Sensitivity Challenges in Biomolecular NMR Spectroscopy. *Angewandte Chemie International Edition*. 54, 9162–9185.
- Bennati, M., Tkach, I., Türke, M. T. (2011). Dynamic nuclear polarization in liquids. *Electron Paramagnetic Resonance*. 22, 155–182.
- Bennati, M., Orlando, T. (2019). Overhauser DNP in liquids on ^{13}C nuclei. *eMagRes*, 8, 11–18.
- Bantum V. J., Meerten, V., B.; Sharma, M.; Kentgens, A. (2016) Perspectives on DNP-enhanced NMR spectroscopy in solutions. *Journal of Magnetic Resonance*. 264, 59–67.
- Coppinger, G.M. (1957). A stable phenoxyl radical inert to oxygen, *Journal of The American Chemical Society*. 79, (2) 501-502.
- Denysenkov, V. P., Prisner, T. F. (2019). Liquid-state Overhauser DNP at high magnetic fields. *eMagRes*. 8, 41–54.
- Enkin, N., Liu G., Gimenez-Lopez, M. del C., Porfyakis, K., Tkacha, I., Bennati, M. (2015). A high saturation factor in Overhauser DNP with nitroxide derivatives: the role of ^{14}N nuclear spin relaxation *Physical Chemistry Chemical Physics*. 17, 11144
- Franck, J. M.; Pavlova, A.; Scott, J. A.; Han, S. (2013). Quantitative cw Overhauser effect dynamic nuclear polarization for the analysis of local water dynamics. *Progress in Nuclear Magnetic Resonance Spectroscopy*. 74, 33–56.
- Gierke, W., Harrer, W., Kurreck, H., Reusch, J. (1973). *Metallorganische Synthese und EPR-Spektroskopie von Galvinoxyl-Verbindungen*, *Tetrahedron Letters*. 38 3681-3684.

- Gierke, W., Harrer, W., Kurreck, H., Reusch, J. (1976). Über Galvinole und Galvinoxyle, II EPR-HFS- und elektronen-spektroskopische Untersuchung von Galvinoxyl-Mehrspinsystemen, Zeitschrift für Naturforschung B Chemical. Science. 31 965-973.
- Griesinger, C.; Bennati, M.; Vieth, H. M.; Luchinat, C.; Parigi, G.; Hofer, P.; Engelke, F.; Glaser, S. J.; Denysenkov, V.; Prisner, T. F. (2012). Dynamic nuclear polarization at high magnetic fields in liquids. Progress in Nuclear Magnetic Resonance Spectroscopy. 64, 4–28.
- Harrer, W., Kurreck, H., Reusch, J., Gierke, W. (1975). Über Galvinole und Galvinoxyl-MehrspinsystemedI : eine neue metallorganische Synthese von Mono- und Oligo-Galvinolen, Tetrahedron. 31 625-632.
- Hausser, K.; Stehlik, D. (1968). In Advances in Magnetic Resonance; Waugh, J. S., Ed.; Academic Press, Vol. 3, pp 79–139.
- Hausser, K.H., Stehlik, D. (1968). Dynamic Nuclear Polarization in Liquids. Advances in Magnetic and Optical Resonance 3, 79-139.
- Kirimli, H.E., Ovalioglu, H. (2014). ¹⁹F Dynamic Nuclear Polarization and SEM in Suspensions Consisting of Fluorobenzene Derivatives and Asphaltene Extracted from MC-800 Liquid Asphalt Journal of Dispersion Science and Technology. 35, 255-264.
- Kirimli, H.E., Ovalioglu, H., Akay, C. (2017). Intermolecular Effects of Fluorocarbons on MC800 Asphaltene and their Characterization. Acta Physica Polonica A 131 (3) 336-338.
- Kramer, K.D., Müller-Warmuth, W. (1964). Über Zusammenhänge der OvERHAUSER-Kernpolarisation mit der Molekülbewegung, der Frequenz und der Relaxation in Flüssigkeiten. Zeitschrift. Naturforschung. 19a, 375.
- Lampp, L., Azarkh, M., Drescher, M., Imming, P. (2019). Galvinoxyl radicals: Synthesis of new derivatives, determination of low oxygen contents, and stability studies, Tetrahedron. 75 2737-2747.
- Levien, M., Hiller, M., Tkach, I., Bennati, M., Orlando, T. (2020). Nitroxide Derivatives for Dynamic Nuclear Polarization in Liquids: The Role of

- Rotational Diffusion, *The Journal of Physical Chemistry Letters*. 11, 1629–1635.
- Müller-Warmuth, W., Meise-Gresch, K. (1983). Molecular Motions and Interactions as Studied by Dynamic Nuclear Polarization (DNP) in Free Radical Solutions. *Advances in Magnetic and Optical Resonance*. 11, 1-45.
- Ovalioglu, H., Peksoz, A., Kirimli, H.E., Yalciner, A. (2010). Intermolecular Spin-Spin Coupling in Highly Fluorinated Solutions of Galvinoxyl Free Radical. *Zeitschrift. Naturforschung*. 65a, 254-262.
- Overhauser, A. W. (1953). Polarization of nuclei in metals. *Physical Review*. 92, 411–415.
- Peksoz, A., Yalciner, A., Cimenoglu, M.A. (2009). A Low Field Fluorine-Electron Double Resonance Study for GALV and BDPA in Some Aliphatic and Aromatic Solvents. *Zeitschrift. Naturforschung*. 64a, 477-484.
- Potenza, J. (1972). Measurement and applications of dynamic nuclear polarization. *Advances in Molecular Relaxation Processes*. 4, 229-354.
- Prisner, T., Denysenkov, V., Sezer, D. (2016). Liquid state DNP at high magnetic fields: Instrumentation, experimental results and atomistic modelling by molecular dynamics simulations, *Journal of Magnetic Resonance* 264 68–77.
- Yalciner, A. (1978). ESR Hyperfine Structure of α , γ -Bisdiphenylene- β -phenyl allyl via Overhauser Effect in Weak Magnetic Fields. *Communications Faculty of Sciences University of Ankara* 27, 1-20.

CHAPTER 6

**THE EFFECT OF SAMPLE AGE OF META-
DIFLUOROBENZENE IN MC-800 ASPHALTENE
SUSPENSION ON DYNAMIC NUCLEAR POLARIZATION
PARAMETERS**

Assoc. Prof. Dr. Hüseyin OVALIOĞLU¹

¹ Bursa Uludag University, Faculty of Arts and Sciences, Physics Department, Bursa/Turkey. ovali@uludag.edu.tr ORCID NO: 0000-0002-7224-7526

INTRODUCTION

Crude oils are sophisticated liquids that have a wide variety of viscosities, at this point, "heavy oils" are typically considered to have viscosities over 100 mPa·s (Briggs, Fulleylove, Wright, 1988). Conventionally, the components of SARA (saturated, aromatic, resin, and asphalt) are differentiated in these materials by means of a well-defined separation method. Resins and asphaltenes (defined as the n-alkane insoluble, toluene soluble fraction) are accepted to be main reasons for having high viscosity and average molecular weight characteristics for oils. (Gizatullin et al., 2018; Shukla, 2018; Martyanov, Larichev, Morozov, Trukhan, Kazarian, 2017; Yen & Chilingarian, 1994; Yen & Chilingarian, 2000; Chilingarian & Yen, 1978; Evdokimov, 2010; Ilyin & Strelets, 2018; Chen et al., 2014). In addition, crude oils have paramagnetic characteristics (Yen & Chilingarian, 1994; Yen & Chilingarian, 2000; Gutowsky, Roger, Rutledge, Unterberger, 1958; O'Reilly, 1958). Many paramagnetic centers are favorably clustered in asphalts and resins and often occur in the shape of consistent carbonaceous FR (Free Radicals), unpaired electrons dislocated over several aromatic or conjugated chemical bonds.

Asphaltenes, which are a part of petroleum, are considered to be polar species, have greater aromatic complexes, and consist of heteroatoms (e.g. O, S, and N), alkyl chains, and certain metals (Evdokimov, Eliseev, Akhmetov, 2006). Asphaltenes have unpaired

electrons, which are observed in crude petroleum by using the ESR (Electron Spin Resonance) experiments (Gutowsky et al., 1958).

DNP (Dynamic Nuclear Polarization) uses liquid state interactions between nucleus and unpaired electron spins to produce enhanced nuclear polarization after the saturation of ESR radical transitions. The maximum DNP enhancement rate of the NMR signal is calculated by the electron-to-nuclear gyromagnetic ratio, γ_e/γ_n . For proton spin, this ratio is 658.

It becomes apparent that studies of the coupling between I, nuclear spin reservoir, and S, electronic spin reservoir, may put forward insight into the dynamics and structure of these sophisticated materials. However, while the coupling itself can also utilize DNP techniques to increase the NMR signal via spin polarization from S to I. Therefore, sensitivity increases by (Shukla, 2018) or (Martyanov et al., 2017) orders of magnitude (Sapunov et al., 2016). The ODNP (Overhauser Type Mechanism) for the hyperpolarization should be the most efficient, as crude oil is historically treated as a viscous liquid (Pradhan, Ovalles, Moir, 2018). Since the comparatively high mobility of oil molecules, including radicals, requires an appropriate regulation of electron-nuclear interaction, this condition leads to an efficient propagation of polarization between nuclei and electrons in oil. The main aspect of ODNP is that when the microwave pumping frequency is in precisely the same resonance as the EPR transition, namely, $f_{MW} = f_e$, the full effect of electron polarization conversion on the

nuclear system is obtained. In fact, Poindexter (Poindexter, 1958; Poindexter & Torrey, 1963) recorded Overhauser form of DNP in the external magnetic field $B_0 = 18$ G on protons of "light" or "medium" crude oils that have a viscosity of 25-40 mPa·s as early as the 1950s.

The nuclear spins are the proton spins in this sample, which are the ^1H center of the solvent medium, while the electron spins are the free electrons on the asphaltene micelles. Unpaired electrons have been dislocated to the unfilled carbon bonds of asphaltene particles' compact aromatic structure (Griesinger et al., 2012). We revealed a dipolar interaction between the solvent hydrogen atoms and unpaired colloidal asphaltene electrons through the DNP process. In a low magnetic field, electron spin saturation, as well as DNP improvements, were achieved, and also DNP parameters have been determined.

1. MATERIALS AND EQUIPMENT

The spectrometer used in this study is a continuous wave weak field dual resonance NMR spectrometer. Additional material is available in the literature on the DNP principle and implementations for liquid samples (Kirimli & Ovalioglu, 2014; Hausser & Stehlik, 1968; Potenza, 1972; Müller-Warmuth & Meise-Gresch, 1983). DNP experiments were performed at 1.53 mT with 61.2 kHz resonance frequency for the ^1H nuclei and the electrons 42.5 MHz resonance frequency. Asphaltene was taken from MC800 fluid asphalt. This asphalt was obtained from the Turkish Petroleum Refineries

Corporation in Kırıkkale province of Turkey. Three distinct asphalt ratios were taken to prepare the suspensions. The solvent was bought from the US, Aldrich Chemical Co.

The main properties of meta-difluorobenzene in Figure 1 used as a solvent in this study are given in Table 1.

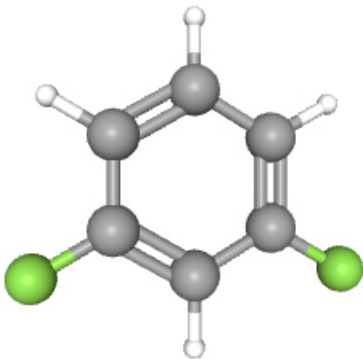


Figure 1: Structure of the meta-difluorobenzene molecule (green color “fluor”; white color “hydrogen” and grey color “carbon”).

Table 1: NMR sensitivity of meta-difluorobenzene and basic constants.

Solvent	Molecular Weight (g mol ⁻¹)	Melting Point (°C)	Boiling Point (°C)	Density (g cm ⁻³)	Viscosity (cP)	Dipole Moment (D)	NMR Sensitivity (x10 ²² spin/cm ³)
meta-difluorobenzene (C ₆ H ₄ F ₂)	114,09	-59	83	1,163	0,603	1,5	1,23

Degasification of the samples was carried out with the Leybold-Heraeus vacuum system and the lowest pressure value seen in our studies was recorded as 1·10⁻⁵ Pa. As seen in Figure 2, the samples were sealed and degassed in Pyrex tubes.



Figure 2: The sample in Pyrex tube was sealed and degassed.

2. RESULTS AND DISCUSSION

2.1. EPR Spectra

To test DNP parameters in the magnetic field, it is important to obtain a free radical EPR spectrum. ESR spectrum should not be affected by the solvents (Yalciner, 1978). Figure 3 displays the EPR distribution for three separate concentrations of the asphaltene/meta difluorobenzene solvent medium. Furthermore, Table 2 demonstrates the Gaussian function parameters of the asphalt/meta-difluorobenzene solvent medium at room temperature in three distinct amounts.

$$y = A \cdot e^{\left[-\frac{1}{2} \frac{(x-x_c)^2}{\sigma^2} \right]} \quad (1)$$

Table 2: Gaussian parameters obtained for the meta-difluorobenzene of MC800 Asphaltene in distinct concentrations. $y=-(P_z-P_0)/P_0$, $x_c=v$ (MHz), x is peak frequency that shows EPR spectrum peak point, σ is the standard deviation, and A is the fit in Eq. 1 parameter shows variance for various experimental data.

concentration	A	A*	x_c	x_c^*	σ	σ^*	R^2	R^2*
1,8 kg m ⁻³	0,44	0,77	42,31	42,34	7,36	7,23	95,31	96,50
3,1 kg m ⁻³	0,40	0,70	42,43	42,29	6,49	6,58	97,29	96,43
6,3 kg m ⁻³	0,35	0,64	42,56	42,50	4,99	5,76	98,07	98,67

*2016 Data (Kirimli et al., 2017).

The spectrum was presented as single Gaussian, created by the overlay of many Lorentzians. Additionally, the measured values of these concentrations are fit with Gaussian functions given by the following equations:

$$-\frac{(P_z-P_0)}{P_0}=0.44\exp\left[-\frac{(v_s-42.31)^2}{108.34}\right] \tag{2a}$$

$$-\frac{(P_z-P_0)}{P_0}=0.40\exp\left[-\frac{(v_s-42.43)^2}{84.24}\right] \tag{2b}$$

$$-\frac{(P_z-P_0)}{P_0}=0.35\exp\left[-\frac{(v_s-42.50)^2}{49.80}\right] \tag{2c}$$

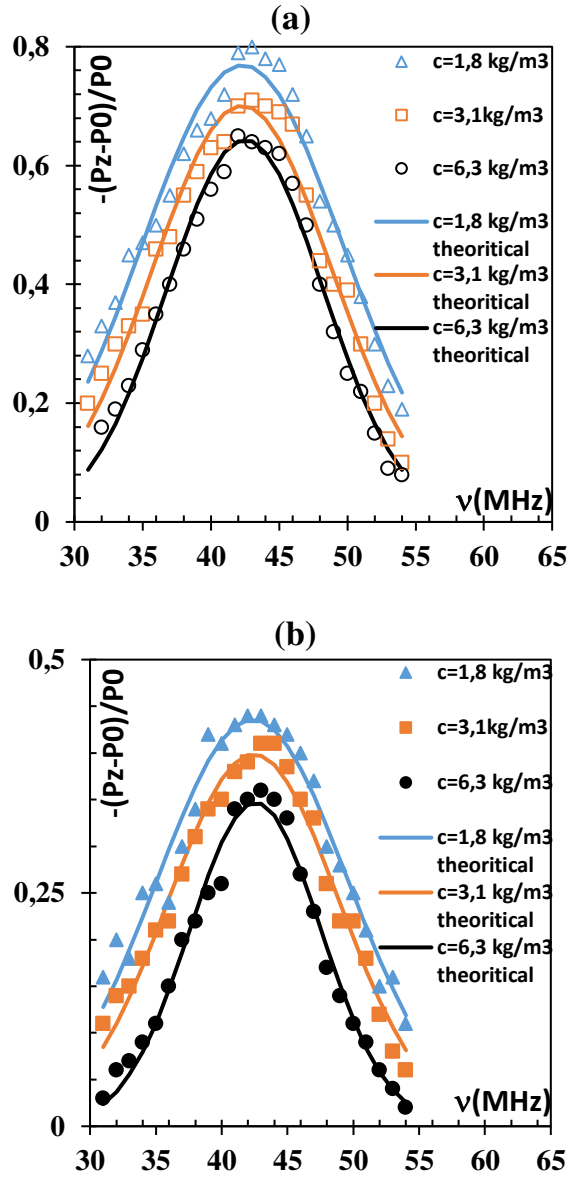


Figure 3: (a) EPR Spectra of the meta-difluorobenzene /MC800 asphaltene sample for three concentrations (Kirimli et al., 2017), (b) EPR Spectra of the meta-difluorobenzene /MC800 asphaltene sample for three concentrations. It is the experimental data of 2021.

2.2. DNP Parameters

The NMR enhancement factor is calculated as follows (Kramer & Müller-Warmuth, 1964)

$$A = -\frac{(P_z - P_0)}{P_0} = \rho \cdot f \cdot s \left| \frac{\gamma_s}{\gamma_I} \right| \quad (3)$$

here P_z and P_0 are the NMR signal amplitudes with and without ESR saturation power. On the other side, γ_s and γ_I symbolize electronic and nuclear gyromagnetic ratios, f is the nuclear relaxation leakage factor, s is the saturation factor equivalent to 1 for the whole EPR saturation, and lastly, ρ is the nuclear-electron coupling parameter, that is a measurement of the nuclear-electron interaction. All of the saturation measurements have been saturated at 42.5 MHz.

The variation of $\left[\frac{(P_z - P_0)}{P_0} \right]^{-1}$ versus V_{eff}^{-2} for asphaltene/meta-difluorobenzene sample is seen at 3 distinct concentrations in Figure 4. For the maximum attainable EPR power, A^{-1} and A_{end}^{-1} are equal. The reciprocal enhancement factor is extrapolated for the infinite ESR power if the saturation condition is met. At complete EPR saturation A_∞ is the enhancement factor and it is calculated as follows

$$A_\infty = -\rho \cdot f \left| \frac{\gamma_s}{\gamma_I} \right| \quad (4)$$

U_∞ , the ultimate enhancement factor, can easily be determined, as A_∞^{-1} values are well proportioned to the reciprocal concentration of the

sample c^{-1} as depicted in Figure 5. Here the ρ values can be calculated after determining U_{∞} .

$$\rho = -\frac{U_{\infty}}{658} \quad (5)$$

In the formula, for each concentration f value was figured by using the A_{∞}/U_{∞} ratio and the s value was computed by using the A_{end} to A_{∞} ratio. A_{∞} , U_{∞} , f , and s parameters which are parameters of the dynamic nuclear polarization are provided in Table 3. Experimental saturations range from 78% to 84%. The value of A_{∞} varies between -8.2 and -10.6. For all samples, it shows an increase with the rise in the concentration of the sample. All A_{∞} and U_{∞} parameters have negative values since P_z and P_0 NMR signals are opposite to each other. This condition also leads ρ , nuclear coupling parameter, to have a positive value for solvent medium. ρ value of asphaltene/meta-difluorobenzene is 0.015.

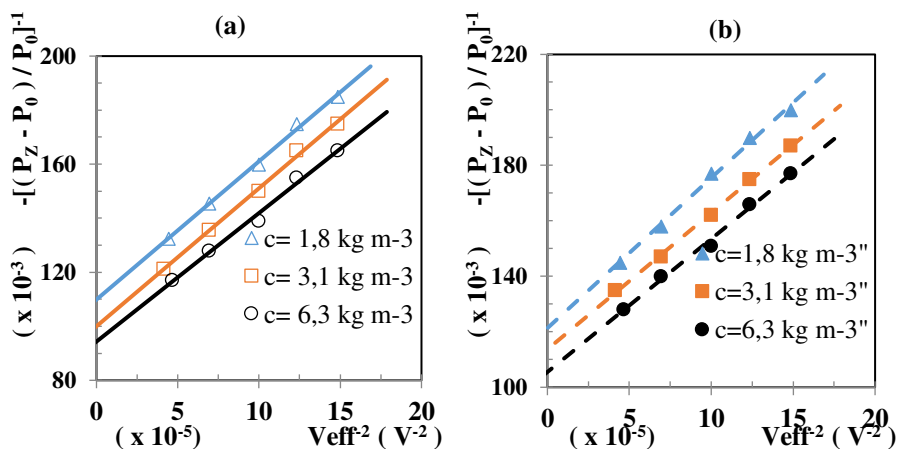


Figure 4: Variation of $\left[\frac{(P_Z - P_0)}{P_0}\right]^{-1}$ versus V_{eff}^{-2} for asphaltene/meta-difluorobenzene sample at 3 distinct concentrations. Here, A_{∞}^{-1} values equivalent to the intersection points of the extrapolated best-fit and the $V_{eff}^{-2} = 0$ lines. The R^2 values indicate how well the linear fit function is consistent with the experimental points. (a) (Kırımli et al., 2017) and (b) 2021 data.

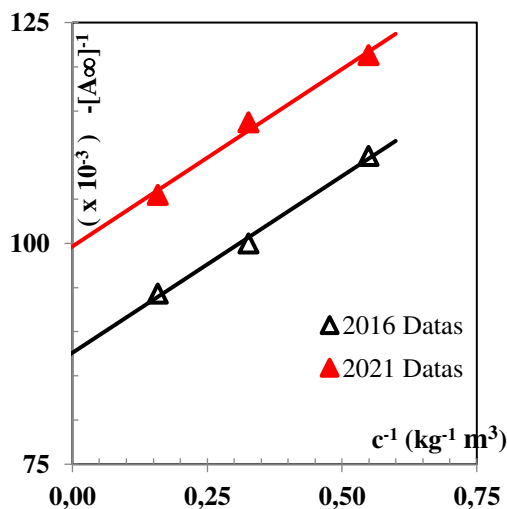


Figure 5: Examples of ultimate enhancement factor evaluations measured at room temperature. Here, the U_{∞}^{-1} values are equivalent to the intersection points of extrapolated best-fit lines and the $c^{-1} = 0$ line (2016 & 2021 data).

Table 3: DNP parameter values for the suspensions of meta-difluorobenzene with asphaltene.

Solvent Medium	C (kg m ⁻³)	A _∞	A _∞ [*]	U _∞	U _∞ [*]	ρ	ρ [*]	f	f [*]	s	s [*]
Asphaltene/meta-difluorobenzene	1,8	-8,2	-9,1					0,821	0,796	0,809	0,779
	3,1	-8,8	-10,0	-10,0	-11,4	0,015	0,017	0,877	0,872	0,801	0,843
	6,3	-9,5	-10,6					0,944	0,931	0,782	0,806

* 2016 Data (Kirimli et al., 2017).

CONCLUSION

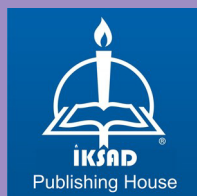
DNP experimentations were conducted to analyze meta difluorobenzene solvents asphaltene suspensions at 1.53 mT. We have observed a single Gaussian which was peaked around 42.5 MHz in the EPR spectra of the asphaltenes. It ranges from +0.5, which means pure dipolar to -1.0 which means pure scalar in low magnetic fields. In our study, had varied between 0.015 and 0.017. Even the new attained ρ values range between the limits mentioned above. Following the five-year retention of samples that formed colloidal suspensions of meta-difluorobenzenic asphaltene solvent medium obtained from liquid asphalt, the nuclear-electron coupling parameter, ρ, was found to be reduced. The decrease in ρ-value is almost %13. Interactions between the solvent molecular hydrogen nuclei and unpaired electrons belonging to the asphaltene micelles are distinguished by dipolarity. Ultimately in this analysis, all ρ values are positive, indicating the superiority of the dipolar component in intermolecular spin-spin interactions. The obtained DNP parameters demonstrate that asphaltene particles have aggregated under the effect of solvent.

REFERENCES

- Briggs, P. J., Baron, P. R., Fulleylove, R. J., Wright, M. S. (1988). Development of Heavy-Oil Reservoirs. *Journal of Petroleum Technology*, 40, 206–214.
- Chen, J. J., Hürlimann, M., Paulsen, J., Freed, D., Mandal, S., Song, Y. Q. (2014). Dispersion of T_1 and T_2 Nuclear Magnetic Resonance Relaxation in Crude Oils *ChemPhysChem*, 15, 2676–2681.
- Chilingarian, G. V., Yen, T. F., (1978). Eds. *Bitumens, Asphalts and Tar Sands*. New York: Elsevier
- Evdokimov, I.N., Eliseev, N.Y., Akhmetov, B.R. (2006). Asphaltene dispersions in dilute oil solutions. *Fuel* 85, (10-11), 1465-1472.
- Evdokimov, I. N. (2010). The Importance of Asphaltene Content in Petroleum—The Revision of Some Persistent Stereotypes. *Petroleum Science and Technology*, 28, 756–763.
- Gizatullin, B., Gafurov, M., Rodionov, A., Mamin, G., Mattea, C., Stapf, S., Orlinskii, S. (2018). Proton–Radical Interaction in Crude Oil-A Combined NMR and EPR Study. *Energy & Fuels*. 32 11261-11268.
- Griesinger, C., Bennati, M., Vieth, H.M., Luchinat, C., Parigi, G., Hofer, P., Engelke, F., Glaser, S.J., Denysenkov, V., Prisner, T.F. (2012). Dynamic Nuclear Polarization at High Magnetic Fields in Liquids *Progress in Nuclear Magnetic Resonance Spectroscopy*. 64, 4 (2012).
- Gutowsky, H. S., Roger Ray, B., Rutledge, R. L., Unterberger, R. R. (1958). Carbonaceous Free Radicals in Crude Petroleum. *The Journal of Chemical Physics*. 28, 744–745.
- Hausser, K.H., Stehlik, D. (1968). Dynamic Nuclear Polarization in Liquids. *Advances in Magnetic and Optical Resonance* 3, 79-139
- Ilyin, S. O., Strelets, L. A. (2018). Basic fundamentals of petroleum rheology and their application for the investigation of crude oils of different natures. *Energy Fuels*, 32, 268–278.
- Kirimli, H.E., Ovalioglu, H. (2014). ^{19}F Dynamic Nuclear Polarization and SEM in Suspensions Consisting of Fluorobenzene Derivatives and Asphaltene

- Extracted from MC-800 Liquid Asphalt Journal of Dispersion Science and Technology. 35, 255-264
- Kirimli, H.E., Ovalioglu, H., Akay, C. (2017). Intermolecular Effects of Fluorocarbons on MC800 Asphaltene and their Characterization. *Acta Physica Polonica A* 131 (3) 336-338.
- Kramer, K.D., Müller-Warmuth, W. (1964). Über Zusammenhänge der OverHAUSER-Kernpolarisation mit der Molekülbewegung, der Frequenz und der Relaxation in Flüssigkeiten. *Zeitschrift. Naturforschung.* 19a, 375.
- Martyanov, O. N., Larichev, Y. V., Morozov, E. V., Trukhan, S.N., Kazarian, S. G. (2017). The stability and evolution of oil systems studied via advanced methods in situ. *Russian Chemical. Reviews*, 86, 999–1023.
- Müller-Warmuth, W., Meise-Gresch, K. (1983). Molecular Motions and Interactions as Studied by Dynamic Nuclear Polarization (DNP) in Free Radical Solutions. *Advances in Magnetic and Optical Resonance.* 11, 1-45.
- O'Reilly, D. E. (1958). Paramagnetic Resonance of Vanadyl Etioporphyrin I. *The Journal of Chemical Physics.* 29, 1188–1189.
- Poindexter, E. (1958). An Overhauser Effect in Natural Crude Oil. *Nature* 1958, 182, 1087.
- Poindexter, E. H., Torrey, H. C. (1963). Overhauser effect well logging. U.S. Patent, US 3096476A
- Potenza, J. (1972). Measurement and applications of dynamic nuclear polarization. *Advances in Molecular Relaxation Processes.* 4, 229-354.
- Pradhan, A., Ovalles, C., Moir, M. (2018). Characterization of Heavy Petroleum Fractions by NMR Techniques. In *The Boduszynski Continuum: Contributions to the Understanding of the Molecular Composition of Petroleum.* Ovalles, C., Moir, M., Eds. ACS Symposium Series; OUP: Washington, DC. pp 73–86.
- Sapunov, V., Denisov, A., Saveliev, D., Soloviev, A., Khomutov, S., Borodin, P., Narkhov, E., Sergeev, A., Shirokov, A. (2016). New vector/scalar Overhauser DNP magnetometers POS-4 for magnetic observatories and

- directional oil drilling support. *Magnetic Resonance in Solids*. 18 (2) 16209.
- Shukla, A. K., (2018). *Analytical Characterization Methods for Crude Oil and Related Products*. JohnWiley & Sons Ltd: Hoboken, NJ.
- Yalciner, A. (1978). ESR Hyperfine Structure of α , γ -Bisdiphenylene- β -phenyl allyl via Overhauser Effect in Weak Magnetic Fields. *Communications Faculty of Sciences University of Ankara* 27, 1-20.
- Yen, T., Chilingarian, G., (1994). *Asphaltenes and asphalts 1*. New York: Elsevier.
- Yen, T., Chilingarian, G., (2000). *Eds. Asphaltenes and asphalts 2*. New York: Elsevier.



ISBN: 978-605-74646-1-3